NASA Technical Memorandum 2003–206892, Volume 22

SeaWiFS Postlaunch Technical Report Series

Stanford B. Hooker, Editor
NASA Goddard Space Flight Center, Greenbelt, Maryland

Elaine R. Firestone, Senior Scientific Technical Editor
Science Applications International Corporation, Beltsville, Maryland

Volume 22, Algorithm Updates for the Fourth SeaWiFS Data Reprocessing

Frederick S. Patt, Robert A. Barnes, Robert E. Eplee, Jr., Bryan A. Franz, and Wayne D. Robinson
Science Applications International Corporation, Beltsville, Maryland

Gene Carl Feldman
NASA/Goddard Space Flight Center, Greenbelt, Maryland

Sean W. Bailey and Joel Gales
Futuretech Corporation, Greenbelt, Maryland

P. Jeremy Werdell
Science Systems and Applications, Incorporated, Lanham, Maryland

Menghua Wang
University of Maryland, Baltimore County, Baltimore, Maryland

Robert Frouin
Scripps Institution of Oceanography, La Jolla, California

Richard P. Stumpf
NOAA Center for Coastal Monitoring and Assessment, Silver Spring, Maryland

Robert A. Arnone, Richard W. Gould, Jr., and Paul M. Martinolich
Naval Research Lab, Stennis, Mississippi

Varis Ransibrahmanakul
SPS Technologies, Silver Spring, Maryland

John E. O'Reilly
NOAA National Marine Fisheries Service, Narragansett, Rhode Island

James A. Yoder
University of Rhode Island, Narragansett, Rhode Island

Preface

The SeaWiFS Project continually strives to improve the quality of the SeaWiFS data products and to expand the product suite. This effort requires the SeaWiFS staff to be knowledgeable of recent developments in marine optics, atmospheric correction approaches, and vicarious calibration techniques. This capability is largely maintained through communication with the user community, particularly the SIMBIOS Project staff and science team which provides most of the *in situ* bio-optical and atmospheric validation data. As a result, a number of significant improvements in the sensor calibration, the atmospheric correction scheme, and certain masks and flags have been developed since the third reprocessing in mid-2000.

One particularly important improvement in data quality resulted from the recalibration of the Marine Optical Buoy (MOBY) to account for spectrometer stray light. MOBY data is used for the vicarious calibration of SeaWiFS. The recalibration required development of a portable version of the National Institute of Standards and Technology (NIST) Spectral Irradiance and Radiance Responsivity Calibrations using Uniform Sources (SIRCUS) which was deployed to the MOBY facility in Honolulu, Hawaii by NIST staff (Carol Johnson and Steve Brown). The cost of the portable system was shared by the SeaWiFS Project, the SIMBIOS Project, and the MODIS science team. The recalibration significantly increased the total radiances in bands 1 and 2, thereby increasing the retrieved water-leaving radiances and decreasing the frequency of negative water-leaving radiances in coastal regions. Another significant improvement is the implementation of a revised near-infrared reflectance model in the atmospheric correction scheme. The improved algorithm is designed to work in turbid Case-2 water with no impact on corrections in clear waters.

The research community has always stated a requirement for daily mean PAR, which is needed for computing primary production and the surface heat budget. With this reprocessing, daily mean PAR is now included in the archive product suite. This PAR product was under development and was tested in collaboration with members of the SIMBIOS science team (Robert Frouin and Menghua Wang) for over two years and the algorithm is described in Chapt. 8.

The overall improvements in the derived products, especially in coastal waters is impressive. I would like to congratulate the SeaWiFS Calibration and Validation Team and others who have helped realize these improvements and who have provided validation data. These collaborations underscore the fact that the SeaWiFS Project and the science community are partners in the overall SeaWiFS program and the Project looks forward to future cooperation.

Greenbelt, Maryland
November 2002

— C. R. McClain

Table of Contents

Table of Contents (*cont.*)

Abstract

The efforts to improve the data quality for the Sea-viewing Wide Field-of-view Sensor (SeaWiFS) data products have continued, following the third reprocessing of the global data set in May 2000. Analyses have been ongoing to address all aspects of the processing algorithms, particularly the calibration methodologies, atmospheric correction, and data flagging and masking. All proposed changes were subjected to rigorous testing, evaluation and validation. The results of these activities culminated in the fourth reprocessing, which was completed in July 2002. The algorithm changes, which were implemented for this reprocessing, are described in the chapters of this volume. Chapter 1 presents an overview of the activities leading up to the fourth reprocessing, and summarizes the effects of the changes. Chapter 2 describes the modifications to the on-orbit calibration, specifically the focal plane temperature correction and the temporal dependence. Chapter 3 describes the changes to the vicarious calibration, including the stray light correction to the Marine Optical Buoy (MOBY) data and improved data screening procedures. Chapter 4 describes improvements to the near-infrared (NIR) band correction algorithm. Chapter 5 describes changes to the atmospheric correction and the oceanic property retrieval algorithms, including out-of-band corrections, NIR noise reduction, and handling of unusual conditions. Chapter 6 describes various changes to the flags and masks, to increase the number of valid retrievals, improve the detection of the flag conditions, and add new flags. Chapter 7 describes modifications to the level-1a and level-3 algorithms, to improve the navigation accuracy, correct certain types of spacecraft time anomalies, and correct a binning logic error. Chapter 8 describes the algorithm used to generate the SeaWiFS photosynthetically available radiation (PAR) product. Chapter 9 describes a coupled ocean–atmosphere model, which is used in one of the changes described in Chapter 4. Finally, Chapter 10 describes a comparison of results from the third and fourth reprocessings along the U.S. Northeast coast.

Prologue

The Sea-viewing Wide Field-of-view Sensor (SeaWiFS) Project has continued efforts to improve the overall quality and accuracy of the SeaWiFS data products. The algorithm improvements used through the third reprocessing (May 2000) were described in Volumes 9, 10, and 11 of the *SeaWiFS Postlaunch Technical Report Series*, (McClain et al. 2000a, 2000b, and O'Reilly et al. 2000, respectively). Since that time, work has been ongoing to identify further improvements and resolve issues with the data products. Specific objectives of the improvements included: reducing the number of pixels with negative water-leaving radiance (L_{WN}) values, particularly in bands 1 and 2; increasing the number of valid retrievals and the geographic coverage, by identifying overly restrictive mask conditions or logic errors which exclude otherwise valid data; and improving the consistency of the atmospheric correction. Numerous other improvements or corrections were identified, for example, to the calibration procedures, bio-optical models, and navigation processing. In addition, an entirely new product—photosynthetically available radiation (PAR)—was added to the product line.

These efforts culminated in the fourth global data reprocessing, which was completed in July 2002. Major improvements in the products resulting from the algorithm changes are as follows: the fraction of band 1 retrievals with negative L_{WN} values was reduced by half; the total number of valid data points was increased by 25%, as was the daily geographic coverage; and the monthly geographic coverage was increased by 6%. In addition, the agreement between the satellite and *in situ* data was significantly improved, particularly in the band 1 and 2 matchups and the chlorophyll matchups, and the long term consistency of the products was also improved.

A short synopsis of each chapter in this volume is given below.

1. Introduction to the Fourth SeaWiFS Reprocessing

The fourth reprocessing of the SeaWiFS global data set in July 2002 was preceded by over two years of data analysis, algorithm development, testing, and evaluation by the SeaWiFS Project. Numerous issues that were known at the time of the third reprocessing were addressed, and solutions were developed. Additional algorithm refinements were proposed during this time. A number of proposed changes were deferred, because they either did not show a clear improvement in data quality, or were not sufficiently well developed to be accepted for operational use. All of the accepted changes were subjected to a rigorous, step-by-step evaluation, and detailed results were made available for review and comment by the scientific community, well in advance of the actual reprocessing. This chapter describes the activities that culminated in the fourth SeaWiFS data reprocessing.

2. Changes to the On-Orbit Calibration of SeaWiFS

Monthly lunar calibrations and daily solar calibrations are used to track the on-orbit stability of the radiometric

calibration of the SeaWiFS instrument. Analyses of these data by the SeaWiFS Calibration and Validation Team (CVT) since the third reprocessing showed residual errors in the detector temperature corrections, the lunar calibration time corrections, and the mirror side reflectance corrections. These analyses, and the resulting changes to the on-orbit calibration methodologies, are presented in this chapter. Revised detector temperature corrections allowed the lunar calibration time series to be characterized by a single, time-dependent exponential function. A time correction was applied to the normalization of the lunar calibration time series; time-dependent mirror side reflectance corrections were also implemented. These changes to the calibration methodologies enabled the production of a more robust on-orbit calibration of SeaWiFS for the fourth reprocessing of the SeaWiFS mission data set.

3. Changes to the Vicarious Calibration of SeaWiFS

The SeaWiFS Project vicariously calibrates the visible bands of the instrument against in-water measurements from the Marine Optical Buoy (MOBY) in order to achieve the necessary calibration accuracy for the SeaWiFS retrievals of water-leaving radiances. The SeaWiFS CVT implemented several changes in the vicarious calibration procedure for the fourth reprocessing of the SeaWiFS mission data set. The most significant change is the use of stray light corrected MOBY data in the vicarious calibration. More stringent data quality screening criteria were also implemented for both MOBY and SeaWiFS data to determine the vicarious calibration matchups. Finally, an inverse vicarious calibration procedure was implemented in which the vicarious gains are computed at the top of the atmosphere. The SeaWiFS top-of-the-atmosphere (TOA) radiances are compared with MOBY water-leaving radiances that have been propagated to the top of the atmosphere using the SeaWiFS-retrieved atmospheric correction parameters. These changes to the vicarious calibration procedure enabled the production of a more robust set of vicarious gains for the fourth reprocessing of the SeaWiFS mission data set.

4. Modifications to the SeaWiFS NIR Correction

This chapter describes several changes made to the near-infrared (NIR) correction implemented during the fourth reprocessing of SeaWiFS data. The changes made were both to correct flaws in the actual implementation of the NIR correction and to improve the estimation of NIR reflectance. The changes include revised water absorption coefficients, the addition of a scaling factor to allow for the gradual introduction of the NIR correction as the derived chlorophyll concentration increases, improvements to the iteration control, and an alternative model for the backscatter estimate. The revised NIR correction reduces discontinuities in the aerosol model selection at the boundaries where the correction is introduced. It also reduces the attenuation effect that the original correction had on high chlorophyll concentrations.

5. Changes to the Atmospheric Correction Algorithm and Retrieval of Oceanic Optical Properties

In preparation for the fourth SeaWiFS reprocessing, a series of algorithm changes were implemented to enhance the performance of the atmospheric correction process and to improve the quality and consistency of oceanic optical property retrievals. Included in these changes was the introduction of a filtering process to reduce the relative noise between the two NIR channels. In addition, several modifications were made to improve the handling of the SeaWiFS out-of-band response, and the normalization of water-leaving radiances was extended to account for Fresnel transmittance effects through the air–sea interface. These and other algorithm updates are described within this chapter.

6. Masks and Flags Updates

The flags and masks used for the SeaWiFS level-2 and level-3 processing were updated for the recent fourth reprocessing. This chapter discusses the changes and why they were made. In many cases, underlying algorithms were changed. Some flags changed their states to either flagging (noting a condition), or masking (denoting data excluded from the product) to allow more data to be kept or to improve its quality. New flags were introduced either as a part of new algorithms or to denote the status of the data more clearly. The flag and mask changes significantly contributed to the improvement in the data quality and increased the amount of data retrieved.

7. Level-1a and Level-3 Processing Changes

Improvements were made in the level-1a and level-3 data processing for the fourth reprocessing. Two of these—handling of the spacecraft time tag anomalies, and modification of the level-3 space binning program—address specific problems in the data and processing logic, which excluded otherwise valid data from processing. The third improvement, an update to the navigation algorithms, improves the overall data quality by reducing the maximum navigation errors. The net effect of these changes is an increase both in coverage and quality of the SeaWiFS data products.

8. The SeaWiFS PAR Product

A new SeaWiFS derived product was developed which provides an estimate for the amount of PAR reaching the ocean surface over a 24 hr period. A description of the algorithm is provided in this chapter, followed by comparisons with *in situ* observations. The *in situ* observations include several years of data covering a wide range of solar illumination conditions. The results indicate good algorithm performance, with root mean squared (RMS) differences between satellite-retrieved and observed daily average PAR within a few einsteins per square meters per day.

9. A Partially Coupled Ocean–Atmosphere Model for Retrieval of Water-Leaving Radiance from SeaWiFS in Coastal Waters

The global atmospheric correction algorithm for SeaWiFS tends to over correct for the atmosphere in coastal waters because of water-leaving radiance (L_W) in the NIR part of the spectrum, λ_r. This $L_W(\lambda_r)$ phenomenon occurs particularly in water with high inorganic particulate levels. An iterative solution is used to solve this problem. A bio-optical model is used to determine the NIR backscatter from the backscatter at 670 nm, and specifically addresses inorganic particulates. This solution requires compensation for absorption by chlorophyll, detrital pigments, and gelbstoff (colored dissolved organic matter). The $L_W(\lambda_r)$ is found and removed from the total radiance so that the standard atmospheric models can be applied. Chlorophyll *a* concentrations, C_a, in coastal and Case-2 waters are reduced to appropriate levels. The algorithm cannot yet correct areas where negative L_W occurs at 670 nm.

10. A Comparison of SeaWiFS LAC Products from the Third and Fourth Reprocessing: Northeast US Ecosystem

A comprehensive set of 2,524 local area coverage (LAC) scenes of the northeast US continental shelf and adjacent waters scanned by SeaWiFS from 4 September 1997 to 11 November 2002 was processed using NASA standard algorithms and methods employed in the fourth reprocessing. Estimates of chlorophyll *a* concentration (C_a) and normalized water-leaving radiance (L_{WN}) from the fourth reprocessing are statistically compared with results obtained previously from the third reprocessing. Chlorophyll *a* concentration from the fourth reprocessing is lower than those from the third reprocessing in Gulf Stream and Sargasso Sea waters, along the outer continental shelf and slope water, and over the deep basins in the Gulf of Maine. In nearshore shelf waters approximately less than 50 m, C_a from the third and fourth reprocessings are comparable, except over the shoal water on Georges Bank, Nantucket Shoals, and the northern nearshore Gulf of Maine, where C_a from the fourth reprocessing is approximately 1.1–1.2 times greater than C_a from the third reprocessing. The median $L_{WN}(412)$ and median $L_{WN}(443)$ values from the fourth reprocessing are substantially greater than values from the third reprocessing, and the frequency of negative water-leaving radiances for the 412 nm and 443 nm bands is significantly lower with the fourth reprocessing. Statistical match-up comparisons between SeaWiFS C_a and *in situ* C_a indicate that the fourth reprocessing improved the accuracy of C_a estimates for this region.

Chapter 1

Introduction to the Fourth SeaWiFS Reprocessing

Gene C. Feldman
NASA/Goddard Space Flight Center
Greenbelt, Maryland

Frederick S. Patt
Science Applications International Corporation
Beltsville, Maryland

Abstract

The fourth reprocessing of the SeaWiFS global data set in July 2002 was preceded by over two years of data analysis, algorithm development, testing, and evaluation by the SeaWiFS Project. Numerous issues that were known at the time of the third reprocessing were addressed, and solutions were developed. Additional algorithm refinements were proposed during this time. A number of proposed changes were deferred, because they either did not show a clear improvement in data quality, or were not sufficiently well developed to be accepted for operational use. All of the accepted changes were subjected to a rigorous, step-by-step evaluation, and detailed results were made available for review and comment by the scientific community, well in advance of the actual reprocessing. This chapter describes the activities that culminated in the fourth SeaWiFS data reprocessing.

1.1 INTRODUCTION

Throughout the life of the SeaWiFS mission, the NASA SeaWiFS Project, working in close collaboration with members of the ocean color research community, has conducted continual evaluations of the calibration, algorithms, and operational procedures used to process SeaWiFS data. Significant progress has been made in a large number of areas which have not only continuously improved the scientific quality of the SeaWiFS data products since launch, but have also expanded the product suite to include a number of valuable additional products. Some of these products are the Normalized Difference Vegetation Index (NDVI), PAR, and Land Surface Reflectance. Before implementing any changes, however, to the operational products that are archived and distributed by the Goddard Space Flight Center (GSFC) Distributed Active Archive Center (DAAC), the SeaWiFS Project conducts a very comprehensive set of evaluations for each of the proposed changes, and solicits feedback from the scientific community on the validity of the changes and their effects on the derived products.

In July 2002, the SeaWiFS Project completed the most recent round of evaluations and concluded that the improvements justified another reprocessing. To facilitate the exchange of information with as broad a representation of the international ocean color community as possible, a comprehensive Web site was developed that contained all the details of the analyses performed, complete statistical analyses of the results, and a change-by-change accounting for the resulting differences in the derived products. The Web site† contained a summary of the results for each of the detailed incremental tests that were run to assess the effect of each change proposed for the fourth reprocessing of the SeaWiFS global data. These tests were all run for the month of May 1999. The summary for each test included a statement of the changes added for that test, and a brief discussion of the changes in the products that resulted from the test. The discussions included links to text, images, and plots on the Web site which described the changes in detail and illustrated the results. In addition to these detailed tests, additional analyses were performed on the complete SeaWiFS mission period; these results are presented on the Web site as well.

While science is a continuous process, and there will always be additional improvements that can be made as understanding improves, the SeaWiFS Project believes that the results of the most recent evaluations clearly demonstrate that better products are produced today than during the third SeaWiFS reprocessing. This belief was strongly supported by the feedback from the ocean color scientists, who reviewed the posted analyses and performed additional evaluations of their own.

† `http://seawifs.gsfc.nasa.gov/SEAWIFS/RECAL/Repro4`

In parallel with the changes to the processing algorithms, substantial advances were made in the computational capabilities, including both the system hardware and the data processing system software. As a result, the SeaWiFS Project was able to reprocess all of the standard archive products for the entire mission in less than one week—achieving a reprocessing rate of approximately 400:1 throughput capacity. This made possible multiple, full mission tests well in advance of the final reprocessing and delivery of the archive products to the DAAC, and provided both the Project and the scientific community with unprecedented knowledge of the full effects of the algorithm changes.

1.2 REPROCESSING MOTIVATION

At the time of the third reprocessing (May 2000), a number of issues remained to be resolved with the SeaWiFS products and algorithms. The issues spanned nearly all aspects of the level-2 algorithms, including the sensor calibration, atmospheric correction, in-water retrievals, and the flags and masks. In addition, improvements were being developed in areas such as navigation, level-3 binning, and new products, which could be applied to the mission data set only through reprocessing. This section summarizes the issues that led to the fourth SeaWiFS reprocessing.

1.2.1 Calibration

The problem of low and negative water-leaving radiances (L_{WN}) in SeaWiFS bands 1 and 2 (412 and 443 nm, respectively) received a great deal of attention during the preparation for the third reprocessing. Indeed, every level-2 algorithm change was evaluated with regard to its effect on the number of pixels with negative L_{WN} values. Nonetheless, this problem remained largely unresolved, particularly in coastal areas. In addition, the match-up comparisons consistently showed that SeaWiFS band 1 radiances were low relative to the *in situ* data, by about 15% on average (Bailey 2000).

The calibration temporal corrections for bands 7 and 8 were represented as a series of quadratic and linear segments, to accommodate periodic fluctuations in the radiometric response. These provided a reasonable representation of the instrument response, but required periodic updating and did not extrapolate well for future processing. In addition, the temporal response for all of the bands, determined from the lunar calibration data, was based on an assumption that bands 3 and 4 had no significant temporal change.

The radiometric correction to account for the differences of the two sides of the half-angle mirror is referred to as the *mirror side correction*. These corrections also showed changes over time, which at that time were corrected in stepwise fashion, by adjusting the correction constants for each calibration time segment. This had the disadvantage of introducing discontinuities into the mirror side corrections.

The vicarious calibration of the visible bands using the MOBY data was performed at the surface, by comparing MOBY and SeaWiFS radiances. This required an iterative approach, because there was no direct conversion of surface radiance differences to TOA calibration corrections. In addition, the data selection criteria and processing methods were developed independently for the vicarious calibration and validation activities, and were not consistent.

1.2.2 Atmospheric Correction

The third reprocessing included an iterative method of correcting the NIR bands for surface radiance prior to their use in atmospheric correction (Siegel et al. 2000). Although this approach was selected from several candidates as providing the best overall results at that time, it suffered from several disadvantages:

a) Small, but measurable effects at very low chlorophyll values, which theoretically should have had no effect on these bands;

b) Underestimation of high chlorophyll values;

c) Inapplicability to Case-2 waters;

d) Incorrect absorption coefficients for the SeaWiFS bands passes; and

e) Occasional convergence problems.

Very clear atmospheric conditions, which resulted in low or negative band 8 aerosol reflectance, caused large uncertainties in the aerosol model selection or outright failure of the atmospheric correction. This frequently resulted in chlorophyll retrieval failures under what, in fact, were nearly ideal viewing conditions.

The radiometric resolution of bands 7 and 8 also contributed to model selection uncertainty (Hu et al. 2000a). At low aerosol reflectance levels, one-bit changes in the band 7 or 8 signal resulted in significant changes in single-scattering aerosol reflectance ratio, ϵ values, which sometimes resulted in excessive model switching.

1.2.3 In-Water Retrievals

The effects of out-of-band contributions to the SeaWiFS radiances were already handled in the third reprocessing by applying a correction to the band-averaged normalized water-leaving radiances (L_{WN}). There were two remaining issues:

1. The solar irradiance used for the computation of remote sensing reflectance from the corrected L_{WN} values was still band averaged.
2. The corrections were determined from a chlorophyll-based water-leaving radiance model (Gordon et al. 1988) and used a log-linear interpolation of 13 discrete wavelengths to the SeaWiFS band passes.

1.2.4 Flags and Masks

Most of the flag algorithms used for SeaWiFS level-2 processing were developed prior to the SeaWiFS launch; a number had not been reviewed since, or had been superficially modified (i.e., refinement of thresholds). The results of flagging and masking, specifically the number of pixels and bins that were affected, were not well understood.

1.2.5 Anomalous Chlorophyll

A small, but significant, number of pixels produced anomalous high chlorophyll values in areas of moderate or low chlorophyll. These values were averaged into the level-3 time binned data products, and continued to be visible as *speckles*, i.e., isolated high values, in the products even over long compositing periods.

1.2.6 Other Processing Levels

The navigation processing performed during level-1a conversion has undergone continual evaluation and periodic improvement. These changes are normally incorporated into operational processing when they are accepted, but can only be applied to the mission data set through reprocessing. In addition, the detection and handling of time anomalies in the SeaWiFS data stream was entirely a manual process, and a problem in the first level-3 binning step caused otherwise valid level-2 scenes to not be binned.

1.2.7 New Products

An ongoing effort has been to identify additional geophysical parameters that could be produced from SeaWiFS data and eventually delivered as archive products. Numerous candidate products were under consideration as of the third reprocessing. The most promising of these were the PAR reaching the ocean surface, and the NDVI over land.

1.3 SOLUTIONS

The algorithmic changes implemented in response to the above stated issues arose from a variety of sources over a period of about two years starting in May 2000. Some of these were already in progress at that time. Others resulted from analysis of specific problems, or were developed, based on new information that became available during the time period. This section lists the algorithm changes (which are described in the other chapters of this volume) and the time frame in which they were developed.

1.3.1 On-orbit Calibration Corrections

By the time of the third reprocessing, a correlation had already been identified between the fluctuations in the band 7 and 8 time response and the focal plane temperature. This allowed for a much simpler temporal correction; however, this modification was not fully developed for operational use at the time. During the next several months, the analysis of the temperature correlation was completed, and a new set of temperature corrections was computed to replace those based on the prelaunch testing. The temporal correction was then revised in the form of a (single) decaying exponential function covering the entire mission. The same functional form was also applied to bands 1–6. The implementation of this in a revised calibration table was completed by December 2000. The exponential function was recomputed periodically using additional lunar calibration data after that time; the calibration was finalized just prior to the fourth reprocessing in July 2002.

The form of the mirror side correction was also revised in this time frame. A time-varying correction, in the form of a series of linear segments, was implemented in November 2000.

In early 2002, analysis of the water-leaving radiances from a mission-long test showed that a residual time drift remained in the clear-water values. At around the same time, analysis of the lunar calibration data indicated a measurable temporal response change in bands 3 and 4 (Kieffer et al. 2002), which were used to normalize the lunar time series for the other bands. A time correction was incorporated into the lunar data normalization, and revised temporal correction functions were computed for all bands. This was completed in March 2002.

1.3.2 MOBY Stray Light Correction

One of the most significant improvements to the SeaWiFS calibration arose from the discovery in early 2001 of a stray light effect in the MOBY data calibration (Clark et al. 2001). It was quickly determined that this effect had caused the measurements at the blue end of the spectrum (bands 1 and 2) to be biased low. Because all of the visible bands are vicariously calibrated using MOBY as the reference, this stray light effect was largely responsible for the observed radiance bias in the *in situ* match-up comparisons, and also contributed substantially to the number of negative L_{WN} values.

The first set of corrected MOBY measurements were received in February 2002. Several additional corrected measurement sets were received prior to the fourth reprocessing, and were incorporated into the final vicarious calibration of the visible bands.

1.3.3 Vicarious Calibration Procedures

In addition to the use of the stray light corrected MOBY data, significant changes were made to the vicarious calibration procedures for the fourth reprocessing. The new level-2 processing software, developed for the third reprocessing, made possible the comparison of radiances at the top of the atmosphere (the *inverse calibration*) instead of

the ocean surface (*forward*) as before. This allowed the calibration to be performed in a single step, instead of iteratively, significantly reducing the processing time required. The inverse calibration procedure was already under development as of the third reprocessing, and was shown to produce consistent results with the forward calibration.

In August 2001, a detailed comparison was performed of the selection and processing procedures for the vicarious calibration and *in situ* match-up comparisons, and a consistent set of procedures was developed. Additional selection criteria for the MOBY data were developed in April and May of 2002, and were used for the final vicarious calibration.

1.3.4 Flags and Masks

A detailed evaluation was undertaken of the flags used as masks for the third reprocessing, beginning in September 2001. Specifically, the objective was to determine the number of observations that were affected by each flag, and whether the flag algorithm could be modified to reduce the number of affected pixels without affecting data quality. This analysis, which continued through December 2001, resulted in the changes made to the stray light flag and the sensor zenith angle limit.

The cloud and ice flag was subjected to multiple changes. In conjunction with the temporal calibration change of band 8, the threshold was adjusted to compensate for the change in average radiance. A correction of the algorithm for air mass was proposed in September 2000. In January 2002, however, a substantial revision was proposed to the cloud and ice algorithm: use of the band 8 surface and aerosol reflectance in place of TOA reflectance. This removed the effect of increasing Rayleigh radiance at high solar zenith angles, which caused the flag to be set for valid, open ocean pixels at high latitudes.

The absorbing aerosol flag was analyzed starting in July 2000, and this revealed some implementation issues that were causing inconsistent performance of this flag. In addition, the thresholds were adjusted to compensate for the vicarious calibration changes in bands 1 and 2.

During the final evaluation of the algorithm changes, it was shown that the speckles were still present in the data, and the revised cloud flag had increased the incidence of the speckles at high latitudes. Analysis of these observations showed that many of them exhibited distinctly nonphysical spectral behavior. As a result, a spectral test was added to the algorithm for the chlorophyll failure flag.

Additional flag changes were made as follows:

- The turbid water flag was revised over the period from November 2001–January 2002, to be based on a threshold applied to the band 6 remote sensing reflectance.
- The high total radiance (high L_t) flag, which was set if any band had a value above the knee in the bilinear gain, was modified in January 2002 to apply this test only to bands 7 and 8.
- The high glint flag was removed as a mask; this change had already been suggested, but not evaluated, by the time of the third reprocessing.

1.3.5 NIR Correction

The effect of the NIR surface radiance correction at low chlorophyll levels was known as of the third reprocessing. A modification was already being designed to phase in the correction around a chlorophyll level of $1\,\mathrm{mg\,m^{-3}}$. This modification was completed by the end of 2001.

A change to the NIR absorption coefficients, to better correspond to the SeaWiFS band passes, was introduced in November 2001. In December 2001, the NIR backscatter model was changed from chlorophyll- to reflectance-based, at a reference wavelength of 670 nm. Improved control of the NIR correction iteration process was completed in February 2002.

1.3.6 NIR Noise Reduction

A method to reduce the effect of NIR band digitization error on the atmospheric model selection was already developed as of the third reprocessing, but had not been accepted for operational use at that time. The general approach of filtering radiances was developed starting in October 1998. It was substantially enhanced in June 2000, and was also applied to the Ocean Color and Temperature Scanner (OCTS) global data processing by the NASA Sensor Intercomparison and Merger for Biological and Interdisciplinary Oceanic Studies (SIMBIOS) Project in 2001. After extensive analysis of the results, it was decided in June 2002 to apply this algorithm only to the 1 km LAC and high resolution picture transmission (HRPT) data, and not the global area coverage (GAC) data.

1.3.7 Miscellaneous Changes

A number of other changes were also made:

1. A modification was developed in April 2001, to use different solar irradiance values for calculations before and after the out-of-band correction was applied to the L_{WN} calculation.
2. The atmospheric model selection algorithm was modified to revert to a fixed model for very clear atmospheres (i.e., band 8 aerosol reflectance below a threshold).
3. In June 2002, a correction to the L_{WN} calculation was implemented for the Fresnel reflectance at the air–water interface.
4. Under certain geometric conditions, certain aerosol models cross over in ϵ *space*, i.e., when plotting ϵ as a function of scattering angle, causing discontinuities when the aerosol path radiances are extrapolated into the visible. A correction was developed, also in June 2002, which identifies these

model crossing conditions and revises the model selection result accordingly.

5. Storing chlorophyll in the level-2 product as a scaled integer introduced artifacts at low chlorophyll values. The solution was to store the level-2 chlorophyll value as a floating point variable instead of an integer.

1.4 TESTING AND EVALUATION

A nearly final set of algorithm changes was implemented by December 2001. At that time, work began on a strategy for systematic testing and evaluation of the results, with many opportunities for review and feedback by the scientific community. This section presents the overall testing approach, the specific test cases run, and a summary of the results.

1.4.1 Testing Approach

The month of May 1999 was selected for the case-by-case evaluation of the algorithm changes. For each case, a number of items were generated:

- Images of daily, 8-day, and monthly binned products;
- Difference and ratio images;
- Difference and ratio histograms;
- Two-dimensional histograms;
- Sample and bin gain-or-loss statistics; and
- A summary of the most significant effects.

These results were posted on the SeaWiFS Reprocessing Web site, and the scientific community was invited to review and comment on the results.

In addition, multiple, mission long tests were run, and were used to generate comparisons of *in situ* matchups, clear water and deep water analyses, and mapped images. All of these results were posted on the Web site as well.

1.4.2 Test Cases

The following describes the test cases that were run. Initially, a baseline run was generated using the configuration for the third reprocessing. Each case was then compared with the previous one to generate the statistics and difference images. The vicarious gains were recomputed for several cases as required.

Case 1, MOBY Stray Light Correction: The new visible band vicarious gains were derived from the MOBY data corrected for stray light effects, along with refinements to the vicarious calibration procedures. The configuration was otherwise identical to that for the third reprocessing.

Case 2, Updated Calibration Table: The new calibration table implements changes in the calibration time dependence (from piecewise quadratic to exponential), temperature corrections and mirror side corrections for all bands. The change also included a re-evaluation of the vicarious gains in bands 1–7, and an adjustment to the cloud mask threshold to compensate for a reduction in the band 8 calibrated radiance.

Case 3, Revised Out-of-Band Correction: The revised out-of-band correction is applied prior to use in downstream computations (e.g., chlorophyll retrieval). A revised set of correction factors was generated using the recently published clear-water reflectance model (Morel and Maritorena 2001).

Case 4, Miscellaneous Changes and Corrections: The high L_t flag, which was previously set when any band exceeded the bilinear calibration *knee* value, was changed to only test the NIR bands, where the increased quantization of the radiance can significantly affect aerosol retrievals. The high L_t flag was applied as a mask at level-3. In addition, the threshold for the high sensor zenith angle flag was increased from 56° to 60°. A new turbid water flag was introduced, but this flag is only informational. This stage in the test sequence also introduced the improved handling of low aerosol conditions, a modified NIR iteration control, and the phase-in of the NIR correction. In addition, the transmittance in the cloud albedo calculation was modified to improve behavior at high solar and viewing angles, and the NIR water-leaving radiance model was updated with new absorption and backscatter coefficients. The cloud albedo threshold was adjusted to compensate for the algorithm change. The cloud albedo changes were superseded by subsequent modifications (Case 7).

Case 5, Change in NIR Correction Method: The NIR correction changed from chlorophyll-based to reflectance-based. This correction, as implemented in the third reprocessing, tended to depress the 510–865 nm Ångström values, which often caused the selection of oceanic aerosol models and resulted in reduced chlorophyll retrievals.

Case 6, Change to Glint Mask Use: This case incorporated the change to eliminate masking based on the high glint flag. At the third reprocessing, a glint correction was introduced for pixels where glint radiance was less than the threshold set to trigger the high glint flag. During preparation for the fourth reprocessing, it was demonstrated that this correction was reasonable up to the level where the high L_t flag is triggered.

Case 7, Improved Cloud Flagging Method: The new cloud flagging algorithm was based on band 8 surface- and aerosol reflectance, which better compensates for the increasing Rayleigh path radiance with solar and viewing angles. The third reprocessing algorithm, based on the TOA reflectance, was found to be overly restrictive at higher solar and viewing angles.

Case 8, Reduce Stray Light Mask: The stray light masking algorithm was changed to reduce the number of stray light masked pixels from three to two before and after a bright target. The original masking correction scheme for stray light (GAC resolution), determined before launch, was conservative with the intention that the masking and

Table 1. The following table shows a summary of the median percent change for each incremental change to the SeaWiFS processing code relative to the previous change. The column headers "M" and "D" denote "Monthly" and "Daily," respectively. The "Total" results are versus the third reprocessing.

	Filled Bins		*Samples*		C_a		$L_{WN}(412)$		$L_{WN}(490)$		$L_{WN}(555)$		$\tau_a(865)$	
Case	*M*	*D*	*M*	*D*	*M*	*D*	*M*	*D*	*M*	*D*	*M*	*D*	*M*	*D*
1	0.6	1.9	2.4	2.8	−6.0	−5.2	17.0	16.5	6.2	6.2	4.7	4.8	0.0	0.0
2	−0.1	−0.4	−0.5	−1.0	1.1	1.1	−1.8	−1.7	−1.4	−1.3	−1.0	−0.9	−3.3	−3.4
3	0.0	−0.2	−0.3	−0.3	−3.7	−3.8	2.3	2.3	−0.2	−0.2	−1.3	−1.4	0.0	0.0
4	0.8	3.4	3.0	3.3	−1.4	−1.5	−0.1	−0.1	0.6	0.5	−0.3	−0.5	0.8	0.9
5	0.0	−0.1	−0.1	−0.1	0.0	0.0	0.0	0.0	0.0	0.0	0.0	0.0	0.0	0.0
6	0.2	0.9	0.8	1 0	0.0	0.0	0.0	0.0	0.0	0.0	0.0	0.0	0.0	0.0
7	1.4	1.5	1.5	1.3	0.0	0.0	0.0	0.0	0.0	0.0	0.0	0.0	0.0	0.0
8	3.0	16.0	16.0	16.0	0.0	0.0	0.0	0.0	0.0	0.0	0.0	0.0	0.0	0.0
9	0.1	0.4	0.4	0.5	3.2	3.2	−0.6	−0.6	−0.6	−0.6	1.0	1.1	−1.2	−1.1
Total	6.0	24.7	24.6	24.3	−7.1	−7.6	17.3	16.7	5.1	4.7	3.6	2.9	−1.3	−3.4

correction schemes be revisited after launch. The change is only implemented for GAC resolution data. Stray light corrections were applied to the additional unmasked pixels.

Case 9: Add Fresnel Transmittance Correction, Chlorophyll Failure Condition Modification, and Final Gains: The normalization of water-leaving radiance was modified to include a correction for Fresnel transmittance through the water–atmosphere interface. In addition, a few other minor changes were introduced at this stage.

The number of match-up points used in the vicarious calibration was further reduced by the exclusion of six points with moderate glint contamination. The effect of removing these points was to very slightly raise the gains (all things being equal). Additionally, four more lunar calibration points were added to the data set used to compute the time dependence correction for the calibration table. This case also included the fix for the model crossing problem.

1.4.3 Cumulative Effects of Changes

Table 1 shows a summary of the median percent change for each incremental change to the SeaWiFS processing code relative to the previous change. The statistics presented include the change in the number of filled bins and the total number of valid samples; the median change in chlorophyll; the L_{WN} values at 412, 490, and 555 nm (bands 1, 3, and 5, respectively); and the aerosol optical thickness (AOT, τ_a) at 865 nm (band 8). The statistics were computed for monthly and daily binned files, using the May 1999 test runs.

The statistics show that the most significant changes were an increase of nearly 25% in the number of valid data samples (with an equivalent change in the number of filled bins in the daily product), and an increase of about 17% in the 412 nm (band 1) L_{WN} values, mainly due to the improvement in the vicarious calibration from the MOBY stray light correction. Also significant is the fact that Cases 6, 7, and 8, which were intended only to increase the number of valid retrievals, had no measurable effect on radiometry.

1.5 OTHER OPTIONS NOT ACCEPTED

During the period between the third and fourth SeaWiFS data reprocessings, a number of algorithm changes were considered, but were either deferred for further analysis or rejected. These are summarized below.

Revised At-launch Gains: Prior to the SeaWiFS launch, two separate calibrations were performed, one by Santa Barbara Research Systems (SBRS) in 1993 and the other by the National Institute of Standards and Technology (NIST) in 1997. The NIST 1997 gains have been used for all processing to date, modified by the vicarious gains determined using the MOBY data (bands 1–6) and atmospheric model assumptions near MOBY (band 7). Recent analysis has shown that the vicarious gains are more consistent with the SBRS 1993 calibration. For ocean data, the vicarious calibration largely cancels out any effect on the bands 1–6 L_{WN} values, but the reflectances would be affected, and vicarious gains are not used for land data processing. The effect of this change was not evaluated in time for the fourth reprocessing.

NIR Band Alternative Calibration Schemes: The calibration for the NIR bands has been based on the prelaunch gain for band 8 since launch, and the vicarious calibration based on atmospheric model assumptions for band 7 since shortly after launch. Several alternative approaches were investigated, including use of a single model, or selection of models based on *in situ* AOT measurements, for the band 7 vicarious calibration; vicarious calibration of both bands 7 and 8 using the AOT measurements; and incorporation of local wind speed measurements at the MOBY location. None of these were found to produce improvements over the current approach, although the AOT-based vicarious

calibration improved the AOT matchups performed by the SIMBIOS Project.

Alternate Cloud Shadow Algorithm: The SeaWiFS low water-leaving radiance flag is used to detect cloud shadows based on a threshold on the band 5 L_{WN} values. An algorithm based on multiple bands might be more robust, but this was not investigated for the fourth reprocessing.

Revised Solar Irradiance Model: The current solar irradiance model used in the algorithms is based on the work of Neckel and Labs (1984). Other projects such as the Moderate Resolution Imaging Spectroradiometer (MODIS), have switched to a more recent model developed by Thuillier et al. (1998). Thuillier et al. have also been working on additional refinements to the model, and a new version has been developed (Thuillier et al. 2003). A decision was made to postpone implementation of the so-called *Thuillier model* until the latest spectrum is officially published and the effects on SeaWiFS products are fully quantified.

Alternative Aerosol Model Selection Algorithm: The current aerosol model selection algorithm is designed to choose 2 models from the full set (currently 12) and interpolate linearly between them [the ratio of band i to band j is hereafter denoted as $\lambda_{i/j}$], based on the ratio of band 7 to band 8 ($\lambda_{7/8}$) single-scattering aerosol reflectance (ϵ) value. This approach has problems under several commonly encountered conditions:

a. Two models have nearly identical NIR band ratios for certain geometric conditions, though they differ in the visible bands.

b. The aerosol reflectance values for the visible bands change discontinuously when the model pairs change.

c. The uncertainty in the ϵ value is large for small NIR band values, causing unnecessary model switching.

Alternative model selection algorithms were discussed to reduce the effect of these problems, by using more than two models. One scheme proposed was a gaussian weighing of multiple models; tests of this did not work well, and the suspected cause was a nonuniform distribution of the models in ϵ space. Another approach has been proposed which would involve a weighted linear fit to multiple models in the vicinity of the computed ϵ value. Investigation of this approach was in progress at the time of the fourth reprocessing. A simple fix for a specific model selection problem was described in Sect. 1.3.7, item 4.

NO_2 Correction: At the fifth SIMBIOS Science Team Meeting (January 2002), it was suggested that NO_2 absorption may be significant. The current atmospheric correction algorithm does not consider NO_2 absorption, however, the topic bears future study.

Pressure Dependence of the Band 7 Oxygen Absorption Correction: The current oxygen absorption correction for band 7 is independent of atmospheric pressure. The effect of pressure on this correction is small and likely within the uncertainty of the correction. The effort involved was determined to be unwarranted for the fourth reprocessing.

f/Q Correction: The SeaWiFS Project has been working with D. Antoine and A. Morel on the issue of the bidirectional reflectance at the water's surface, f/Q, since October 1999. The approach has been to evaluate the effect of the correction on reducing viewing angle dependencies in the L_{WN} values. Thus far, the algorithm has not been found to improve the quality of the SeaWiFS products. The results of the f/Q correction have been provided to Antoine and Morel to continue the investigation.

Revert to At-Launch $K_d(490)$ Algorithm: The $K_d(490)$ (diffuse attenuation coefficient at 490 nm) algorithm was changed with the third reprocessing, from using a ratio of $\lambda_{2/5}$ to a ratio of $\lambda_{3/5}$. This change was made because of uncertainties in the band 2 radiances. With the calibration now based on the stray light corrected MOBY data, the uncertainties in the band 2 radiances have been reduced. The at-launch algorithm for $K_d(490)$ is more sensitive, particularly for the lower values found in open ocean conditions. For these two reasons, it was proposed that the at-launch algorithm be re-implemented. Preliminary analysis showed there was general agreement between the current algorithm and the previous version. In turbid waters, however, band 2 radiances become negative more often than band 3. This causes the $\lambda_{2/5}$ algorithm to produce unrealistically high values. For this reason, the decision was made to continue with the $\lambda_{3/5}$ algorithm for this reprocessing.

Log-Scaled Chlorophyll: A proposal to replace the chlorophyll values with their logarithm in the level-2 product was considered, to account for the log-normal distribution of chlorophyll. This was initially a response to the artifacts resulting from the use of scaled integers (Sect. 1.3.7). It also reduced the effect of anomalous chlorophyll values (Sect. 1.2.5). The change was determined to be unacceptable because of the effect on global chlorophyll statistics, and the floating point storage solution was implemented instead.

1.6 CONCLUSIONS

The SeaWiFS Project undertook the preparation for the fourth reprocessing with a number of issues to resolve. More importantly, perhaps, the Project decided from the outset that each change would be accompanied by a technical justification; the effects of each change would be clearly demonstrated by testing, analysis, and evaluation; and the scientific community would be engaged to the maximum extent possible throughout. Some changes were already in progress as of the third reprocessing, while others were proposed when the effort was nearly completed. Most were developed from analyses conducted by Project members, but a few were developed from work done for other sensors, and one (e.g., the MOBY stray light correction) came about as a result of external events that could not have been foreseen in advance. Several promising ideas were ultimately shown to produce no tangible benefit.

The results posted from the tests and evaluations show substantial improvement in overall data quality in a number of areas compared to the third reprocessing. Nonetheless, the number of potential changes deferred for further analysis is a clear indication that further improvements are possible. In addition, some issues (e.g., negative L_{WN} values and absorbing aerosols) were only partially addressed by the improvements described in this volume. Future changes will be implemented following the same approach to data analysis, algorithm development, testing, and evaluation as summarized in this chapter.

Chapter 2

Changes to the On-Orbit Calibration of SeaWiFS

Robert E. Eplee, Jr., Robert A. Barnes,
and Frederick S. Patt
Science Applications International Corporation
Beltsville, Maryland

Abstract

Monthly lunar calibrations and daily solar calibrations are used to track the on-orbit stability of the radiometric calibration of the SeaWiFS instrument. Analyses of these data by the SeaWiFS CVT since the third reprocessing showed residual errors in the detector temperature corrections, the lunar calibration time corrections, and the mirror side reflectance corrections. These analyses, and the resulting changes to the on-orbit calibration methodologies, are presented in this chapter. Revised detector temperature corrections allowed the lunar calibration time series to be characterized by a single, time-dependent exponential function. A time correction was applied to the normalization of the lunar calibration time series; time-dependent mirror side reflectance corrections were also implemented. These changes to the calibration methodologies enabled the production of a more robust on-orbit calibration of SeaWiFS for the fourth reprocessing of the SeaWiFS mission data set.

2.1 INTRODUCTION

The SeaWiFS CVT undertook extensive analyses of the SeaWiFS on-orbit calibration data and ocean data in preparation for the fourth reprocessing of the mission data set. These analyses showed three sources of residual errors in the on-orbit calibration data: a) an annual periodicity in the lunar calibration time series for some bands, b) a residual time drift in the lunar calibration data, and c) a change in the half-angle mirror side reflectances with time. A number of changes were implemented to the on-orbit calibration methodologies to address these residuals. These changes, which have resulted in a more robust on-orbit calibration of SeaWiFS, are detailed in the following sections of this chapter.

2.2 TEMPERATURE CORRECTION

The ambient temperatures at which the SeaWiFS detectors operate are affected by the solar insolation on the spacecraft. The SeaWiFS calibration incorporates corrections for variations in the radiometric response of the instrument with changing detector temperatures (Barnes et al. 1994). The prelaunch corrections do not fully account for the variation in radiometric response with changing detector temperatures observed over the course of a year. Examination of the SeaWiFS lunar calibration time series (Fig. 1) shows an annual periodicity in some bands which corresponds to the variation in detector temperatures (Fig. 2) as the Earth–sun distance changes over a year. Through the third reprocessing, the CVT dealt with these annual periodicities with a series of piecewise quadratic and linear segments in the time correction applied to the ocean data (Barnes et al. 2001 and Eplee and Barnes 2000). This approach required regular updates to the operational calibration table.

For the fourth reprocessing, the periodicities in the lunar time series were used to compute revised detector temperature correction factors for the SeaWiFS calibration. The SeaWiFS level-1b calibration equation includes a correction for variations in the radiometric response of the detectors as a function of temperature, f_T (Eplee and Barnes 2000). This correction has the form

$$f_T(\lambda) \;=\; 1 \;+\; K_2(\lambda)(T - T_{\mathrm{ref}}), \qquad (1)$$

where λ is the wavelength, K_2 is the temperature correction factor, T is the detector temperature from the sensor output data, and T_{ref} is the detector reference temperature (20°C).

During the prelaunch calibration of SeaWiFS, the temperature correction factors were derived for each band over a limited range of detector temperatures. These values are shown in Table 2. To investigate the periodicities in the lunar calibration time series, each band in the time series was fit to a decaying exponential function of time. The residuals of these fits showed linear dependencies on detector temperature. The resulting slopes of the fit residual versus detector temperature trends were used to revise the

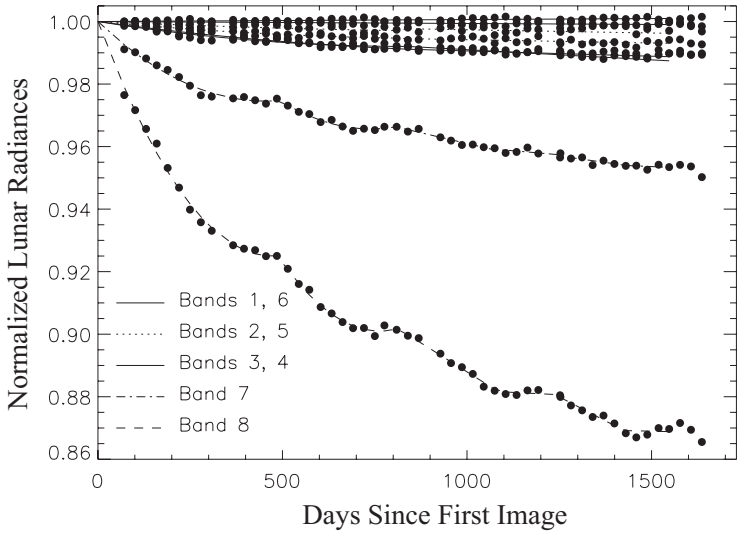

Fig. 1. The initial lunar calibration time series. The lines are fits to the data.

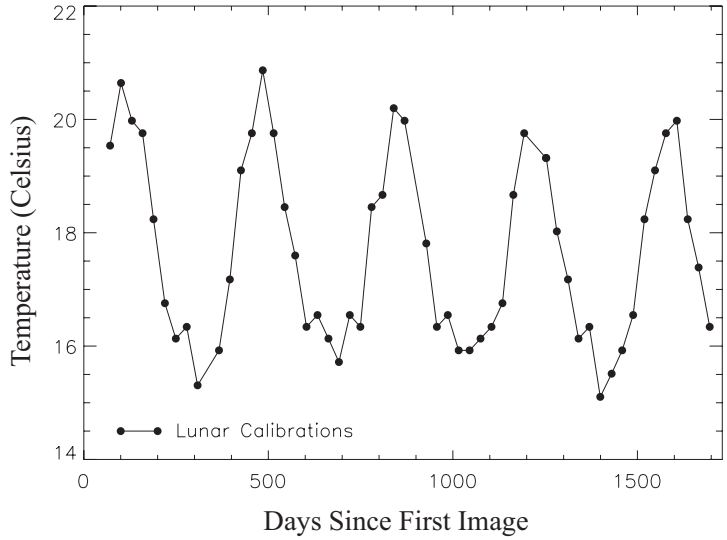

Fig. 2. The band 7 and 8 detector temperatures during lunar calibrations.

temperature correction factors. As shown in Table 2, the changes in the correction factors varied with band, with the largest changes affecting bands 6–8.

Table 2. The detector temperature correction factors are shown.

Band	*Prelaunch* K_2 $\left[(^\circ\mathrm{C})^{-1}\right]$	*Revised* K_2 $\left[(^\circ\mathrm{C})^{-1}\right]$
1	9.01×10^{-4}	7.664×10^{-4}
2	5.85×10^{-4}	5.540×10^{-4}
3	4.20×10^{-4}	3.392×10^{-4}
4	3.90×10^{-4}	3.057×10^{-4}
5	3.91×10^{-4}	3.045×10^{-4}
6	1.51×10^{-4}	-3.443×10^{-5}
7	1.06×10^{-4}	-4.495×10^{-5}
8	7.8×10^{-5}	-1.485×10^{-3}

These revised temperature correction factors were used to reprocess all of the lunar calibration data. The resulting time series (Fig. 3) no longer showed the annual periodicities. The revised lunar calibration time series was fit with a single decaying exponential function of time, $f(t)$, for each band. This function has the form

$$f(\lambda, t) \;=\; a_0(\lambda) \;-\; a_1(\lambda)\left[1 \;-\; e^{-a_2(\lambda)(t-t_0)}\right], \quad (2)$$

where t is the time of the calibration, t_0 is the reference time for the time series, a_0 is the initial value of the function, a_1 is the difference between a_0 and the asymptotic value of the function, and a_2 is the time constant of the function.

As time increases, the function approaches the asymptotic value $a_0 - a_1$. These time correction functions were incorporated into the revised calibration table used in the

fourth reprocessing. Unless a significant change in the behavior of the radiometric response of the detectors occurs, piecewise updates to the calibration table should not be necessary for operational processing of the ocean data.

2.2.1 Effects Over One Orbit

The effects of the revised detector temperature corrections can be observed over a single orbit. As part of the the fourth reprocessing analysis effort, these effects were examined for one orbit on 1 May 1999 for bands 7 and 8. Bands 7 and 8 reside on a single focal plane, for which the instrument telemetry provides one focal plane temperature measurement.

The detector temperature for bands 7 and 8 for a typical orbit on 1 May 1999 is shown in Fig. 4 as a function of the latitude of the center pixel of the scan line. The digitization of the temperature is 0.2°C. The behavior of the other bands is similar. During the part of the orbit when science data are not being collected, the so-called *back orbit,* the detectors are turned off and the focal plane heater is turned on. As the spacecraft crosses over the North Pole, the focal plane heater is turned off and the detectors are turned on. Typically, the focal plane heater keeps the detectors at a higher temperature than that of their normal operation. As shown in Fig. 4, the detector temperature falls from the initial temperature of approximately 16.7°C to a more typical temperature of approximately 14.1°C within about the first 5° of latitude. The temperature continues to fall to approximately 13.7°C over the next 15° of latitude. This temperature, which is the nominal operating temperature of the detectors for this orbit, is stable through 55° of latitude. As the spacecraft approaches the equator, solar heating raises the temperature to approximately 13.9°C, and then to approximately 14.1°C. For most of the orbit, from 75°N to 60°S, the detector temperature is stable to within two counts (0.4°C).

The detector temperature corrections for bands 7 and 8 are shown over the orbit as functions of latitude in Fig. 5. The prelaunch corrections are plotted as dashed lines and the revised corrections are plotted as solid lines. The variation in the prelaunch corrections over the orbit is essentially unity. Over the temperature range of 14–17°C, the revised temperature correction for band 8 is approximately 0.05% per count and the correction for band 7 is approximately 0.02% per count. The change in the temperature correction for band 8 is approximately 0.1% over the course of the orbit. Because the band 8 radiance is used in the atmospheric correction algorithm to determine the aerosol abundance (Eplee et al. 2001, and Robinson and Wang 2000), the decrease in radiance in the Southern Hemisphere may affect the retrieved aerosol abundance between the third and fourth reprocessings for a single pixel.

The combined temperature and time corrections affect the total radiances. In this analysis, single time corrections for bands 7 and 8 were computed for 1 May 1999 and were used to scale the detector temperature corrections over the orbit. The $\lambda_{7/8}$ ratio, normalized by the vicarious gain of band 7, was used to determine the aerosol type in the atmospheric correction algorithm (Eplee et al. 2001 and Robinson and Wang 2000). [The gain of a given band is hereafter denoted as G_i, e.g., G_7 is the vicarious gain for band 7.] Figure 6 shows the changes in the normalized radiance ratio ($G_7 \times \lambda_{7/8}$) between the third and fourth reprocessings as a function of latitude. The plot shows that for the Southern Hemisphere the changes in the radiance ratio between the third and fourth reprocessings may cause changes in the retrieved aerosol type. The changes in aerosol retrievals between the third and fourth reprocessings, shown in Figs. 5 and 6, will propagate through to changes in the retrieved normalized water-leaving radiances and chlorophyll concentrations.

2.2.2 Effects Over Time

The effects of the revised detector temperature corrections and resulting exponential time correction are observed on a monthly basis in the lunar calibration data. As part of the fourth reprocessing analysis effort, these effects were examined daily for bands 7 and 8, where the temperature correction revisions are the most significant.

Figure 7 shows the mean daily detector temperature for bands 7 and 8 over the course of the mission. The temperatures range from 14–20°C on an annual cycle as the Earth–sun distance changes. The combined temperature and time correction to the radiances for band 8 over the course of the mission are shown in Fig. 8. The prelaunch temperature correction and quadratic time correction (the third reprocessing) are shown as dashed lines and the revised temperature correction and exponential time correction (the fourth reprocessing) are shown in solid lines. Figure 9 shows the corrections for band 7. For both bands, the effect of the revised temperature correction on the combined radiance correction is apparent.

Bands 7 and 8 are used for atmospheric correction of the ocean data. The band 8 radiance is used to determine the aerosol abundance, and the $L(\lambda_{7/8})$ value (normalized by G_7), is used to determine the aerosol type. Figure 10 shows the changes in the normalized radiance ratio $[G_7 \times L(\lambda_{7/8})]$ between the third and fourth reprocessings as a function of time. At any point during the mission, changes in the band 8 radiance and in the radiance ratio between the third and fourth reprocessings may result in changes in the retrieved aerosol abundance and type for a given pixel. These changes in the aerosol retrievals will propagate through to changes in the retrieved normalized water-leaving radiances and chlorophyll concentrations.

2.3 LUNAR NORMALIZATION

For one analysis of a fourth reprocessing mission test, mean global L_{WN} values in bands 1–6 were computed from

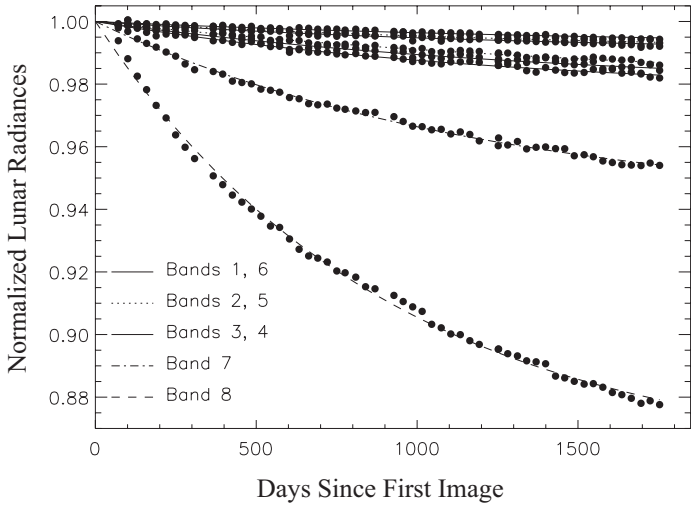

Fig. 3. The revised lunar calibration time series. The lines are fits to the data.

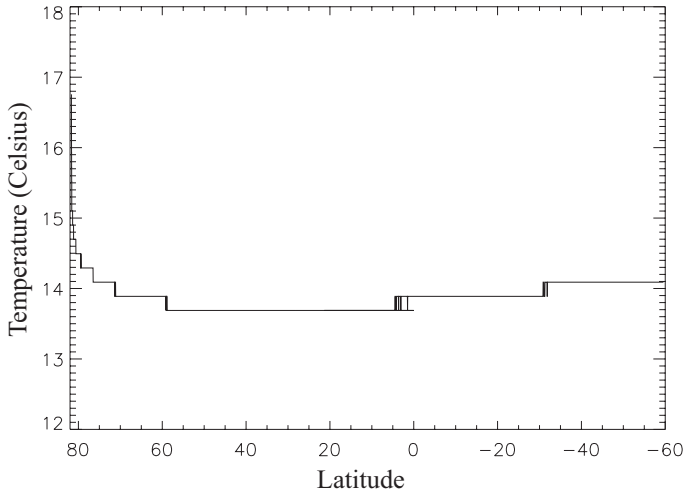

Fig. 4. Band 7 and 8 detector temperatures are plotted over one orbit from 1 May 1999.

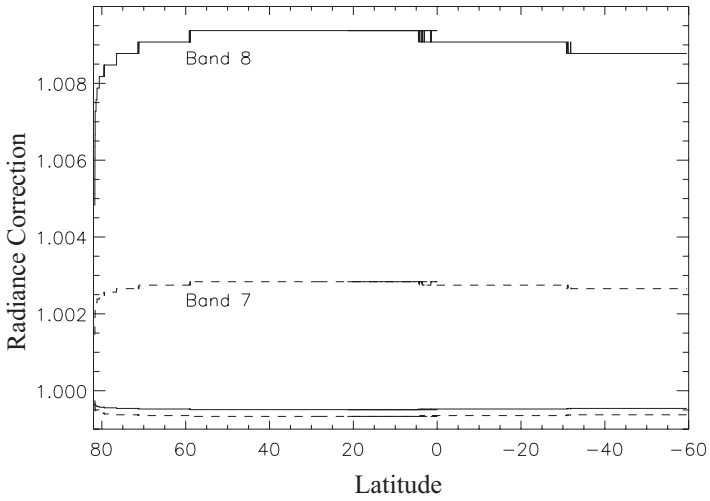

Fig. 5. The band 7 and 8 detector temperature corrections are plotted over the orbit. The two lower lines show the initial corrections. The two upper lines show the revised corrections.

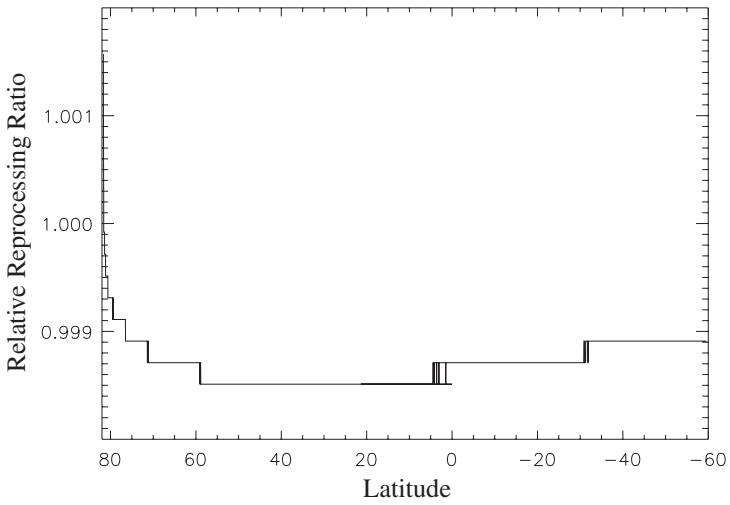

Fig. 6. Relative changes in the $L(\lambda_{7/8})$ values versus latitude resulting from the new temperature correction in the fourth reprocessing.

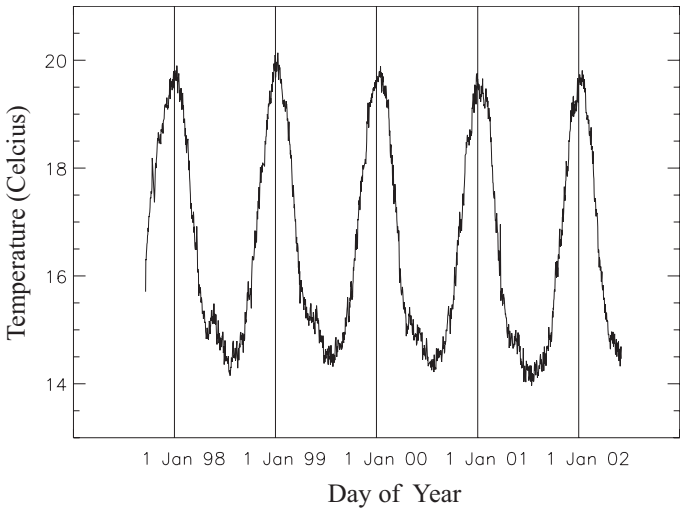

Fig. 7. The band 7 and 8 detector temperatures are plotted over the mission.

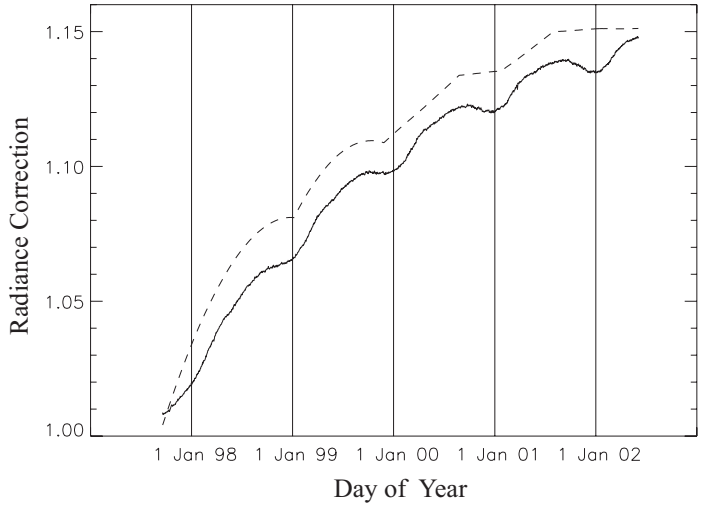

Fig. 8. The band 8 combined time and temperature corrections are plotted over the mission. The dashed line shows the initial corrections. The solid line shows the revised corrections.

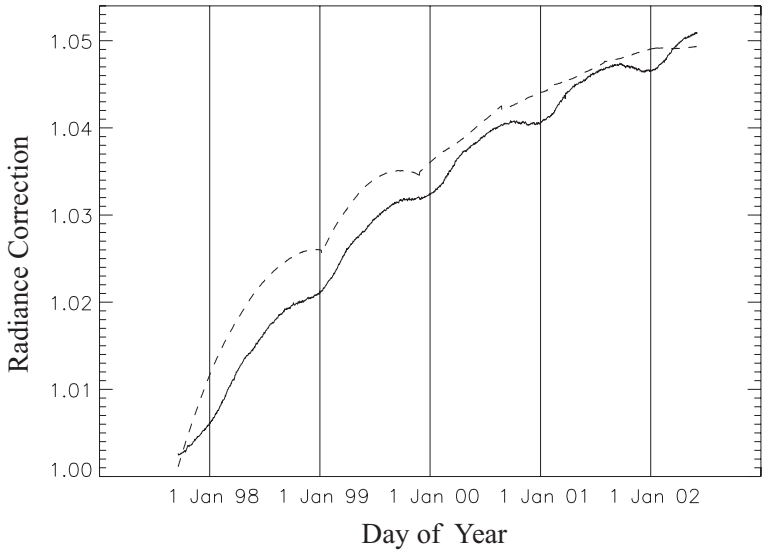

Fig. 9. The band 7 combined time and temperature corrections are plotted over the mission. The dashed line shows the initial corrections. The solid line shows the revised corrections.

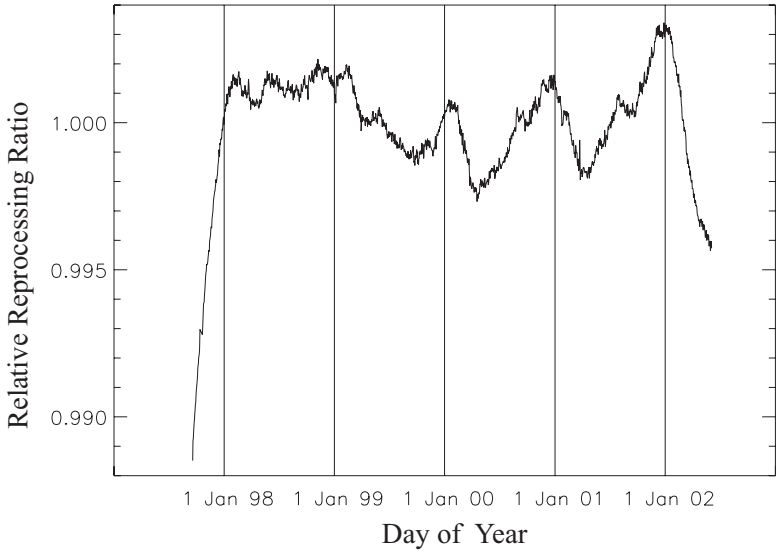

Fig. 10. Relative changes in the $L(\lambda_{7/8})$ values versus time resulting from the new temperature correction in the fourth reprocessing.

the 8-day composite files for clear water (water with a depth of at least 1 km and with a chlorophyll concentration of less than 0.15 mg m^{-3}). The mean radiances in clear water should be constant with time if the radiometric calibration of the instrument is stable (Eplee et al. 2001, and Eplee and McClain 2000). This analysis showed decreases in the radiances for bands 1–6 of several percent over the course of the mission. Figures 11 and 12 show the clear water time series for bands 3 and 5 as dashed lines. Band 3 exhibited a change of -2% over 1,000 days and -3.4% over the mission (a rate of change of -1.9×10^{-5} per day). Band 5 exhibited a change of -2.6% over 1,000 days and -4.4% over the course of the mission (a rate of change of -2.5×10^{-5} per day). These results imply that there was a small residual decrease in the radiometric response of SeaWiFS with time that was not corrected by the previous lunar calibration-based time corrections of the SeaWiFS data. With 4.5 years of data available, small residual drifts can become significant.

The CVT, in analyzing the lunar data to derive the corrections for the instrument, references the lunar calibration time series to the mean of the observations for bands 3 and 4 (Barnes et al. 2001, and Eplee and Barnes 2000). This normalization is done to reduce the systematic noise in the lunar observations which arises from the lack of understanding of how lunar libration affects the long term measurements of the moon. The initial assumption was that the mean of bands 3 and 4 did not change with time. The clear water analysis shows that this assumption is incorrect.

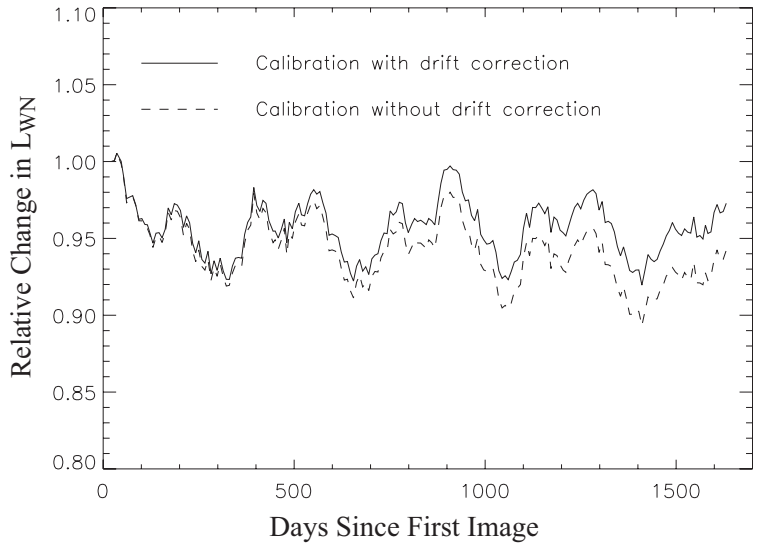

Fig. 11. The band 3 global clear water radiances are plotted over the mission. The radiances are mean values computed for all pixels where the water depth is greater than 1 km and the chlorophyll concentration is less than $0.15\,\mathrm{mg\,m^{-3}}$.

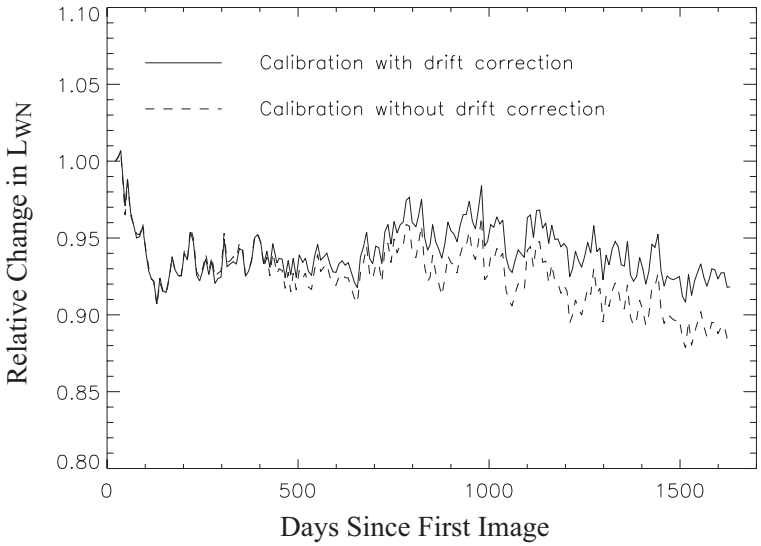

Fig. 12. The band 5 global clear water radiances are plotted over the mission. The radiances are mean values computed for all pixels where the water depth is greater than 1 km and the chlorophyll concentration is less than $0.15\,\mathrm{mg\,m^{-3}}$.

Recently, a comparison of the first 50 SeaWiFS lunar measurements with the United States Geological Survey (USGS) Robotic Lunar Observatory (ROLO) lunar irradiance model (Kieffer et al. 2002) verified that bands 3 and 4 have small drifts with time. The comparisons show that, on average, the radiometric responses of bands 3 and 5 have been decreasing at a rate of 0.35% per 1,000 days, or 0.60% over the course of the mission. The effect of this time drift on the L_{WN} values would be an order of magnitude larger. To correct the residual drift in the SeaWiFS time correction, a time correction of -3.5×10^{-6} per day was applied to the mean of bands 3 and 4 before the mean was used to normalize the lunar time series. The overall time corrections for bands 1–8 were recomputed and the vicarious calibration of SeaWiFS were run again.

The fourth reprocessing was run with the updated time correction and the 8-day composite clear water analysis was rerun. This analysis showed no significant changes in bands 1–6 over the course of the mission. Figures 11 and 12 show the updated clear water time series for bands 3 and 5 as solid lines. Band 3 exhibited a change of +0.16% over 1,000 days and +0.27% over the course of the mission (a rate of change of $+1.5 \times 10^{-6}$ per day). Band 5 exhibits a change of −0.38% over 1,000 days and −0.64% over the course of the mission (a rate of change of -3.5×10^{-6} per day). Any residual time drift in the instrument calibration was reduced by a factor of 8–10.

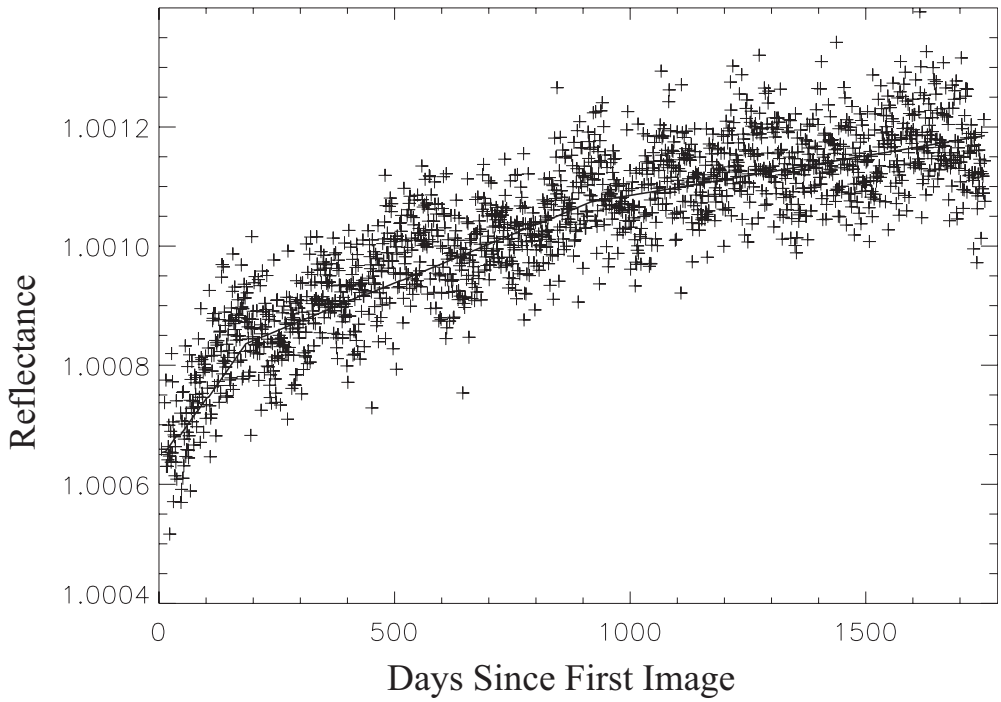

Fig. 13. The mirror side A reflectances for band 1 are plotted over the mission. The lines are the three piecewise linear fits to the data.

2.4 MIRROR SIDE CORRECTIONS

The SeaWiFS level-1b calibration equation includes a correction for the different reflectances of the two sides of the instrument's half-angle mirror (Eplee and Barnes 2000). Over the course of the mission, the SeaWiFS mirror side reflectances have changed at the one-count level, giving rise to artifacts in the ocean data which are visible on close examination. Through the third reprocessing, the problem was addressed by updating the operational calibration table with step-function changes to the mirror side correction factors. For the fourth reprocessing, the mirror side reflectance time series was fit with a set of three piecewise linear corrections. An example reflectance time series is shown for band 1, mirror side A in Fig. 13. The piecewise linear corrections were incorporated into the revised calibration table used in the fourth reprocessing, thus minimizing the future updates required for the operational calibration table.

2.5 SUMMARY

Several changes were implemented in the SeaWiFS on-orbit calibration methodology. Periodicities in the lunar calibration time series were used to revise the detector temperature corrections, thus allowing the revised time series to be fit by a single decaying exponential function of time. Comparisons were made of the SeaWiFS lunar measurements to the USGS ROLO lunar irradiance model to develop a time correction for the lunar data normalization. Time-dependent mirror side reflectance corrections were also implemented. These changes in calibration methodology resulted in a more robust on-orbit calibration of SeaWiFS for the fourth reprocessing of the mission data set. An additional result of these changes is that fewer updates to the operational calibration table will be required to maintain a stable calibration of the SeaWiFS ocean data.

Chapter 3

Changes to the Vicarious Calibration of SeaWiFS

Robert E. Eplee, Jr., and Robert A. Barnes
Science Applications International Corporation
Beltsville, Maryland

Sean W. Bailey
Futuretech Corporation
Greenbelt, Maryland

P. Jeremy Werdell
Science Systems and Applications, Incorporated
Lanham, Maryland

Abstract

The SeaWiFS Project vicariously calibrates the visible bands of the instrument against in-water measurements from MOBY in order to achieve the necessary calibration accuracy for the SeaWiFS retrievals of water-leaving radiances. The SeaWiFS CVT implemented several changes in the vicarious calibration procedure for the fourth reprocessing of the SeaWiFS mission data set. The most significant change is the use of stray light corrected MOBY data in the vicarious calibration. More stringent data quality screening criteria were also implemented for both MOBY and SeaWiFS data to determine the vicarious calibration matchups. Finally, an inverse vicarious calibration procedure was implemented in which the vicarious gains are computed at the top of the atmosphere. The SeaWiFS TOA radiances are compared with MOBY water-leaving radiances that have been propagated to the top of the atmosphere using the SeaWiFS-retrieved atmospheric correction parameters. These changes to the vicarious calibration procedure enabled the production of a more robust set of vicarious gains for the fourth reprocessing of the SeaWiFS mission data set.

3.1 INTRODUCTION

The SeaWiFS CVT implemented several changes in the SeaWiFS vicarious calibration procedure for the fourth reprocessing. The *in situ* measurements are provided by stray light corrected MOBY data. The SeaWiFS data is composed of 101×101 pixel extracted scenes (subscenes) centered on MOBY. More stringent data quality screening criteria were imposed on both the MOBY and SeaWiFS data sets. Vicarious gains were generated using the inverse calibration procedure. These changes are detailed in the following sections of this chapter.

3.2 STRAY LIGHT CORRECTION

In vicariously calibrating SeaWiFS, the assumption is made that the uncertainties in the MOBY radiances are small (Eplee et al. 2001). Analyses of the MOBY data performed by the MOBY Project has shown that stray light within the instrument is biasing the MOBY measurements in the blue end of the visible spectrum (Clark et al. 2001). As part of an ongoing intra-agency collaboration, the MOBY Project is working with NIST to characterize the stray light within the MOBY spectrometers and to develop stray light corrections for the MOBY data. The MOBY Project plans to reprocess the entire MOBY time series, starting with the more recent data. The full set of stray light corrected data over the time range of November 1999 to March 2002 were implemented, along with targeted match-up data from September 1997–November 1999, into the vicarious calibration for the fourth reprocessing. The revised vicarious gains provide water-leaving radiances (L_W) that are higher for bands 1 through 5 (555 nm), compared with the gains for the third reprocessing.

3.3 DATA SCREENING PROCEDURES

Before matchups between MOBY and SeaWiFS can be used in vicarious calibration, both data sets must be screened for data quality. The data screening procedures for both data sets have been enhanced for the fourth reprocessing.

MOBY-derived values of L_W are computed by propagating the upwelling radiance (L_u) measurements made at depth to the surface using the diffuse attenuation coefficient (Clark et al. 2001). Measurements of L_W computed from the L_u measurement at the top arm of MOBY (1.5 m depth) were compared to those computed from the L_u measurement at the middle arm (5 m depth). The majority of these measurement pairs are in good agreement; however, divergence between the two water-leaving radiances on the order of 5–30% can occur. These are likely the result of unfavorable sky and or sea conditions. Consequently, the following exclusion criteria for MOBY data were implemented:

1) Data from both the top and middle arms must exist;, and
2) The combined uncertainty in the L_W measurements for all bands from both arms must be less than 10%, as determined by the square root of the sum of the squared absolute percent differences for bands 1–5, corrected for the cosine of the solar zenith angle.

The currently available set of stray light corrected MOBY data has yielded 163 points where the skies are clear over MOBY at the time of the SeaWiFS overpass (Fig. 14). The exclusion criteria imposed on the MOBY data have reduced the number of matchups for the vicarious calibration to 45. Further data will be incorporated into future vicarious calibrations of SeaWiFS as additional stray light corrected MOBY data become available and as future refinements of the MOBY stray light correction are implemented. In all probability, these additions to the match-up data set will not significantly alter the results obtained for the fourth reprocessing.

The SeaWiFS match-up data consist of 101×101 pixel subscenes centered on the MOBY location. The size of these extracts ensures that stray light within SeaWiFS will be handled properly by the level-2 conversion software in the vicinity of MOBY. The analysis for each matchup is performed on 5×5 pixel subscenes centered on the MOBY location. Each subscene is checked for data quality, screening out matchups for clouds and cloud shadows, stray light, sun glint, high satellite and solar zenith angles, high L_t in bands 7 and 8, and aerosol optical depths greater than 0.1. All 25 pixels in a subscene are required to be clear for the matchup to be used in the vicarious calibration. These quality constraints imposed on the SeaWiFS data have reduced the number of matchups to 23. The vicarious calibration used in the fourth reprocessing is based on 23 SeaWiFS–MOBY matchups selected from the original pool of 163 potential matchups.

3.4 CALIBRATION METHODOLOGY

In order to reduce the uncertainty in the vicarious gains, the vicarious calibration procedures for the fourth reprocessing were modified. The major change was switching from the forward vicarious calibration procedure, which compares the MOBY and SeaWiFS data at the sea surface, to an inverse calibration procedure, which makes the comparison at the top of the atmosphere. The calibration methodologies discussed here apply to the SeaWiFS visible bands, bands 1–6. The vicarious calibration of band 7, was performed for the fourth reprocessing to optimize the retrieval of the aerosol optical properties, as described in Eplee et al. (2001).

The forward vicarious calibration procedure compares normalized water-leaving radiances (L_{WN}) between SeaWiFS and MOBY to determine the vicarious gains for SeaWiFS bands 1–6. For a given matchup, the L_{WN} values for SeaWiFS, $L(\lambda_S)$, is averaged over the 5×5 pixel subscene and this average value $L(\lambda_S)$ is divided by the MOBY radiance $L(\lambda_M)$ for that matchup. The mean of this ratio, $L(\lambda_{S/M})$, is computed over all of the individual matchups. The vicarious gain for each band is adjusted iteratively over multiple runs of level-2 conversion software on the match-up data set until the mean $L(\lambda_{S/M})$ value converges to unity. The forward vicarious calibration procedure allows the effects of iterative NIR correction algorithms to be incorporated into the vicarious gains. The vicarious gains were derived for the third and previous reprocessings using the forward vicarious calibration procedure (Eplee et al. 2001).

The inverse vicarious calibration procedure compares TOA radiances between SeaWiFS and MOBY to determine the vicarious gains for SeaWiFS bands 1–6 (Fig. 15). For a given matchup, the atmospheric correction parameters retrieved for the SeaWiFS data are used to normalize the water-leaving radiances measured by MOBY and to propagate the resulting normalized water-leaving radiances to the top of the atmosphere. For the matchup, the vicarious gains are computed from the $L_t(\lambda_{S/M})$ values in each pixel, averaged over the 5×5 subscene. The overall vicarious gains are the means of the gains computed for the individual matchups.

The inverse vicarious calibration procedure generates gains which agree with those produced by the forward calibration to within 0.04% for the same calibration conditions. At the same time, the inverse calibration offers a number of advantages over the forward calibration. The inverse calibration runs more quickly than the forward calibration, because the gains are computed directly from a single run of the level-2 conversion software. The inverse calibration allows the effect of an instrumental offset to be investigated, although no evidence of an offset has been observed to date. Additionally, the inverse calibration preserves spectral shape information in the matchups by computing a set of gains for each matchup. The forward calibration computes the gains from the mean of the match-up ratios, thus diluting the spectral shape information. The only drawback to the inverse calibration procedure is that it cannot incorporate the effects of iterative NIR correction algorithms. Consequently, the inverse calibration procedure can only be used when the NIR correction algorithms

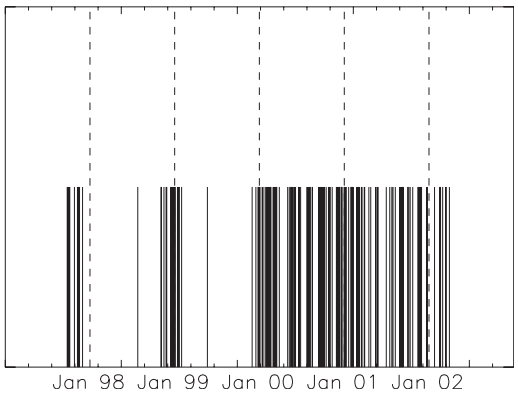

Fig. 14. Current SeaWiFS–MOBY matchups are shown. The distribution of the matchups in time is primarily due to the availability of stray light corrected MOBY data.

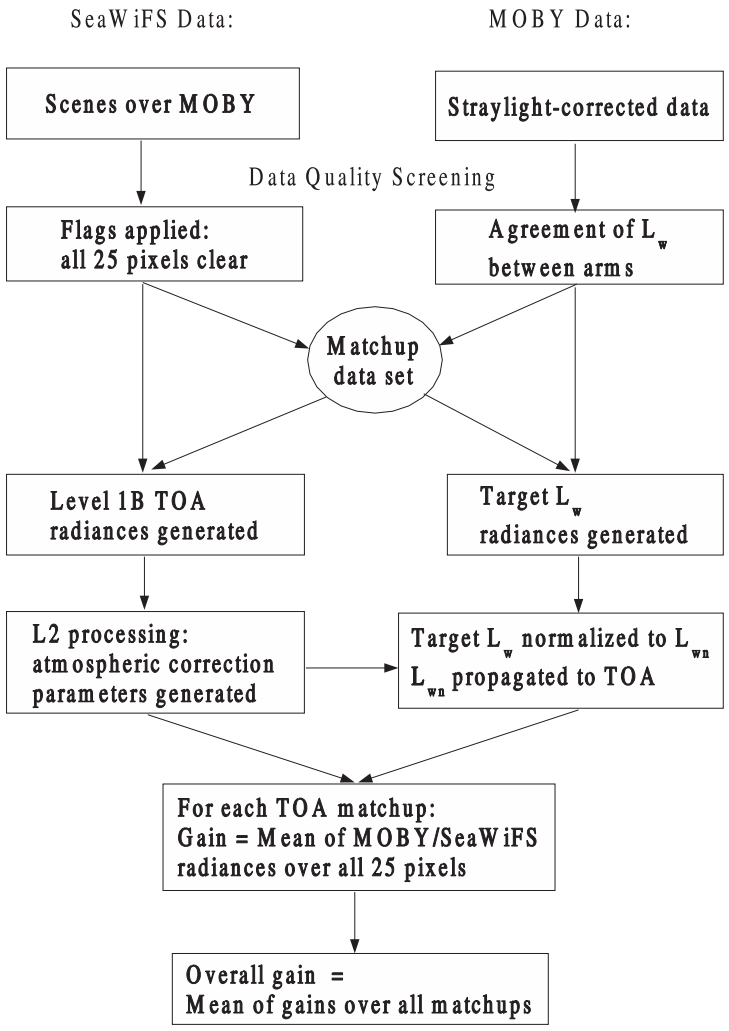

Fig. 15. The diagram shows how SeaWiFS and MOBY data are used to compute vicarious gains for SeaWiFS from ratios of TOA radiances.

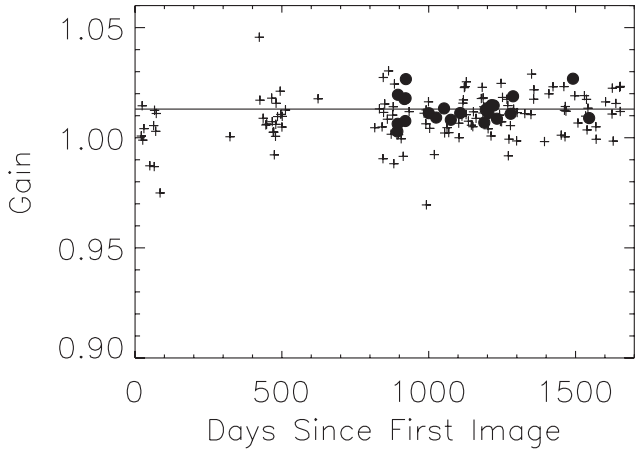

Fig. 16. The vicarious gains for band 1 are shown. The full match-up data set is represented by pluses, while the matchups used in the vicarious calibration are represented by filled circles. The horizontal line shows the vicarious gain for the band.

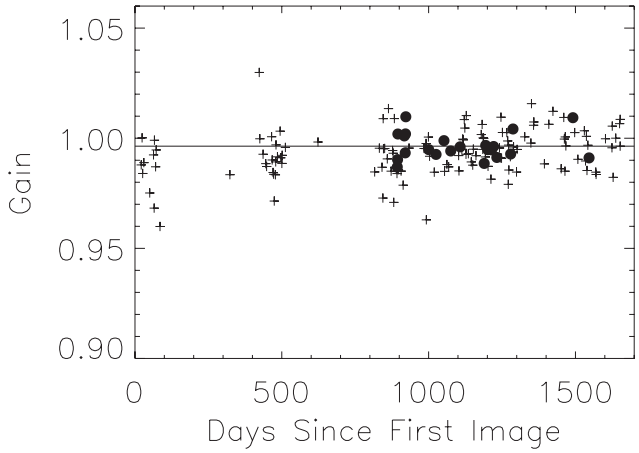

Fig. 17. The vicarious gains for band 2. The symbols used are the same as in Fig. 16.

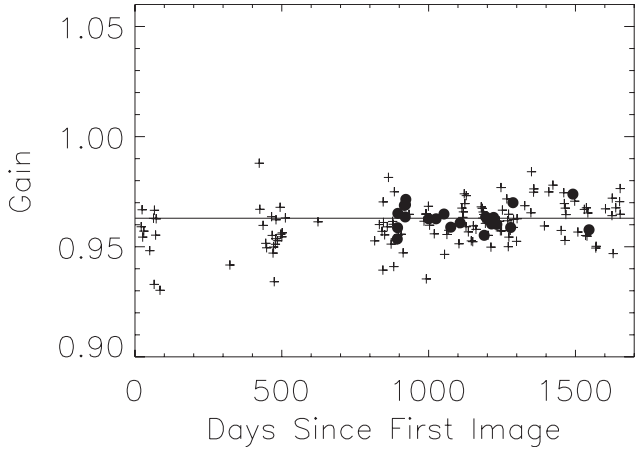

Fig. 18. The vicarious gains for band 3. The symbols used are the same as in Fig. 16.

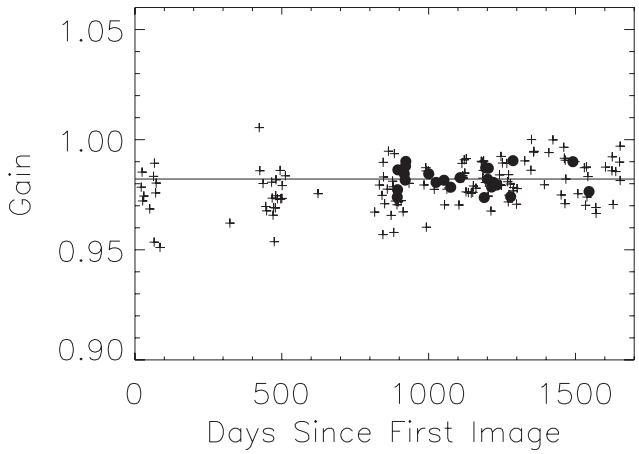

Fig. 19. The vicarious gains for band 4. The symbols used are the same as in Fig. 16.

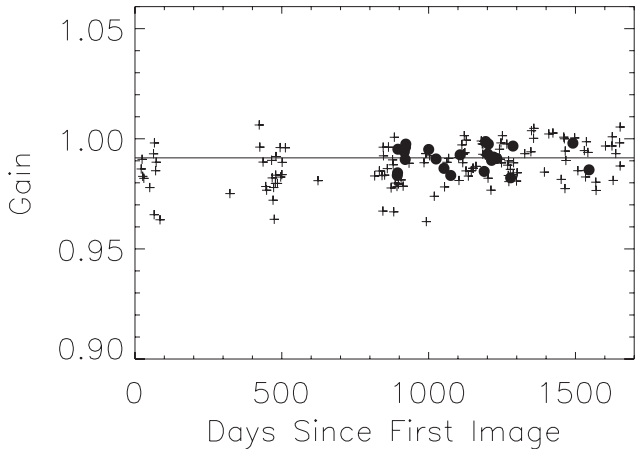

Fig. 20. The vicarious gains for band 5. The symbols used are the same as in Fig. 16.

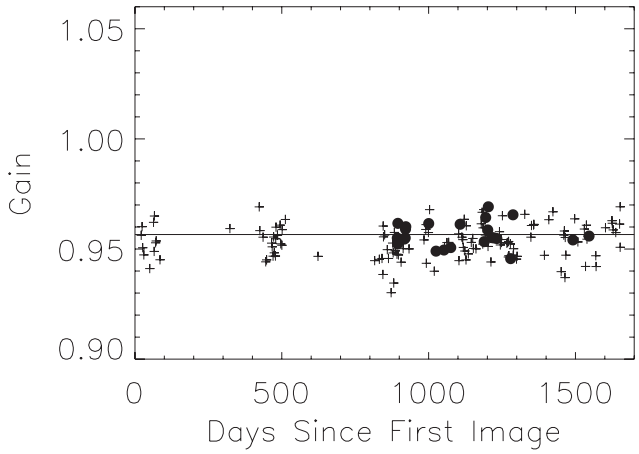

Fig. 21. The vicarious gains for band 6. The symbols used are the same as in Fig. 16.

Table 3. These vicarious gains were used for the fourth reprocessing.

Band	1	2	3	4	5	6	7	8
Gain	1.013007	0.996384	0.962951	0.982130	0.991338	0.956581	0.9380	1.0000

have been disabled or have been enabled with a transition (Chapt. 4 in this volume) at low chlorophyll concentrations. The vicarious gains were derived for the fourth reprocessing using the inverse calibration procedure.

3.5 VICARIOUS GAINS

Throughout the analyses performed in preparation for the fourth reprocessing, the vicarious calibration was updated as specific changes were implemented in the data processing methodology that would effect the derivation of the vicarious gain. Such changes included the MOBY stray light correction, the switch to the revised calibration table, the implementation of the ramp-in of the NIR correction algorithm at low chlorophyll levels, and the Fresnel transmittance correction at the air–sea interface.

The vicarious calibration data set used for the fourth reprocessing is composed of 23 SeaWiFS–MOBY matchups selected from an original pool of 163 potential matchups. Time series of the TOA gains for bands 1–6 are shown in Figs. 16–21. The 163 potential matchups in each band are shown by pluses and the 23 matchups used in computing the overall vicarious gains are shown by filled circles. The data quality screening applied to both the MOBY and SeaWiFS data has significantly reduced the scatter in the individual gains used to compute the overall vicarious gains. The vicarious gains used for the fourth reprocessing are shown in Table 3 and are plotted as horizontal lines in Figs. 16–21. It should be noted that the computed gains pass through the clusters of matchups that were excluded from the vicarious calibration.

As was discussed above, the gain for band 7 used in the fourth reprocessing was computed to optimize the retrieval of the aerosol optical properties, as described in Eplee et al. (2001).

As a validation of the vicarious gains, the L_{WN} values retrieved by SeaWiFS for the 23 matchups were compared with the water-leaving radiances measured by MOBY and were then normalized using the SeaWiFS-derived atmospheric correction parameters. The RMS differences between the SeaWiFS retrievals and the MOBY measurements are shown as percentages for bands 1–5 in Table 4. The radiances in band 6 are close to zero, so the RMS difference for band 6 is not a meaningful number. For bands 1–5, the differences increase with decreasing wavelength, which is to be expected if the major source of the uncertainties in the vicarious gains is the extrapolation of the atmospheric correction from the NIR to the visible.

Table 4. SeaWiFS and MOBY L_{WN} agree to better than 10%.

Band	1	2	3	4	5
RMS Differences [%]	9.74	7.86	4.46	3.69	2.41

3.6 SUMMARY

The CVT has improved the quality of both the MOBY and SeaWiFS data sets which are used in the vicarious calibration for the fourth reprocessing. The stray light correction of the MOBY data has improved the spectral shape of the vicarious gains. The stricter data quality screening imposed on both the MOBY and SeaWiFS data has reduced the uncertainty in the gains. In addition, an inverse calibration procedure was implemented to determine the vicarious gains. The result of these changes in the vicarious calibration methodology is a more robust vicarious calibration of SeaWiFS for the fourth reprocessing.

Chapter 4

Modifications to the SeaWiFS NIR Correction

Sean W. Bailey
Futuretech Corporation
Greenbelt, Maryland

Wayne D. Robinson and Bryan A. Franz
Science Applications International Corporation
Beltsville, Maryland

Abstract

This chapter describes several changes made to the NIR correction implemented during the fourth reprocessing of SeaWiFS data. The changes made were both to correct flaws in the actual implementation of the NIR correction and to improve the estimation of NIR reflectance. The changes include revised water absorption coefficients, the addition of a scaling factor to allow for the gradual introduction of the NIR correction as the derived chlorophyll concentration increases, improvements to the iteration control, and an alternative model for the backscatter estimate. The revised NIR correction reduces discontinuities in the aerosol model selection at the boundaries where the correction is introduced. It also reduces the attenuation effect that the original correction had on high chlorophyll concentrations.

4.1 INTRODUCTION

One of the primary assumptions used in the SeaWiFS atmospheric correction process is what is known as the *black pixel assumption*. This assumption states that the contribution to the total radiance by water-leaving radiance in the NIR region is negligible, and therefore, the TOA radiance in the NIR bands is solely due to atmospheric path radiance. For most conditions, this assumption is valid, however, in turbid or highly productive waters, this assumption breaks down. Various methods have been proposed to account for NIR water-leaving radiance for these situations. The SeaWiFS Project implemented an NIR correction (Siegel et al. 2000) with the third reprocessing in May 2000. Since then, refinements to the implementation of the NIR correction algorithm, as well as significant changes to the algorithm have been developed. While the basic concept for estimating NIR water-leaving radiance proposed by Siegel et al. (2000) is maintained, the methods have changed. This chapter describes these modifications.

4.2 BACKSCATTER MODEL

The NIR correction implemented with the third reprocessing used the particulate backscatter ($b_{\rm bp}$) estimate described in Loisel and Morel (1998) to estimate backscattering (b_b) at 555 nm and the spectral backscattering function described in Morel (1988) to extrapolate this value into the NIR. In practical application, the NIR correction is applied most often in highly productive waters ($>3\,{\rm mg\,m^{-3}}\,C_a$) and turbid or Case-2 waters. The Loisel and Morel model is explicitly Case-1, developed with a data set of chlorophyll values ranging from 0.01–4.53 $\rm mg\,m^{-3}$, with the majority of the data having values of less than 1.5 $\rm mg\,m^{-3}$. The Loisel and Morel model is not applicable to Case-2 waters. Gould et al. (1999) developed a spectral dependence model for the scattering coefficient in Case-1 and Case-2 waters. This model was implemented in place of the Morel (1988) model as being more appropriate to the practical application of the NIR correction in SeaWiFS.

A reflectance-based estimate of backscatter (Sydor and Arnone 1997) at a reference wavelength of 670 nm has been adopted in place of the chlorophyll-based estimate described in Loisel and Morel (1998). This reflectance-based estimate relies on the assumption that water absorption is dominate at wavelengths greater than 650 nm. This assumption allows for the estimation of $b_b(670)$ from $R_{\rm rs}(670)$ by (3):

$$b_b(670) \;=\; R_{\rm rs}(670)\frac{a_w(670)}{0.051}, \qquad (3)$$

where a_w is the absorption coefficient for water.

There can, however, be a measureable amount of particulate absorption (a_p) at 670 nm. Two additional absorp-

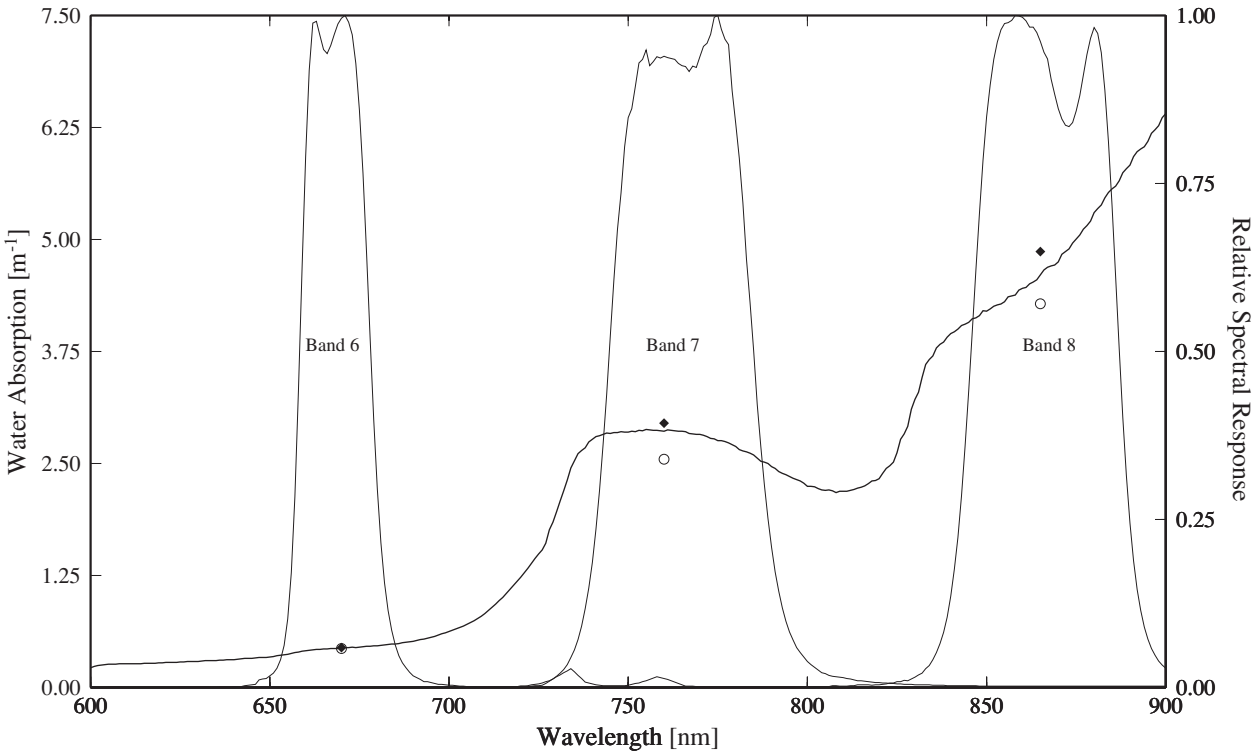

Fig. 22. Water absorption spectra with SeaWiFS spectral response overlayed. The open circles indicate values for water absorption cited in Siegel et al. (2000), and the solid diamonds indicate revised values.

tion terms have, therefore, been added, particulate absorption (Bricaud et al. 1998),

$$a_p(670) \;=\; 0.019890\, C_a^{0.818}, \tag{4}$$

and detrital–gelbstoff absorption ($a_{\rm dg}$) (Chapt. 9 in this volume),

$$a_{\rm dg}(670) \;=\; 0.15 \;-\; 0.19\,\frac{R_{\rm rs}(555) - R_{\rm rs}(670)}{R_{\rm rs}(555)}. \tag{5}$$

The total absorption ($a_{\rm tot}$) term becomes,

$$a_{\rm tot}(670) \;=\; a_w(670) \;+\; a_p(670) \;+\; a_{\rm dg}(670), \tag{6}$$

resulting in a new $b_b(670)$ equation,

$$b_b(670) \;=\; R_{\rm rs}(670)\frac{a_{\rm tot}(670)}{0.051}. \tag{7}$$

Because there are no reliable *in situ* measurements of NIR water-leaving radiance, validating the NIR correction is difficult. In order to evaluate whether or not the changes to the NIR correction algorithm constituted an improvement over the correction implemented with the third reprocessing, the Ångström exponent product was used as a proxy. The goal of the NIR correction is to account for water-leaving radiance in the NIR bands under conditions for which the black-pixel assumption is not valid, so that the retrieval of aerosol properties can be performed correctly. Because these aerosol properties should be independent of in-water constituents, it is assumed that the aerosol products (e.g., Ångström) should not be correlated with chlorophyll retrievals or water-leaving radiance (or reflectance). Visual inspection of LAC resolution imagery processed with the chlorophyll-based NIR correction showed patterns in the Ångström product that mirrored the chlorophyll product, with distinct boundaries at the transition regions of the image where the NIR correction was applied. These same scenes were processed with the reflectance-based NIR corrected; the Ångström product showed a correlation with the in-water constituents only under extremely turbid conditions.

4.3 ABSORPTION COEFFICIENTS

The NIR correction algorithm uses the absorption coefficient of water in its formulation. The values used with the Siegel et al. (2000) algorithm, implemented with the third reprocessing, were derived from published values [Hale and Query (1973) and Smith and Baker (1981)] for the nominal center wavelengths of SeaWiFS NIR bands. Given the strong absorption of water in the NIR and the 40 nm bandpasses for the SeaWiFS NIR bands (Fig. 22), these numbers are underestimated. A revised set of bandpass-averaged numbers were generated (Table 5), based on the newer published values for water absorption than those

cited in Siegel et al. (2000), Kou et al. (1993), and Pope and Fry (1997).

Table 5. Revised absorption coefficient for water based on full SeaWiFS bandpasses.

	Band 6 670 nm	*Band 7* 765 nm	*Band 8* 865 nm
a_w†	0.4346	2.5500	4.2860
Revised a_w	0.4458	2.9530	4.8680
Percent difference	2.5770	15.8039	13.5791

† Siegel et al. 2000.

4.4 SCALING FACTOR

A change was made in the NIR correction to introduce a scaling factor to the NIR radiances as a function of the amount of chlorophyll. The NIR radiances are modified by a factor that is zero for chlorophyll from 0–0.7 mg m^{-3}, 1.0 for chlorophyll of 1.3 mg m^{-3} and above, and linearly increasing from 0–1.0 in the 0.7–1.3 mg m^{-3} chlorophyll range. The change was made for several reasons.

Determining the NIR radiances is a computationally intensive iterative process that only makes a significant correction at chlorophyll values above 2 mg m^{-3} (Siegel et al. 2000). Below this value, the assumption of no NIR radiances is reasonable. Performing the iterations above chlorophyll concentrations of 0.7 mg m^{-3} increases the processing speed and still addresses regions where the non-zero NIR is important.

Another reason for not having the NIR correction applied at low chlorophyll concentrations is that the vicarious calibration process can be performed much more quickly if the iteration for the NIR does not have to be done. As the chlorophyll at the vicarious calibration site rarely gets higher than 0.1 mg m^{-3}, the threshold of 0.7 mg m^{-3} allows for the vicarious calibration to be performed without the NIR iteration. In addition, users of the chlorophyll data had concerns during the third reprocessing that the NIR algorithm was changing the low chlorophyll values. This occurred because the initial first guess NIR was computed for a chlorophyll value of 0.3 mg m^{-3}, which made a small, but noticable difference in the chlorophyll retrievals made with and without the NIR algorithm enabled. The current use of zero NIR removes this problem.

The scaling factor for the transition from no NIR at a chlorophyll concentration of 0.7 mg m^{-3}, to the full NIR at 1.3 mg m^{-3} linearly increases from 0–1.0 to remove the occurrence of any artifacts in the chlorophyll distribution that would be caused by the abrupt change of the NIR radiances at one chlorophyll value. The transition is instead distributed over a 0.6 mg m^{-3} range, where the NIR correction has a small effect on the chlorophyll. The transition starts well above the typical conditions used for vicarious calibration and well below where the effect of the NIR correction is significant.

4.5 ITERATION CONTROL

In order to improve the estimate of the NIR reflectance, the correction algorithm was implemented in an iterative manner. The original iteration control was quite simplistic. The algorithm would iterate until retrieved chlorophyll concentration changed by less than 20% from the previous iteration, for a maximum of 10 iterations. If the chlorophyll retrieval failed during the iteration process, the iteration was reinitialized once with a chlorophyll value of 5 mg m^{-3}. The iteration control was modified to improve the behavior. The following changes were implemented:

1. Dampening between iterations: The NIR reflectance returned is averaged with the previous iteration result to minimize the possibility of large fluctuations between iterations.
2. Iterations stop when the average NIR water-leaving reflectance changes by less than 2%, or $R_{\rm rs}(670) < 0.0$.
3. The initial C_a value is changed from 0.3 mg m^{-3}, to 0.0 mg m^{-3}. The initial $R_{\rm rs}(670)$ value is set to 0.0.
4. The iteration is reinitialized on any iteration where the chlorophyll retrieval fails, up to the maximum allowed iterations (currently 10), using:
   a) $C_a = i5.0$, where i is the number of iterations, and
   b) $R_{\rm rs}(670) = 5.0(0.00032 + 0.00021C_a)$.

4.6 DISCUSSION

Changes were made to the methods used by the SeaWiFS project to estimate water-leaving radiance in the NIR bands to allow for atmospherically correcting data where the black pixel assumption is not valid. These changes included a scaling factor, a revision of the iteration control for the algorithm, an update to the absorption coefficients for water used in the algorithm, and the switch to a reflectance-based estimate of backscatter with a new function to estimate NIR backscatter from a reference wavelength in the visible spectrum. These changes produce a marked improvement to the NIR correction as it is applied operationally to SeaWiFS data.

Chapter 5

Changes to the Atmospheric Correction Algorithm and Retrieval of Oceanic Optical Properties

Bryan A. Franz and Robert E. Eplee, Jr.
Science Applications International Corporation
Beltsville, Maryland

Sean W. Bailey
Futuretech Corporation
Greenbelt, Maryland

Menghua Wang
University of Maryland, Baltimore County
Baltimore, Maryland

Abstract

In preparation for the fourth SeaWiFS reprocessing, a series of algorithm changes were implemented to enhance the performance of the atmospheric correction process and to improve the quality and consistency of oceanic optical property retrievals. Included in these changes was the introduction of a filtering process to reduce the relative noise between the two NIR channels. In addition, several modifications were made to improve the handling of the SeaWiFS out-of-band response, and the normalization of water-leaving radiances was extended to account for Fresnel transmittance effects through the air–sea interface. These and other algorithm updates are described within this chapter.

5.1 INTRODUCTION

While the general approach to SeaWiFS atmospheric correction over oceans did not change for the fourth reprocessing, a number of refinements were implemented and evaluated. Several of these modifications were found to yield significant improvement in the quality and consistency of oceanic optical property retrievals; the changes were included in the final reprocessing software and are discussed in detail in this chapter:

a) A filtering scheme for reducing aerosol model selection noise,
b) A modification to improve algorithm performance in very clear atmospheres,
c) Updates to the corrections for out-of-band response,
d) An extension of the water-leaving radiance normalization to account for Fresnel transmittance through the air–sea interface, and
e) A fix for aerosol model ambiguity problems.

5.2 RELATIVE NOISE REDUCTION

The SeaWiFS atmospheric correction algorithm (Gordon and Wang 1994) relies on the single-scattering aerosol reflectance ratio (ϵ) between the two NIR bands at 765 and 865 nm to select the aerosol type. The atmospheric correction is, therefore, highly sensitive to any relative noise between these two NIR channels. A filtering technique was developed to reduce the relative noise in the NIR band ratio, which thereby reduces the small scale variability in aerosol model selection. The smoothing filter adjusts the radiance in the 765 nm channel to minimize local variability in the observed NIR aerosol ratio (i.e., the multiscattering equivalent of atmospheric ϵ, i.e., ϵ_{ms}), while leaving the 865 nm radiance (which governs aerosol concentration) unchanged. The effect of this smoothing is to reduce pixel-to-pixel variability in the retrieved aerosol type, which ultimately reduces atmospheric correction noise in the retrieved water-leaving radiances.

The effect of this filtering can easily be seen in level-2 images of ϵ, the Ångström coefficient, and, to a lesser extent, aerosol optical thickness at 865 nm. The value of this smoothing will diminish with increasing spatial and temporal averaging, and is more readily seen as reduced speckling in level-2 oceanic and atmospheric optical property retrievals. The smoothing was found to induce no bias-change in either the aerosol optical thickness or the water-leaving radiances. The smoothing algorithm follows:

1. Define NIR aerosol radiance at pixel i for wavelength λ as

$$L_a(\lambda,i) = \frac{1}{t_{\rm ox}(\lambda,i)}\left[\frac{L_t(\lambda,i) - tL_f(\lambda,i)}{t_{\rm oz}(\lambda,i)} - L_r(\lambda,i)\right]. \quad (8)$$

2. Given a scan-pixel window centered on pixel i, i.e., i_c, containing a total of n unmasked pixels, compute mean $L_a(\lambda)$ at i_c as

$$\langle L_a(\lambda,i_c)\rangle \;=\; \frac{1}{n}\sum L_a(\lambda,i), \quad (9)$$

for $i = 1, n$ and $\lambda = 765$ or 865 nm.

3. Compute the mean multiscattering ϵ value at pixel i_c as

$$\epsilon_{\rm ms} \;=\; \frac{\langle L_a(765,i_c)\rangle}{\langle L_a(865,i_c)\rangle}. \quad (10)$$

4. Then compute a new $L_a(765,i_c)$ which would yield the mean ϵ value when combined with the original $L_a(865,i_c)$ as

$$L'_a(765,i_c) \;=\; \epsilon_{\rm ms} L_a(865,i_c). \quad (11)$$

5. Reconstruct the TOA radiance at 765 nm as

$$\begin{aligned} L_t(765,i_c) \;&= t_{\rm oz}(765,i_c)\Big[L'_a(765,i_c)t_{\rm ox}(765,i_c) \\ &\quad + L_r(765,i_c)\Big] \;+\; tL_f(765,i_c), \end{aligned} \quad (12)$$

where

- $L_t(\lambda,i)$ is the observed TOA radiance for wavelength λ at pixel i;
- $tL_f(\lambda,i)$ is the white cap radiance, transmitted to the TOA;
- $L_r(\lambda,i)$ is the Rayleigh path radiance;
- $L_a(\lambda,i)$ and $L'_a(\lambda,i)$ are the aerosol path radiance (including Rayleigh aerosol interaction) and the new computed aerosol path radiance, respectively;
- $t_{\rm ox}(\lambda,i)$ is the oxygen transmittance;
- $t_{\rm oz}(\lambda,i)$ is the ozone transmittance; and
- Mean values are within angle brackets, $\langle\ \rangle$.

Using the filter-adjusted TOA radiance at 765 nm, the SeaWiFS atmospheric correction algorithm is then operated in the standard manner.

It is desirable to keep the filter window size as small as possible, to limit the reduction of real changes in aerosol type. The window size, however, needs to be large enough to allow sufficient sample size for the averaging to be effective. In addition to varying the size, it is also possible to change the shape. This can be achieved by introducing the concept of a filter window kernel, which indicates which pixels within the window will be considered in computing the filtered value. Consider these two examples of a 5×5 filtering window, where the value of 1 indicates that the pixel at that location will contribute.

Square 5x5	Diamond 5x5
1 1 1 1 1	0 0 1 0 0
1 1 1 1 1	0 1 1 1 0
1 1 1 1 1	1 1 1 1 1
1 1 1 1 1	0 1 1 1 0
1 1 1 1 1	0 0 1 0 0

For the same window size, the diamond filter kernel reduces the number of contributing samples by approximately 50% over the square kernel, and the radius of influence is never greater than two pixels. While this reduces the number of samples contributing to the mean, the diamond shape is better designed to minimize line-by-line digitization problems such as those associated with SeaWiFS mirror side differences. This is because the diamond kernel gives nearly equal weight to the odd and even lines, while the square kernel yields a 3-to-2 over weighting of opposing lines.

For SeaWiFS LAC resolution data, it was found that the NIR relative noise reduction filter with a 5×5 diamond kernel gave the best compromise between noise reduction and aerosol smoothing. Figure 23 shows a LAC subscene of L_{WN} values at 443 nm, before and after smoothing.

Unfortunately, it was found that the filtering approach did not always reduce noise in SeaWiFS GAC resolution scenes. The problem appears to be that the GAC data set, being subsampled at the sensor, does not contain a complete record of the bright sources observed by the instrument. This is a fundamental limitation of SeaWiFS, as it is simply not possible to identify and correct for all stray light contamination in the GAC data set. Any algorithm that combines neighboring pixels will, therefore, increase the probability of stray light contamination in a given pixel. The problem is most significant in the vicinity of scattered clouds. Considering this limitation, and the fact that GAC data are primarily used for generating spatial and temporal composites (where noise will be significantly reduced through averaging), it was decided that the NIR relative noise reduction filter would not be applied to the GAC products in this reprocessing.

5.3 CLEAR CONDITIONS

Under very clear atmospheric conditions, the Rayleigh-subtracted radiance in the NIR approaches zero. When other uncertainties are included, the retrieved aerosol path radiances in the NIR may even go slightly negative. The aerosol model selection, therefore, becomes highly uncertain in clear atmospheres. As a result, the SeaWiFS atmospheric correction algorithm often fails to obtain ocean color retrievals in the best of atmospheric conditions. A simple solution to this problem is to fix the aerosol type when the aerosol path radiance in one or both of the NIR bands approaches zero, and limit the aerosol radiance at 865 nm to be greater than, or equal to, zero. With these two changes, it is possible for the atmospheric correction algorithm to procede when the retrieved aerosol concentration is effectively zero.

The aerosol type to which low aerosol pixels will be fixed is a simple white aerosol, i.e., $\rho_a(\lambda) = \rho_a(865)$, where $\rho_a(\lambda)$ is aerosol path reflectance at wavelength λ. The threshold below which the aerosol model will be fixed has been set at a very conservative value of ρ_a (NIR) = 0.0001.

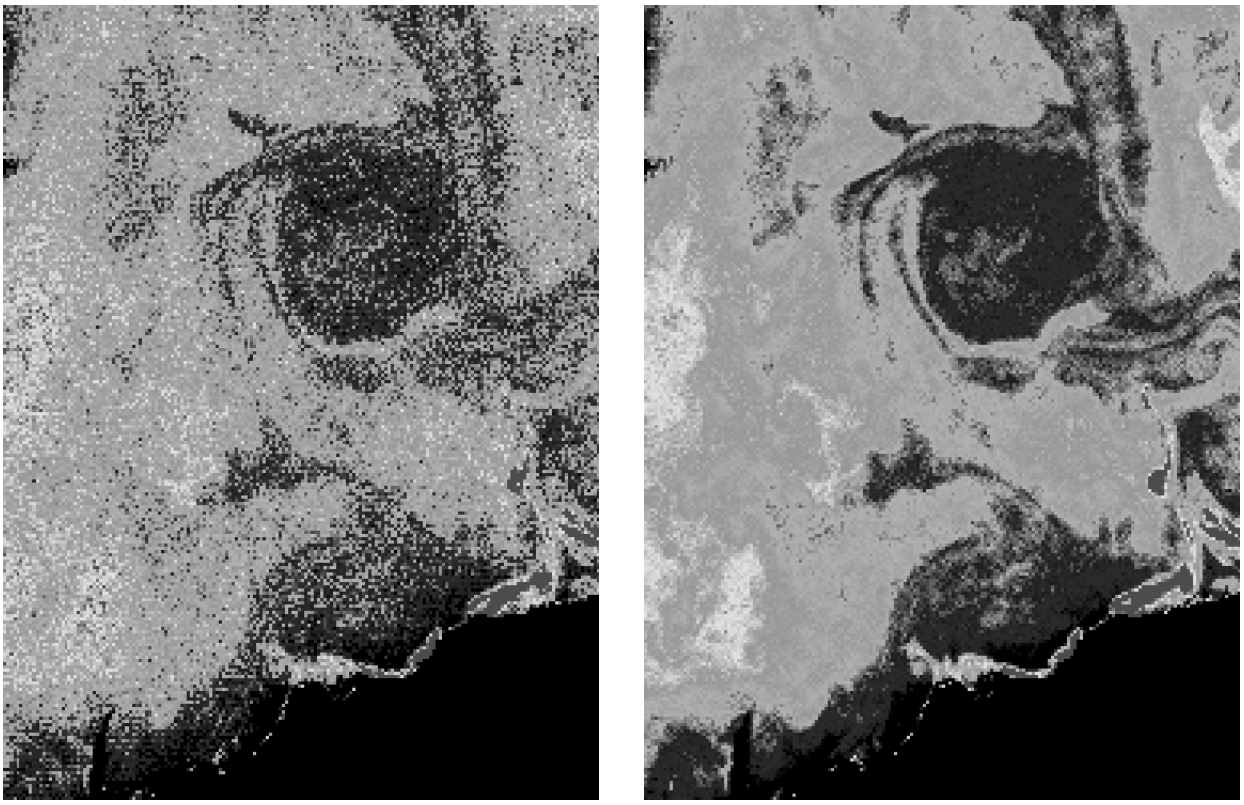

Fig. 23. Sample LAC image of normalized water-leaving radiance at 443 nm, before and after application of the NIR relative noise reduction filter: **a)** the scene without filtering, and **b)** the same scene with filtering applied.

For the 765 and 865 nm channels, this reflectance value corresponds to slightly greater than 1 digital count. Raising this value will force a larger percentage of the pixels to assume white aerosols, thus bypassing the aerosol model selection process of Gordon and Wang (1994).

In conjunction with the above enhancement, the occurrence of $\left[(L_t - tL_f)/t_{\rm oz} - L_r\right] < 0$ in one or more of bands 2–8 will no longer be considered an atmospheric correction failure condition.

5.4 OUT-OF-BAND CORRECTION

The SeaWiFS spectral bands cover the range from 380–1,150 nm, with nominal band centers at 412, 443, 490, 510, 555, 670, 765, and 865 nm. The spectral bandwidth, which is defined as the full width at half the maximum response, is 20 nm for the first six bands and 40 nm for the two NIR bands. The SeaWiFS bands, however, are known to exhibit significant response well beyond the quoted spectral range of the bandpasses. Throughout the SeaWiFS atmospheric correction process, adjustments are made to account for this out-of-band response (Gordon 1995). In the third SeaWiFS reprocessing, additional corrections were added to adjust the retrieved L_{WN} values to correspond to the nominal band center wavelengths (Wang et al. 2001). For the fourth SeaWiFS reprocessing, several modifications were made to the out-of-band corrections for the water-leaving radiances and derived reflectances. These changes are discussed in the sections that follow.

5.4.1 Remote Sensing Reflectance

The solar irradiance (F_0) values used in the SeaWiFS atmospheric correction processing are band-averaged quantities. This means that the solar spectrum has been convolved with the relative spectral response (RSR) function, where the RSR may include significant out-of-band response. In the third SeaWiFS reprocessing, an algorithm was introduced to correct the L_{WN} retrievals from band-averaged quantities to a nominal wavelength. Unfortunately, the out-of-band corrected L_{WN} vlaues were still normalized by the band-averaged F_0 when computing $R_{\rm rs}$. The $R_{\rm rs}$ ratios between the visible bands were then used as input to the OC4 chlorophyll algorithm (O'Reilly et al. 2000), so the resulting chlorophyll retrievals may have been slightly biased. In the fourth reprocessing, the nominal band L_{WN} values were normalized by nominal band F_0 values when computing $R_{\rm rs}$.

5.4.2 Water-Leaving Radiance

The L_{WN} retrievals are computed as band-averaged values, with an out-of-band correction applied prior to use

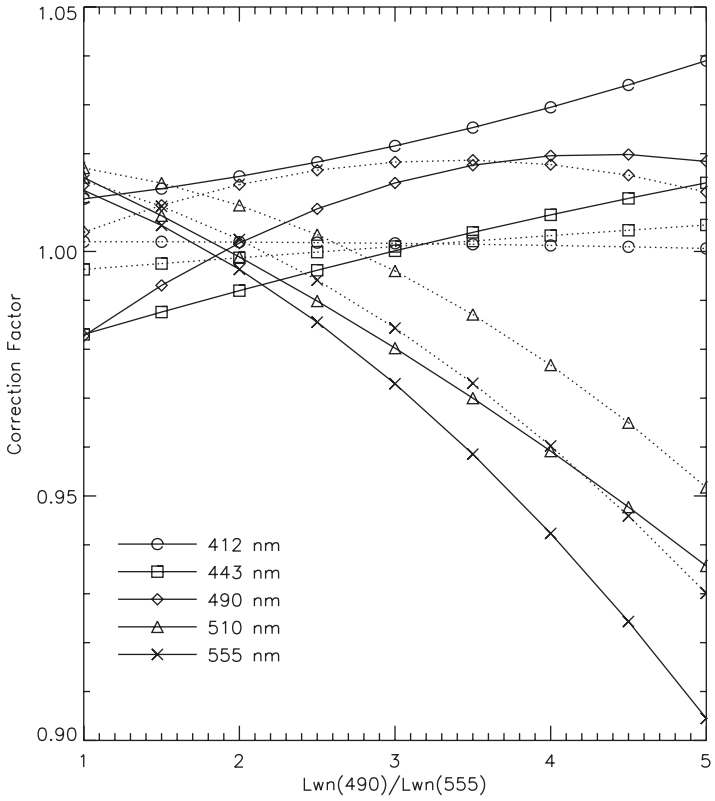

Fig. 24. Comparison of Morel and Maritorena (2001) bio-optical model with Gordon et al. 1988 model.

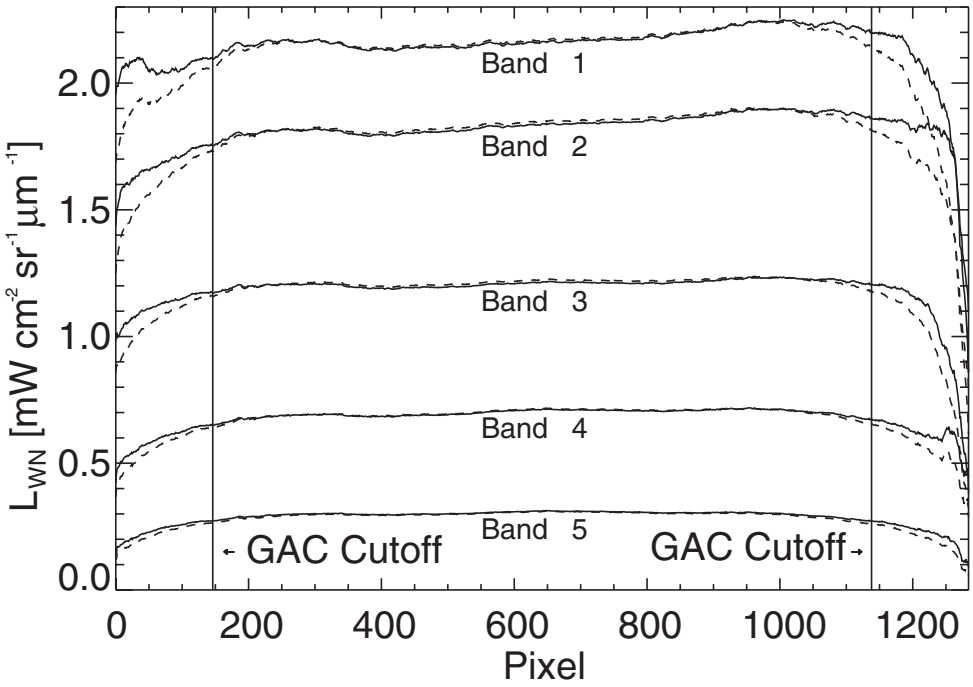

Fig. 25. Mean along-scan normalized water-leaving radiance retrievals, before and after application of the Fresnel transmittance correction. The solid line is with correction.

in downstream computations such as chlorophyll retrieval. The correction applied in the third SeaWiFS reprocessing was computed from the $L_{WN}(\lambda_{3/5})$ ratio, and was based on a chlorophyll-dominated L_{WN} spectrum which uses the Gordon et al. (1988) model. A revised set of correction factors were generated for this reprocessing using the recently published clear-water reflectance model of Morel and Maritorena (2001). Figure 24 shows the comparison between the correction factors from Gordon et al. (1988) and Morel and Maritorena (2001), with the Morel and Maritorena (2001) model results indicated by the solid lines.

This change to the out-of-band correction factors results in a lowering of chlorophyll values in waters with a $\lambda_{3/5}$ L_{WN} ratio of greater than approximately 2. For lower ratios, chlorophyll increases slightly. Differencing tests on global binned products indicate that the revised out-of-band correction results in a net decrease of 2.5–4.0% in global averaged chlorophyll retrievals.

5.5 FRESNEL TRANSMITTANCE

The normalization of water-leaving radiance was modified to include a correction for Fresnel transmittance through the water–atmosphere interface. The Gordon and Wang (1994) atmospheric correction algorithm assumes that the water-leaving radiance just beneath the ocean surface, $L_{WN}(0^-)$, is uniform. For a flat ocean surface, the normalized water-leaving radiance just above the surface, $L_{WN}(0^+)$, can be related to the value just beneath the surface as

$$L_{WN}(\theta) \;=\; \frac{t_f(\theta)}{n_w^2} L_{WN}(0^-), \tag{13}$$

where θ, $t_f(\theta)$, and n_w are the sensor zenith angle, the Fresnel transmittance of the air–sea interface, and the refractive index of the water, respectively. It is assumed in the above equation that the normalized water-leaving radiance just beneath the surface, $L_{WN}(0^-)$, is uniform (independent of the sensor zenith angle θ). Without correction, therefore, the SeaWiFS-derived normalized water-leaving radiance, L_{WN}, depends on the sensor zenith angle according to $t_f(\theta)$. In fact, the Fresnel transmittance effect is part of the ocean bidirectional reflectance factors (f/Q correction) discussed by Morel and Mueller (2002). A simple correction was implemented to remove the air–sea transmittance effect on the SeaWiFS-derived normalized water-leaving radiances. The corrected values, L'_{WN}, are computed as

$$L'_{WN} \;=\; \frac{t_f(\theta=0)}{t_f(\theta)} L_{WN}(0^+), \tag{14}$$

where L'_{WN} and L_{WN} are normalized water-leaving radiances with and without surface transmittance correction, respectively. The L'_{WN} values (for all six visible bands) are now the SeaWiFS-derived normalized water-leaving radiances. Note that the correction does not affect the SeaWiFS chlorophyll a concentration values because the transmittance effects are cancelled in the band ratio.

The general effect of this change is to increase the normalized water-leaving radiance in all bands, with the largest increase occurring at the highest view zenith angle, reaching approximately 3% at the GAC limit of 56°. Figure 25 shows the effect of this Fresnel correction across the full SeaWiFS scan. The scan trends were derived by simple averaging of water-leaving radiance retrievals within each scan pixel over a one year period in the relatively homogeneous waters near Hawaii. The solid line is the corrected data, and the dashed line is the uncorrected data. Note that the *roll off* in radiance near the edge of the GAC swath and beyond is reduced.

5.6 AEROSOL MODEL AMBIGUITY

Under certain geometric conditions, the T99 (tropospheric, 99% relative humidity) and C50 (coastal, 50% relative humidity) aerosol models cross over in ϵ space. These discontinuities appear along lines of constant scattering angle, and they are sometimes visible in images of water-leaving radiance and even chlorophyll. Application of the aforementioned NIR relative noise reduction filtering makes these effects even more apparent, as the aerosol model selection noise is reduced across the scattering angle isolines. A fix was developed which identifies these model cross-over conditions and revises the model selection result accordingly. The details of these effects are discussed in Wang (2003). This is a relatively rare problem which will not significantly effect global results.

Chapter 6

Masks and Flags Updates

Wayne D. Robinson, Bryan A. Franz, and Frederick S. Patt
Science Applications International Corporation
Beltsville, Maryland

Sean W. Bailey
Futuretech Corporation
Greenbelt, Maryland

P. Jeremy Werdell
Science Systems and Applications, Incorporated
Lanham, Maryland

Abstract

The flags and masks used for the SeaWiFS level-2 and level-3 processing were updated for the recent fourth reprocessing. This chapter discusses the changes and why they were made. In many cases, underlying algorithms were changed. Some flags changed their states to either flagging (noting a condition), or masking (denoting data excluded from the product) to allow more data to be kept or to improve its quality. New flags were either introduced as a part of new algorithms or to denote the status of the data more clearly. The flag and mask changes significantly contributed to the improvement in the data quality and increased the amount of data retrieved.

6.1 INTRODUCTION

As part of the algorithm improvements for the fourth reprocessing, several improvements were made in the flagging and masking done in the level-2 and level-3 SeaWiFS data processing. Table 6 shows a list of the current flags used in the fourth reprocessing, their status in operational processing as a flag (to note a condition) or a mask (to note that the data are excluded from the product because of this condition), a brief description of the flag, and a general indication of how this flag changed from the third to the fourth reprocessing. Three general classes of change are noted.

For many flags, the underlying algorithm that generates the flag was changed. In all these cases, the new algorithm is an improvement over the old algorithm in that it characterizes the flag condition better, and in some cases, is able to allow for a greater number of good retrievals to be made. In Table 6, this is denoted as a change.

Some flags had their status as a mask or a flag changed for the fourth reprocessing. Many times, this change was a direct result of the algorithm changes referred to above. Other changes were prompted by increased experience with the operation of the flag, which revealed the data quality or amount of retrieved data would be increased with the new masking. Table 6 notes cases in which data previously masked are now flagged, or vice versa. The changes in masking and flagging are noted for the level-2 and the level-3 product. For the level-3 product, there is no actual flag for the data. In the case where the change in flag status is denoted as *flagged*, it really means that the data which were previously excluded from the level-3 product are now included as a part of the product.

Finally, four new flag conditions were added to the list of flags. These denote either new general conditions, or are part of new algorithms, or are used to more clearly separate conditions that occur during the level-2 processing. In Table 6, they are denoted as new flags.

The following sections describe the flag and mask changes in more detail. Section 6.2 describes an analysis to determine the effect of individual level-3 masks on the number of retrievals. Section 6.3 describes the changes in the flagging and masking for the level-2 product, Sect. 6.4 looks at the changes in the masking for the level-3 product, and Sect. 6.5 summarizes the changes.

6.2 FLAG EFFECT ANALYSIS

Most of the flag and mask changes came naturally from the increased understanding of the SeaWiFS data. For

Table 6. Flags for the fourth reprocessing. The *Mask In* columns indicate that no geophysical data is created in the level-2 (L2) or level-3 (L3) data set if the flag conditions marked *Y* exist for that observation. The changes from the third reprocessing fall under one or more of the following categories: a) New (a new flag for the fourth reprocessing); b) Change (a direct change in the algorithm or threshold was made); and c) *Mask in L2* or *Mask in L3* indicates that in the fourth reprocessing, data are now excluded from the level-2 or level-3 product and *Flag in L2* or *Flag in L3* indicates that data which were previously exluded from the product are now included, (e.g., the `HIGLINT` flag is no longer a mask in L2 or L3, so the change reads: "Flag in L2 and L3").

No.	*Flag Name*	*Mask In* L2	*Mask In* L3	*Description*	*Change From Third Reprocessing*
1	`ATMFAIL`	Y	Y	Atmospheric algorithm failure	—
2	`LAND`	Y	Y	Land	—
3	`BADANC`			Missing ancillary data	—
4	`HIGLINT`			Sun glint contamination	Flag in L2 and L3
5	`HILT`	Y	Y	Total radiance above the knee	Change
6	`HISATZEN`		Y	Satellite zenith angle above the limit	Change
7	`COASTZ`			Shallow water	Change
8	`NEGLW`			Negative water-leaving radiance in bands 7 and 8	—
9	`STRAYLIGHT`	Y	Y	Stray light contamination	Change, mask in L2
10	`CLDICE`	Y	Y	Clouds or ice	Change
11	`COCCOLITH`		Y	Coccolithophore bloom	—
12	`TURBIDW`			Turbid, Case-2 water	Change
13	`HISOLZEN`		Y	Solar zenith angle above the limit	—
14	`HITAU`			High aerosol concentration	—
15	`LOWLW`		Y	Low water-leaving radiance at 555 nm	—
16	`CHLFAIL`	†	Y	Chlorophyll not calculable	Change
17	`NAVWARN`		Y	Questionable navigation (tilt change)	—
18	`ABSAER`		Y	Absorbing aerosol index above the threshold	Change
19	`TRICHO`			*Trichodesmium* bloom condition	—
20	`MAXAERITER`		Y	Maximum number of iterations in the NIR algorithm	—
21	`MODGLINT`			Glint corrected measurement	—
22	`CHLWARN`		Y	Chlorophyll is out of range	Mask in L3
23	`ATMWARN`		Y	The ϵ value is outside of reasonable range or L_W at 490, 510, or 555 nm is less than zero	—
24	`DARKPIXEL`			Rayleigh corrected radiance is less than zero for any band	—
25	`SEAICE`			Sea ice present based on climatology	New
26	`NAVFAIL`	Y	Y	Navigation of the line is bad	New
27	`FILTER`		Y	Insufficient surrounding pixels for aerosol model filter‡	New
28–31				Spare for future use	N/A
32	`OCEAN`			Ocean data	New

† The chlorophyll value is not computed, but *first guess* L_{WN} values are computed.
‡ The filter algorithm is only applied to LAC and HRPT data.

the fourth reprocessing, another goal was to increase the number of retrievals without degrading the data quality by making the masking criteria less strict (known as *relaxing the criteria*). For flags that have a large role in reducing the number of retrievals, the algorithms could then be re-examined to see if the flagging could be relaxed to increase the number of retrievals.

Early in the preparation for the fourth reprocessing, a test was performed to determine which flags, if relaxed, would result in a large increase in the number of retrievals. A level-3 8-day bin file was made for the period starting 2 June 2001 with minimal masking criteria (`ATMFAIL`, `LAND`, `FILTER`, `CLDICE`, `CHLFAIL`, `NAVFAIL`) enabled to form a control case for testing the effect of other flags in masking data. The 11 flags usually used as masks in the level-3 processing were individually turned on and the effect of each flag is shown in Table 7. The effect of the flags are listed in order from the largest number of bins (Earth area coverage) removed to the smallest.

The stray light flag has the largest effect, decreasing coverage by 17% and the total number of retrievals by almost 33%. The geographic distribution of the bins lost to

Table 7. Effect of the level-3 binning flags in removing data. A baseline 8-day timebin level-3 file was produced using the third reprocessing and a minimum amount of level-3 masks (ATMFAIL, LAND, FILTER, CLDICE, CHLFAIL, NAVFAIL). The binning was repeated with one extra flag used as a mask to determine the effect of that flag in decreasing the bins (coverage) and samples relative to the baseline. The effects are listed in decreasing order of bins lost.

Flag Name	Decrease in *Bins* [%]	*Decrease in Samples* [%]	*Description*
STRAYLIGHT	17.26	32.13	Stray light contamination
TURBIDW	3.71	7.93	Turbid, Case-2 water
LOWLW	3.39	8.32	Low water-leaving radiance at 555 nm
HISOLZEN	1.08	0.48	Solar zenith angle above the limit
ATMWARN	1.04	1.43	The ϵ value unreasonable, L_W at 490–555 nm < 0
HISATZEN	0.45	1.64	Satellite zenith angle above the limit
HILT	0.25	0.35	Total radiance above the knee
ABSAER	0.18	0.51	Absorbing aerosol index above threshold
COCCOLITH	0.12	0.39	Coccolithophore bloom
MAXAERITER	0.08	0.28	Maximum iterations in NIR algorithm
NAVWARN	0.014	0.028	Questionable navigation (tilt change)

the stray light flag is relatively uniform over the oceans and is caused mainly by cloud edges. Aggregation over longer time periods reduces the lost coverage because of changing cloud distributions. The degree to which coverage is lost because of the stray light flag prompted the project to re-examine the stray light algorithm and flag to see if the loss of coverage could be reduced. The results of this work are presented in Sect. 6.3.5.

The analysis also revealed that the high satellite zenith angle flag was being set for some of the SeaWiFS GAC data. It was previously assumed that the 56° satellite zenith threshold would only flag LAC data, but analysis showed that it was happening at the very edges of the GAC scans. This prompted the examination of the high satellite zenith angle flag (Sect. 6.3.3). Other flags on the list were affected by the fourth reprocessing changes, but only the stray light and high satellite zenith angle flags were re-examined as a direct outcome of these tests.

6.3 LEVEL-2 CHANGES

The flag algorithms are all performed in the level-2 processing, so a majority of the changes are discussed in this section. The effect of these changes on the data is also presented. Changes in the use of flags for accepting data for level-3 binning are discussed in Sect. 6.4.

6.3.1 Glint

In the third reprocessing, the sun glint flag was used as a mask in the level-2 processing. The flag was activated when the estimated glint reflectance exceeded 0.005. Wang and Bailey (2001) showed that glint radiance could be effectively removed from the data by using the glint correction up to the point where the detectors saturate. Because other masks are active at this point, the glint flag no longer needs to be a mask.

In the fourth reprocessing, the HIGLINT flag is changed from a mask to a flag in the level-2 processing to allow more good data to be retrieved. The change to the glint mask left the global parameter means unchanged. The number of retrievals increased about 1% while the coverage increased by 0.2% for the monthly binned data and 0.9% for the daily binned data. The recovered pixels are in areas where the sun glint is high, i.e., around the subsolar point.

6.3.2 High Total Radiance Flags

For the third reprocessing, the high total radiance (HILT) flag was set for a pixel if the digital count value was above the knee in any of the eight SeaWiFS bands. This was done because radiances taken above the knee have substantially lower radiometric precision than those taken below the knee (McClain et al. 1995) and were not believed to have sufficient precision for accurate chlorophyll and water-leaving radiance retrieval. The flag has been used as a mask in the level-2 processing.

It was determined that although the higher precision is required for the NIR bands 7 and 8 at 765 and 865 nm to accurately characterize the aerosols, it is not required for the other bands. For the fourth reprocessing, the HILT flag is defined so that it only applies to the radiances in bands 7 and 8.

This change yields substantially more good retrievals in some coastal areas. Over the globe, the estimated increase in number of retrievals is only 0.06%. When binned over a month, the coverage is increased by 0.02%. The new retrievals are in regions of high chlorophyll, which increases the global chlorophyll mean and $L_{WN}(555)$, but reduces the $L_{WN}(412)$.

6.3.3 High Satellite Zenith Angle Flag

The satellite zenith threshold was extended from 56° (used in the third reprocessing) to 60°. This allows processing to be performed for pixels on the edge of the GAC swath which were being excluded because of the high satellite zenith angle. The satellite zenith angle is affected by the spacecraft roll, which caused pixels on the edge of the GAC scene to have a satellite zenith angle slight larger than the 56° limit. The increase in number of retrievals is about 1.5% and is distributed evenly over the globe.

6.3.4 Shallow Water Flag

The shallow water mask used for the third reprocessing was based on the Earth Topography 5 min of arc grid—ETOPO5 bathemetry data—from the National Geophysical Data Center (Sloss 1988). The mask for depths shallower than 30 m had a minimum resolution of about 9 km, which was noticable at the GAC resolution of 4 km and very noticable at the LAC and HRPT resolutions of 1 km.

The shallow water mask used for fourth reprocessing is based on the Earth Topography 2 min of arc grid—ETOPO2 bathemetry (Sloss 2001)—which has a resolution of approximately 4 km. The improved resolution of the mask results in a smoother boundary between shallow and deep water. The 15 MB size of the new shallow water mask file is slightly greater than the previous file size of 13 MB and should not pose a storage space problem.

6.3.5 Stray Light Flag

Section 6.2 showed that the effect of the stray light flag in reducing the number of retrievals was the greatest of all the additional flags used in the level-3 processing. If some relaxation of the masking criteria was possible, the increase in retrievals would be the greatest.

The stray light algorithm used through the third reprocessing was developed using laboratory measurements of a bright target (Barnes et al. 1995). The correction factors (for pixels that could be corrected) and masking recommendations (for pixels that could not be corrected) were incorporated into the stray light algorithm (Yeh et al. 1997). In the initial development of the corrections (Barnes et al. 1995), it was stated that it may be possible to relax the GAC masking so that two more pixels adjacent to a bright target could be corrected instead of flagged. Corrections for these pixels were also provided. The correcting of those extra pixels instead of masking results in a significant gain in retrievals.

This change in the stray light algorithm and masking was tested on a level-3 data set and on several level-2 data sets in open and coastal waters. It was found that the change to the stray light algorithm increased the number of retrievals by about 17% and did not change the global means of retrieved parameters. It was also found that the new set of corrected pixels had chlorophyll and normalized water-leaving radiance values very similar to neighboring pixels in the scene, even though the uncorrected total radiances showed significant increases from neighboring pixels to the new pixels.

The modified stray light algorithm is incorporated into the fourth reprocessing. In addition, the stray light flag is now used as a mask (instead of as a flag) for the level-2 data sets. The exclusion of pixels that are highly contaminated by, and uncorrected for, stray light in the level-2 data results in more consistent data quality. The stray light algorithm is unchanged for both LAC and HRPT data.

As a final note, the correction for stray light was derived only under laboratory conditions. These conditions, however, may not be representative of what is encountered by the satellite on orbit. It would be useful if an on-orbit analysis could be performed on the stray light correction factors to determine if they could be improved. The analysis could be performed at known sharp radiance boundaries, such as the moon's limb in the lunar calibration data, or the boundary between the ocean and either land or ice features in HRPT data.

6.3.6 Cloud and Ice Flag

In September 2000, the SeaWiFS imaging duty cycle was increased to include additional data at higher latitudes. GAC data is now routinely collected at solar zenith angles as high as 83°. It was found that the standard SeaWiFS cloud detection algorithm was too restrictive at these extreme solar zenith angles. In fact, it was pointed out that the predicted Rayleigh path radiance alone is sufficient to trip the cloud flag when solar zenith angles exceed 75° (H. Fukushima, pers. comm.). A proposed solution to this problem was to base the cloud test on a Rayleigh subtracted radiance value, such as the combined surface and aerosol reflectance at 865 nm. A threshold on this quasi-surface reflectance field, $\rho_s(865)$, of 0.027 (2.7%) was found to yield very similar results to the third reprocessing algorithm at moderate solar and viewing geometries, while still allowing high solar- and viewing-angle observations of apparently clear ocean pixels to pass through unmasked.

Figure 26 illustrates how the two quantities of albedo and quasi-surface reflectance, vary as a function of solar zenith angle. Each point in the plots is the average albedo or reflectance, computed from all the pixels in a typical GAC scan line. Only pixels for which there was a chlorophyll retrieval without stray light correction were included in the averages. The plots illustrate that the cloud albedo of relatively clear ocean observations (Fig. 26a) generally increases with solar zenith angle, with the rate of increase rising rapidly above 65°. In contrast, the surface reflectance distribution (Fig. 26b) remains relatively flat up to 75°, primarily because the change in the Rayleigh path radiance was accounted for. The high reflectance around 40° is due to a dust plume. The solid horizontal lines show

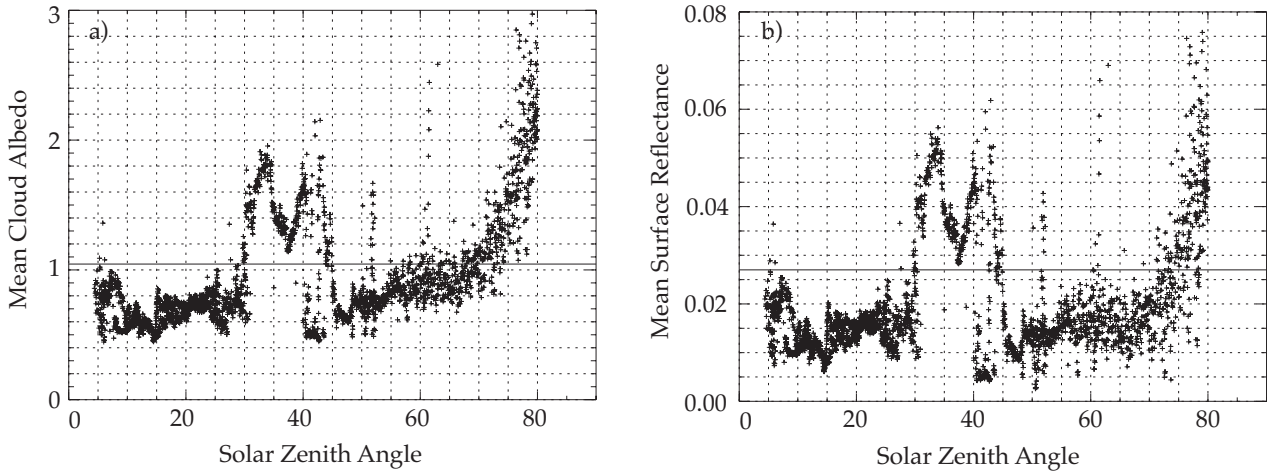

Fig. 26. a) Albedo at 865 nm as a function of the solar zenith angle for a typical SeaWiFS GAC orbit. The horizontal line indicates the cloud mask threshold for the third reprocessing. **b)** Quasi-surface reflectance at 865 nm for the same data as in panel **a)**. The horizontal line indicates the cloud mask threshold for the fourth reprocessing.

the threshold above which values are considered cloud contaminated. The threshold on $\rho_s(865)$ was chosen to give similar results to the current albedo threshold at moderate solar and viewing angles, but the surface reflectance test will allow more observations at higher solar and viewing zenith angles to pass through unmasked.

Application of the proposed cloud flag was found to increase overall coverage (in terms of number of filled 9 km bins) by 1–2%, with smaller gains seen in the monthly composite and larger gains seen in the daily composite. As expected, the increased coverage is seen primarily at high latitudes, where the solar zenith angle and the Rayleigh radiance are large. The average number of samples per bin also generally increased 1–2%. The most significant change to the derived products is a general increase in mean aerosol optical thickness, especially at higher solar angles. This is not suprising, as the cloud flag for the third reprocessing tends to mask even moderate aerosol loads when the solar and viewing angle is large, thus biasing the average toward lower aerosol optical thicknesses.

6.3.7 Turbid, Case-2 Water Flag

For the third reprocessing, the turbid water flag was set when the measured reflectance in band 5, at 555 nm, exceeded the estimated 555 nm reflectance derived from Morel's clear water model (Morel 1988). Because the Morel model requires pigment as input, an invalid chlorophyll retrieval would cause the turbid water flag to be erroneously set, or prevent the flag from being set under highly turbid conditions. This problem was remedied in the fourth reprocessing by basing the turbid water flag on a threshold of the remote sensing reflectance in band 6, at 670 nm [$R_{\rm rs}(670)$]. The water is flagged as turbid if $R_{\rm rs}(670)$ is greater than 0.0012, which is a value 25% larger than the expected value for pure water of 0.000954.

6.3.8 Chlorophyll Failure Flag

The SeaWiFS chlorophyll fields, although generally smooth, have sporadic isolated high values, or *speckles*. In past reprocessings, the Project has implemented checks that would limit these speckles, but some still remain.

For the fourth reprocessing, analysis of the data revealed some characteristic patterns in the water-leaving radiance spectra of pixels that have speckles. It was found that many of the high chlorophyll spikes were associated with spectra where the 510 or 490 nm bands went negative, while bracketing bands were positive. These conditions are considered nonphysical, and probably caused by proximity to bright sources that cannot be seen in the subsampled GAC data and which may cause band-dependent stray light or ringing effects. To avoid these pixels, new failure conditions were implemented in the operational chlorophyll algorithm. The following tests must be satisfied or the pixel will be given the chlorophyll failure (`CHLFAIL`) flag:

1) $R_{\rm rs}(510) > 0$;
2) $R_{\rm rs}(490) > 0$, or $R_{\rm rs}(443)R_{\rm rs}(490) > 0$; and
3) Both $R_{\rm rs}(443)$ and $R_{\rm rs}(490) > -0.001$.

The first two tests, taken together, enable the 443 nm and 490 nm bands to be less than zero, but require that the shorter wavelengths become negative before the longer wavelengths. This typically happens in the blue part of the spectrum when a) there is aerosol absorption, or b) if an aerosol model is selected which removes too much radiance. The third test limits the amount by which the reflectances can go negative. These additional tests flag a

significant number of the pixels that would otherwise add speckles to the data.

6.3.9 Absorbing Aerosol Flag

The absorbing aerosol flag algorithm has remained unchanged. Some of the thresholds used in the algorithm required modification to account for the radiance changes at 412 and 443 nm which came as a result of the calibration changes described in Chapt. 3.

6.3.10 Chlorophyll Warning Flag

Previously, the chlorophyll was stored in the level-2 data set as a scaled 2-byte integer which could represent any value from 0–64 $\mathrm{mg\,m^{-3}}$ with a precision of 0.001. For the fourth reprocessing, the chlorophyll parameter is stored as a 4-byte real value so that small values of chlorophyll can be stored with the same relative precision as larger values. This change also allows the storage of chlorophyll values greater than 64. The threshold for the chlorophyll warning flag, which was previously set at 64 $\mathrm{mg\,m^{-3}}$, was increased to 100 $\mathrm{mg\,m^{-3}}$ to account for the increased range available. The limit of 100 was chosen so that high values of chlorophyll could be recorded but unreasonably high values would be flagged.

6.3.11 Sea Ice Flag

The sea ice flag, `SEAICE`, is a new flag for the fourth reprocessing. It flags pixels that have a high probability of containing sea ice, based on a climatology of sea ice. The sea ice flag is used mainly in the creation of the PAR product.

6.3.12 Navigation Failure Flag

The navigation failure flag, `NAVFAIL`, is new for the fourth reprocessing. Previously, if a navigation failure condition was indicated in the level-1a data, the atmospheric algorithm failure flag was set in the level-2 data set. There was only one such condition—a failure in the navigation algorithm. In the fourth reprocessing, it became necessary to automatically and manually mark time ranges in the data where the navigation was unacceptable because of timing errors, as described in Chapt. 7. It was decided that for this added condition, and to more clearly denote the navigation failure condition, a separate flag would be assigned to failed navigation conditions. The navigation failure flag is used as a mask in the level-2 processing.

6.3.13 Aerosol Model Filter Flag

The aerosol model filter flag, `FILTER`, is new for the fourth reprocessing. This flag supports a new algorithm which reduces the noise in the NIR band ratio and thereby reduces the small scale variability in aerosol model selection. As a part of the filtering process, a minimum number of nonmasked neighboring pixels must be available for the filter to operate. If this minimum number is not present, the flag is set. The algorithm was not found to improve the GAC data, so it is not used in the fourth reprocessing for GAC data but it is suggested for LAC and HRPT processing.

6.3.14 Ocean Flag

The ocean flag, `OCEAN`, is also new for the fourth reprocessing. It indicates that the given pixel is a clear ocean pixel, without cloud contamination or land. This flag is used to give an estimate of how much useful ocean data is in a level-2 file.

6.4 LEVEL-3 CHANGES

The following changes were made in the use of flags and masks for the binning process which makes level-3 products.

1. The glint flag is no longer a masking condition in the fourth reprocessing. Section 6.3.1 notes that the glint flag does not need to be a mask because the glint correction is valid up to where the high total radiance or cloud and ice flags mask the pixel.
2. The chlorophyll warning flag is now a masking condition in the fourth reprocessing. This was done to keep erroneously high chlorophyll values out of the level-3 binned file. In the fourth reprocessing, chlorophyll values up to 100 $\mathrm{mg\,m^{-3}}$ are binned. More discussion about the chlorophyll flag can be found in Sect. 6.3.1.
3. The navigation failure flag is new for the fourth reprocessing. This flag is used to mask the level-2 product (Sect. 6.3.12), and is carried on as a mask for the level-3 binning.
4. The filter flag is set as a mask for the operational binning in the fourth reprocessing, but because the filtering is not enabled for GAC data, this mask has no effect on the operational level-3 product.

6.5 SUMMARY

A number of flag and mask changes were made as a part of the fourth SeaWiFS reprocessing. When combined with the calibration improvements and algorithm changes, this results in significantly better retrievals of water-leaving radiance, chlorophyll, and atmospheric products. A greater number of retrievals are also produced.

The flagging changes resulted, in part, in an overall increase of retrievals by 24% and an increase in global coverage of 24, 14, and 6% for daily, 8-day, and monthly time binned level-3 products, respectively. This was made possible by a relaxation in the stray light mask, the elimination of the glint flag as a mask, the improved treatment of the cloud and ice flag, a relaxation in the high satellite zenith flag, and a better treatment of the high total radiance flag.

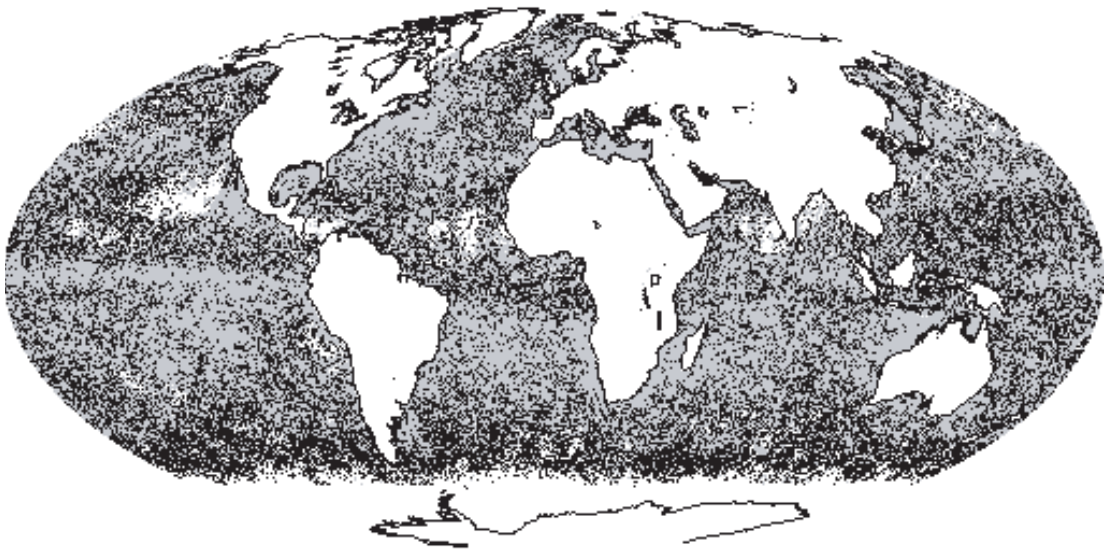

Fig. 27. Global distribution of the gained bins and samples for a monthly level-3 binned product (May 1999). The white indicates where no data exists, the grey indicates where the gain in samples in a bin was less than 30%, and the black indicates where new bin coverage occurred or where the number of samples in a bin increased by 30% or more. The continental outlines are drawn in black.

Figure 27 is an image showing the locations where new bins were gained and where the number of samples in a bin increased by 30% or more. Throughout the ocean areas, there have been relatively uniform increases in samples and bins. This is mainly the result of the change in the stray light mask permitting more data around cloud edges. These increases can also be attributed to the gain of samples at the ends of the scan lines that were previously beyond the old satellite zenith angle cutoff. In addition to the uniform increases, several areas show higher amounts of new retrievals. The Southern Ocean has substantial increases in samples and bins, mainly resulting from the new cloud flag, which no longer masks out data having moderately high aerosol radiances. The coastal regions also show increases in samples and bins, resulting from the reduction of the stray light mask near coastlines and the improved calibration. Other variations are a result of differing amounts of clouds in parts of the world.

Fields of normalized water-leaving radiance and chlorophyll were also improved. The chlorophyll failure flag was improved to reject more speckles in the chlorophyll.

Finally, the flags were improved and expanded to give better information about the conditions at any pixel. The shallow water flag is improved, using higher resolution data. The sea ice and ocean flags are new, and signal sea ice and unclouded ocean regions. The navigation failure flag separates the flagging for failed navigation conditions from different conditions.

Possible future improvements in the flags include a more thorough examination of the stray light algorithm to verify and possibly improve the corrections and masking conditions. The flag for low water-leaving radiance at 555 nm, which is a flag for cloud shadows, may be re-examined to see if a better cloud shadow algorithm can be implemented. Users of the data from the fourth reprocessing should acquaint themselves with the new flagging and masking changes so they can make the best use of the SeaWiFS data.

Chapter 7

Level-1a and Level-3 Processing Changes

Frederick S. Patt, Bryan A. Franz, and Wayne D. Robinson
Science Applications International Corporation
Beltsville, Maryland

Joel Gales
Futuretech Corporation
Greenbelt, Maryland

Abstract

Improvements were made in the level-1a and level-3 data processing for the fourth reprocessing. Two of these—handling of the spacecraft time tag anomalies, and modification of the level-3 space binning program—address specific problems in the data and processing logic, which excluded otherwise valid data from processing. The third improvement, an update to the navigation algorithms, improves the overall data quality by reducing the maximum navigation errors. The net effect of these changes is an increase both in coverage and quality of the SeaWiFS data products.

7.1 INTRODUCTION

This chapter describes changes that were made in the level-1a and level-3 data processing software as part of the fourth reprocessing. These changes were implemented independently of the level-2 algorithm updates which are described in the previous chapters. They represent either solutions to known problems in the previous versions of the processing software, or results of ongoing analysis of data quality.

The first of these changes is a method for handling anomalies, or *glitches*, in the spacecraft time tag during level-1a processing. These glitches have resulted in significant navigation errors, which previously could only be handled by excluding entire scenes from further processing. As a result, significant amounts of valid data were also excluded to avoid including the misnavigated periods. The new scheme both corrects simple time glitches and allows specific, uncorrected periods to be flagged within scenes, minimizing the loss of data.

As another part of the level-1a processing, improvements were made to the navigation algorithms to reduce the seasonal variations in accuracy. This update was actually made to the operational software in April 2001, but the fourth reprocessing was the first opportunity to apply it to the entire mission. In addition, a problem was identified and corrected in the initial level-3 processing (space binning) logic, which excluded some level-2 files from binning. Each of these changes is described in the following sections.

7.2 TIME TAG GLITCH HANDLING

The data stream produced by the OrbView-2 spacecraft contains a time tag for each level-0 data record, or minor frame. (A level-0 minor frame contains either one LAC scan line or five GAC scan lines, along with associated spacecraft and instrument telemetry.) In addition, the telemetry data contain time tags for various spacecraft subsystems. The spacecraft minor frame time tag is used during level-0-to-1A processing to compute the scan line time, which in turn is used in the determination of the spacecraft navigation fields (orbit position and attitude angles).

Various types of time tag glitches have been observed during the mission. The most serious are those that involve the minor frame time tag. A 1 s error in this time tag results in a pixel location error of 6.75 km, or 6 LAC pixels. Glitches that only affect other time tags (e.g., for telemetry fields) have little or no effect, and are largely handled in the processing software by data quality checks. Note that the glitches discussed here originate on the spacecraft, and affect all data types—GAC, LAC, and HRPT—when they occur. Time tag glitches may also be caused by data transmission errors, but these glitches are source dependent (specific ground station, and recorded versus direct broadcast) and are handled by data quality checks.

The types of minor frame time tag glitches are discussed in more detail below, followed by a description of the procedure implemented for handling the time glitches.

7.2.1 Minor Frame Time Tag Glitches

Two types of minor frame time code glitches have been observed in the OrbView-2 data. The first is associated with resets of the onboard Global Positioning System (GPS) receiver. The second is of unknown origin, and consists of a shift of exactly 1 s over a period of approximately 30 s. Each of these is described below.

The GPS receiver is the source of the spacecraft orbit data, and also provides a very accurate time signal. On OrbView-2, the GPS time signal is used as the reference for all other spacecraft time codes. At regular intervals, the time codes in the spacecraft computers are compared with the GPS time signal, and adjusted to maintain agreement.

Resets of the GPS receiver have occurred throughout the mission. A reset occurs when the receiver temporarily stops tracking enough GPS satellites to get a valid orbit solution. These events were observed frequently at the start of the mission (September–December 1997). After the spacecraft engineers analyzed the problem, software patches were uplinked to the spacecraft computer and the GPS operating parameters were adjusted, which significantly reduced the number of events. Since January 1998, resets have been observed at very irregular intervals, averaging about one or two per month. Only resets which overlap with GAC data collection affect data quality.

A GPS reset results in errors in the minor frame time tag, and other spacecraft time tags are also affected. The errors appear at the start of the reset event as a series of fractional-second steps, spread over about 1 min. In some cases, the steps cancel out each other. More frequently, they accumulate to a total error of 1 s; this remains for a period of from 15–20 min and is corrected in a single step at the end of the event. In these cases, because the event duration is a large fraction of a GAC scene length, it is common to observe only the start or end of an event.

The second type of minor frame time tag glitch is called the *30 s glitch*, because of the characteristic duration of 30–35 s. This glitch starts with a single shift of exactly 1 s, which is corrected from 30–35 s later. No other spacecraft time tags are affected.

The occurrence of the 30 s glitches was not actually documented until early 2001, when they were observed by the quality control (QC) personnel on the CVT. That they went unobserved for over three years is most likely because of their brevity and (at first) infrequency, which limited the effect on data quality. Following their discovery, the mission data set was analyzed to locate all occurrences. There were 17 events in 1998, 24 in 1999, 59 in 2000, 87 in 2001, and 48 as of the end of August 2002. The timing of the glitches was very irregular. In some cases, multiple glitches occurred in a single GAC scene, while at other times none were observed for weeks. Geographic and temporal analyses have revealed no discernable pattern.

Prior to the fourth reprocessing, the only means for handling scenes affected by time tag glitches was for the QC team to manually fail entire scenes, to exclude them from both further processing and distribution. The decision of whether or not to fail a given scene was made according to the fraction of the data with navigation affected by the glitch, which was usually a joint decision by the QC and Mission Operations team. In the majority of cases (all GAC scenes and many HRPT scenes), each such decision caused some valid data to be lost as well. This approach was highly subjective and, as the frequency of the 30 s glitches increased, it also became a burden on the QC team.

7.2.2 Time Tag Glitch Handling

The approach to handling the minor frame time tag glitches during the level-0-to-1A conversion is based on two principles:

1. Only those glitches which can be reliably detected and corrected, are corrected.
2. The navigation flags in the level-1a data products are used to flag scan lines affected by uncorrected glitches (as a navigation failure condition, which inhibits downstream processing) and indicate those with corrected glitches (no effect on subsequent processing).

The conditions in the first principle are met by the 30 s glitches in the GAC data. They can be detected reliably and automatically, because of their consistent characteristics (single step time tag shift of 1 s, corrected after 30–35 s), their limited effect (no other spacecraft time tags are affected), their brevity (for most glitches, both the start and end occur within a scene), and the magnitude of the shift compared to the GAC minor frame interval of 3.333 s. This last element is important because the frame interval is neither an integer multiple of, or smaller than, the time tag shifts, which can easily be distinguished from missing or repeated minor frames. Once the frames affected by a time glitch are identified, the error is easily corrected by adjusting all of the corresponding time tags by the same amount. (As indicated previously, a GAC minor frame contains five GAC scan lines, and the minor frame time tag is used as the first scan line time. The other four scan line times are extrapolated from the first using the scan line period of 0.666 s. The minor frame time tag correction is, therefore, automatically applied to all five scan lines.)

Unlike the GAC, the specific minor frames affected by a 30 s glitch in HRPT or LAC data cannot be reliably detected. The time interval for these frames is 0.166 s, so the time shift of 1 s is an integer number of minor frames. A forward time shift, therefore, is indistinguishable from a data gap, and a backward shift appears the same as repeated frames, which the level-0-to-1A software is designed to filter out.

As stated previously, the time tag glitches occur simultaneously in all data types (LAC, GAC, and HRPT);

therefore, it should be possible to determine the period affected by a 30 s glitch based on the GAC data. The limiting factor is the GAC frame interval, which is 3.333 s; this means that the start and end times of the glitch period are uncertain by this amount, corresponding to 20 LAC or HRPT frames. To address this, these frames at the start and end of each glitch period are flagged and not corrected.

The following is the approach implemented for handling the 30 s glitches:

1. A database table was developed to store time tag glitch information, consisting of the start and end times, the data type (GAC, or LAC and HRPT), the action to be taken (correct or flag minor frame times within the interval) and the time shift (if correction is indicated).
2. During GAC data processing, any 30 s glitches are detected, and the affected minor frame time tags are corrected prior to the calculation of the scan line time tags. (Note that the original, uncorrected minor frame time tags are also stored with the data.) The glitch time period is added to the database table.
3. Database table entries are also made for LAC and HRPT data as follows: one entry to correct the minor frames within the time range of the corrected GAC frames, one to flag the 20 minor frames prior to this time range, and one to flag 20 minor frames after.
4. During subsequent LAC or HRPT data processing, the table entries are used to correct or flag minor frame time tags.

The GPS reset time tag glitches do not meet the reliable detection and correction criteria, for the following reasons:

- Their start is reflected in multiple time shifts, so there is no single start time for a glitch;
- Their duration causes a significant number of these glitches to span the start or end of a GAC scene, making unambiguous identification difficult;
- The shifts affect multiple spacecraft time tags, particularly in the attitude control system (ACS) telemetry, and;
- The shifts do not occur simultaneously, making reliable correction virtually impossible. Detection of GPS reset glitches is still essentially a manual process.

The approach described above can also be used to flag specified periods with no associated correction, and this approach was chosen for the GPS reset glitches. As GPS resets are detected by the QC or Mission Operations teams, entries are manually added to the database table to flag the affected time periods. Afterward, any affected data sets previously generated are renavigated to apply the flags, and all subsequently processed data are flagged automatically. While this process still requires manual intervention, it has the advantage of allowing only the specific data affected by a glitch to be excluded from further processing, instead of an entire scene being failed.

7.3 NAVIGATION UPDATE

The SeaWiFS navigation processing is performed as part of the level-0-to-1A conversion. The results of navigation processing have been under continual evaluation since launch, and numerous improvements were made prior to the third reprocessing. Following that reprocessing (May 2000), the navigation results for the entire mission up to that time were analyzed, and the results of that analysis were used to develop the modification discussed here. This change was actually incorporated into the operational processing in April 2001, but was not applied to the mission data prior to that time until the fourth reprocessing.

The SeaWiFS navigation accuracy requirement is 1 pixel (1.1 km at nadir) at twice the standard deviation. The accuracy of the navigation processing was evaluated using the method of island targets, which was developed prior to launch (Patt et al. 1997). During the mission, the results of this method have been used to develop modifications which have steadily improved the navigation accuracy (Patt 1999). The current set of navigation algorithms are described in another volume of this series (Patt 2002).

The results from the third reprocessing showed good overall accuracy, but significant seasonal and geographic variations were observed. Specifically, errors in the Southern Hemisphere during February and March frequently exceeded 2 pixels, because of excessive yaw angle errors. These errors were observed, for example, in the HRPT scenes from the Pretoria ground station. With the algorithms in use at that time, however, attempts to reduce the yaw errors for this period (e.g., by adjusting attitude sensor alignments) would have degraded the accuracy during other seasons.

The results also showed that, while the roll angle errors were within the requirement, there were consistent, seasonal variations. Specifically, the errors versus latitude during the months of November–February had a small but distinct curvature, with positive errors near the equator decreasing to negative toward the poles. Figure 28 shows the average roll and yaw errors versus latitude for HRPT data from the last 10 days of February 2001. This illustrates the typical behavior for this period: both the roll error peak near the equator, and the large yaw errors in the Southern Hemisphere.

Because the roll angle is essentially determined from the spacecraft horizon scanner data, the curvature observed during these months suggested a seasonal variation in the shape of the CO_2 layer of the atmosphere as seen by the scanner (Patt and Bilanow 2001). The CO_2 height model used for the third reprocessing already had a seasonal correction for the height and the north–south shift, but the

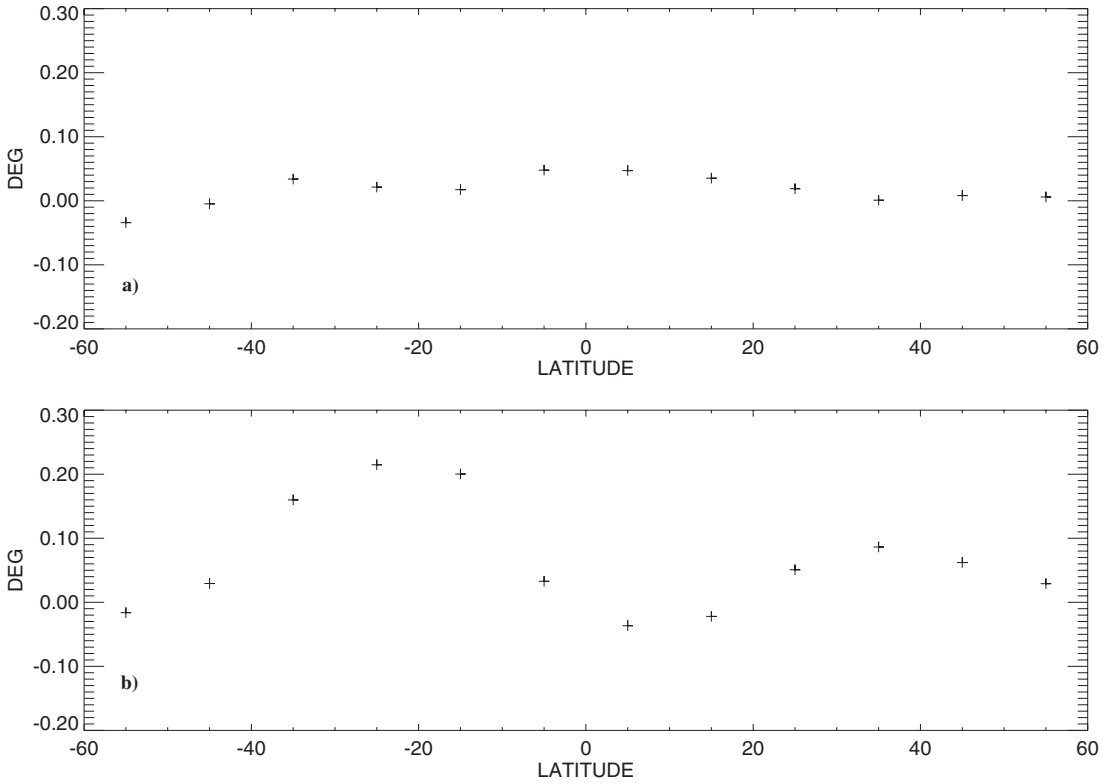

Fig. 28. HRPT data average for the last 10 days of February 2001: **a)** roll errors, and **b)** yaw errors.

shape (as represented by the ellipsoidal flattening factor) was a constant which had been determined for all seasons. An additional correction was added to the model to vary the flattening factor seasonally, with the effect of making the atmosphere slightly more ellipsoidal in November–February than in May–August.

The revised model had the desired effect of minimizing the seasonal roll error variations. It was also found that by incorporating small changes to the attitude sensor alignments, it was possible with the revised model to reduce the maximum yaw errors in the February–March period, without degrading the accuracy at other times. This combination of changes was implemented in April 2001 and used for the fourth reprocessing. The accuracy was evaluated using the island targets method for the entire GAC mission data, and shows the yaw angle errors to be within acceptable limits at all seasons. The HRPT mission data have not yet been reprocessed, but the results for February and March 2002 showed the desired improvement in the Southern Hemisphere. The average HRPT roll and yaw errors for the last 10 days of February 2002 (Fig. 29) show that the roll errors have been flattened out and, more importantly, the Southern Hemisphere yaw errors have been significantly reduced.

7.4 SPACEBIN MODIFICATIONS

This section describes a problem in the initial level-3 processing that was first identified and resolved during the preparations for the OCTS GAC data processing, performed in November 2001. The problem and its solution were also determined to be applicable to SeaWiFS GAC processing, and this modification was adopted for the fourth reprocessing.

The level-3 ocean products generated by SeaWiFS and SIMBIOS follow a convention known as the *data day*. The data day is defined geographically, according to the time when the spacecraft orbit crosses the 180° meridian (hereafter called the *Date Line*) closest to the equator (Podesta 1995).

To apply the data day convention, the level-2–to–3 binning program, `spacebin`, splits any level-2 scenes that cross the Date Line into two level-3 files. The pixels that are west of the date line are assigned to a data day one later than those east of the line. The determination of the appropriate data day involves two separate steps. A program is run to determine the start and end times of the current data day, using the Coordinated Universal Time (UTC) day of the scene as a starting point. Then the binning program logic determines whether each pixel should be associated with the current, previous, or following data day, based on the observation time and location.

During the testing of this processing for the OCTS GAC data, a problem was found in which scenes near the middle of the data day had alternate data days assigned incorrectly. At the time of *spacebin* execution, each scene has been assigned a primary data day, as described in the

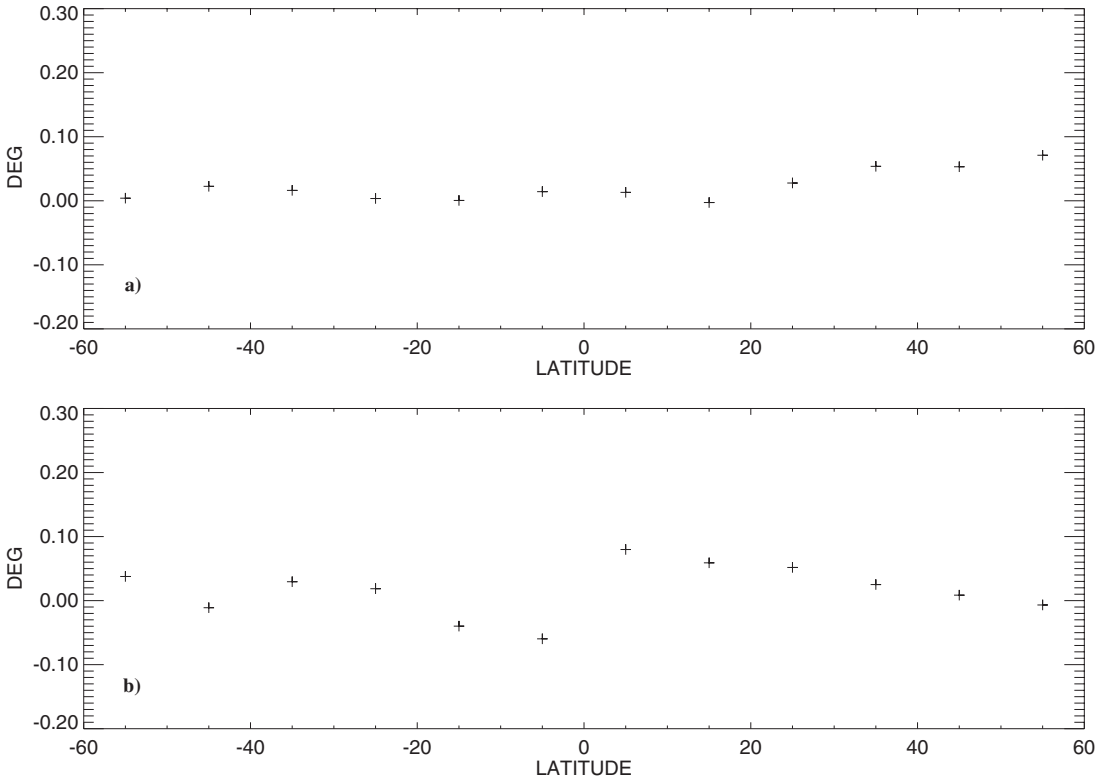

Fig. 29. HRPT data average for the last 10 days of February 2002: **a)** roll errors, and **b)** yaw errors.

previous paragraph. The program then assigns either the previous or following data day as an alternate, to be used if the scene crosses the Date Line. This assignment is performed using the scene time and the data day start and end time. If the scene time falls within the first half of the data day, the previous day is selected as the alternate; otherwise the following day is selected.

During the test runs, it was found that in December and January, scenes near the data day midpoint were sometimes not being binned. Two problems were identified:

1. The selection of the alternate data day was being performed using the scene start time, which biased the selection toward the previous day.
2. The selection was being performed by first checking if the scene time was within 12 h of the data day start time. The data day start and end times are not exactly 24 h apart, because there is not an integral number of orbits per day. For data days less than 24 h long, this logic also biased the selection toward the previous day.

This caused problems in December and January. The low solar declination caused the data collection to extend well past the South Pole, which significantly increased the longitudinal coverage. Each scene spanned nearly the entire daylight part of the orbit. As a result, many scenes collected near 1200 UTC extended from the Greenwich meridian past the Date Line. The incorrect selection of the previous data day as the alternate for these scenes resulted in no data being binned. The solution is twofold. First, the scene center time is used for this selection, rather than the start time. Second, the selection is performed using the actual midpoint of the data day, rather than 12 h from the data day start time.

An example of a scene that is affected by this change is `S2002010114002.L2_GAC`. The start and end times for data day 2002010 are 00:17:59 and 23:38:16 (all times are UTC). Using the previous logic of spacebin, the scene start time (11:40:02) was within 12 h of the data day start time, and so the alternate data day selected was the previous day. This scene crossed the date line at its southern end, resulting in observations that belonged in the following data day. The net result is that no data from this scene were binned for data day 2002010. Using this modified logic, the scene center time (12:01:52) is compared with the data day midtime (11:58:07). Because the scene center time is later, the following data day is selected as the alternate, and the data are binned correctly.

These modifications were implemented in the operational version of spacebin and were used for the fourth reprocessing. The result is that no scenes have failed space binning because of incorrect selection of the alternate data day.

Chapter 8

The SeaWiFS PAR Product

Robert Frouin
Scripps Institution of Oceanography
La Jolla, California

Bryan A. Franz
Science Applications International Corporation
Beltsville, Maryland

P. Jeremy Werdell
Science Systems and Applications, Incorporated
Lanham, Maryland

Abstract

A new SeaWiFS derived product was developed which provides an estimate for the amount of PAR reaching the ocean surface over a 24 hr period. A description of the algorithm is provided in this chapter, followed by comparisons with *in situ* observations. The *in situ* observations include several years of data covering a wide range of solar illumination conditions. The results indicate good algorithm performance, with RMS differences between satellite-retrieved and observed daily average PAR within a few einsteins per square meters per day.

8.1 INTRODUCTION

The SeaWiFS PAR product is an estimate of daily (i.e., 24 hr averaged) PAR reaching the ocean surface. PAR is defined as the quantum energy flux from the sun in the spectral range of 400–700 nm. It is expressed in einsteins per square meter per day. In the sections that follow, the algorithm is described in detail and comparisons are provided with *in situ* observations from two moored buoys, one at the relatively high latitude of British Columbia, and the other in the equatorial Pacific.

8.2 ALGORITHM DESCRIPTION

The PAR algorithm uses plane-parallel theory and assumes that the effects of clouds and clear atmosphere can be decoupled. The planetary atmosphere is, therefore, modeled as a clear sky atmosphere positioned above a cloud layer. This approach was shown to be valid by Dedieu et al. (1987) and Frouin and Chertock (1992). The great strength of such a decoupled model resides in its simplicity. It is unnecessary to distinguish between clear and cloudy regions within a pixel, and this dismisses the need for assumptions about cloud coverage distribution.

For a solar zenith angle θ_0, the incoming solar irradiance at the top of the atmosphere, $E_0 \cos\theta_0$ is diminished by a factor $t_d t_g/(1 - S_a A)$ by the time it enters the cloud–surface system. In these expressions, E_0 is the extraterrestrial solar irradiance at the time of the observation, t_d is the clear sky total (direct plus diffuse) transmittance, t_g is the gaseous transmittance, S_a is the spherical albedo, and A is the cloud–surface system albedo. As the irradiance, $E_0 \cos\theta_0 t_d t_g/(1 - S_a A)$, passes through the cloud–surface system, it is further reduced by $(1 - A)(1 - A_s)^{-1}$. The solar irradiance reaching the ocean surface is then given by

$$E_s \;=\; \frac{E_c(1 - A)}{(1 - A_s)(1 - S_a A)}, \tag{15}$$

where A_s is the albedo of the ocean surface and $E_c = E_0 \cos\theta_0 t_d t_g$ is the solar irradiance that would reach the surface if the cloud–surface system were nonreflecting and nonabsorbing. In clear sky conditions, A reduces to A_s.

To compute E_s, A is expressed as a function of the radiance measured by SeaWiFS in the PAR spectral range (i.e., in bands 1–6, nominal center wavelengths from 412–670 nm). The algorithm works pixel by pixel and proceeds as follows.

First, for each pixel not contaminated by sun glint, the SeaWiFS observed radiance in band i at the top of the atmosphere, $L_t(\lambda_i)$, is transformed into reflectance, $\rho_t(\lambda_i)$, as

$$\rho_t(\lambda_i) \;=\; \frac{\pi L_t(\lambda_i)}{E_0(\lambda_i)\cos\theta_0}, \tag{16}$$

where $E_0(\lambda_i)$ is the extraterrestrial solar irradiance in band i, and θ_0 is the solar zenith angle at the SeaWiFS observation time. The glint areas are not selected because they would be interpreted as cloudy in the PAR algorithm.

Second, $\rho_t(\lambda_i)$ is corrected for gaseous absorption due to ozone

$$\rho'_t(\lambda_i) \;=\; \frac{\rho_t(\lambda_i)}{t_{\rm oz}(\lambda_i)}, \tag{17}$$

with

$$t_{\rm oz}(\lambda_i) \;=\; \exp\!\left\{\frac{-a_{\rm oz}(\lambda_i)C_{\rm oz}}{\cos\theta_0}\right\}, \tag{18}$$

where $a_{\rm oz}(\lambda_i)$ is the ozone absorption coefficient in band i and $C_{\rm oz}$ is the ozone concentration. The ozone concentration is obtained from time and space coincident ancillary data sets distributed by the SeaWiFS Project (Ainsworth and Patt 2000).

Third, the reflectance of the cloud–surface layer, $\rho_s(\lambda_i)$, is obtained from $\rho'_t(\lambda_i)$ following Tanré et al. (1979) assuming isotropy of the cloud–surface layer system. The reflectance is calculated using:

$$\begin{aligned}\rho_s(\lambda_i) \;=\; &\big[\rho'_t(\lambda_i)-\rho_{\rm atm}(\lambda_i)\big]\Big\{t_d(\lambda_i,\theta_0)t_d(\lambda_i,\theta_v)\\ &+ S_a(\lambda_i)\big[\rho'_t(\lambda_i)-\rho_{\rm atm}(\lambda_i)\big]\Big\}^{-1}\end{aligned}, \tag{19}$$

where θ_v is the viewing zenith angle and $\rho_{\rm atm}(\lambda_i)$ is the intrinsic atmospheric reflectance in band i (photons that have not interacted with the cloud–surface layer). The assumption of isotropy is made because no information on pixel composition is available.

In (19), $\rho_{\rm atm}(\lambda_i)$ is modeled using the quasi-single scattering approximation:

$$\rho_{\rm atm} \;=\; \frac{\tau_m P_m + \omega_a\tau_a P_a}{4\cos\theta_0\cos\theta_v}, \tag{20}$$

where τ_m and τ_a are the optical thicknesses of molecules and aerosols, respectively, P_m and P_a are their respective phase functions, and ω_a is the single scattering albedo of aerosols. Wavelength dependence has been dropped for clarity. The total transmittance t_d, and spherical albedo S_a, are computed using analytical formulas developed by Tanré et al. (1979):

$$t_d(\theta) = \exp\!\left\{\frac{-(\tau_m+\tau_a)}{\cos\theta}\right\}\exp\!\left\{\frac{0.52\tau_m+0.83\tau_a}{\cos\theta}\right\}, \tag{21}$$

and

$$S_a \;=\; (0.92\tau_m + 0.33\tau_a)\,e^{-(\tau_m+\tau_a)}, \tag{22}$$

where θ is either θ_0 or θ_v.

The optical thickness of aerosols in band i, $\tau_a(\lambda_i)$, is obtained from the optical thickness in band 8, $\tau_a(\lambda_8)$, and the Ångström coefficient, α, between bands 4 and 8:

$$\tau_a(\lambda_i) \;=\; \tau_a(\lambda_8)\left[\frac{\lambda_8}{\lambda_i}\right]^{\alpha}, \tag{23}$$

where λ_i and λ_8 are nominal wavelengths for SeaWiFS bands i and 8, respectively. A monthly climatology based on three years of SeaWiFS data (1997–2000) is used for $\tau_a(\lambda_8)$ and α, because aerosol properties cannot be determined when the pixel is cloudy. This procedure is also justified because, in general, aerosol effects on E_s are secondary compared to cloud or θ_0 effects.

To estimate ω_a and P_a, the two closest SeaWiFS aerosol models, k and l, that verify $\alpha(l) < \alpha < \alpha(k)$ are selected, and a distance $d_a = \big[\alpha(l)-\alpha\big]\big[\alpha(l)-\alpha(k)\big]^{-1}$ is computed. Using this distance, ω_a and P_a are obtained as follows:

$$\omega_a \;=\; d_a\omega_a(k) \;+\; [1-d_a]\omega_a(l), \tag{24}$$

and

$$P_a \;=\; d_a P_a(k) + [1-d_a]P_a(l), \tag{25}$$

where $\omega_a(l)$ and $\omega_a(k)$ are the single scattering albedos of aerosol models l and k, and $P_a(l)$ and $P_a(k)$ their respective phase functions.

Next, an estimate of daily PAR, $\bar{E}_s$, is obtained by integrating (15) over the length of the day:

$$\bar{E}_s \;=\; \bar{E}_0\int \frac{\cos\theta_0\bar{t}_g\bar{t}_d\big[1-\bar{A}\big]}{\big[1-\bar{A}_s\big]\big[1-\bar{S}_a\bar{A}\big]}dt, \tag{26}$$

with

$$\bar{t}_g \;=\bar{t}_{\rm oz}\bar{t}_{\rm wv}, \tag{27}$$

$$\bar{t}_d \;=\; \frac{\sum_i\big[t_d(\lambda_i)E_0(\lambda_i)\big]}{\sum_i E_0(\lambda_i)}, \tag{28}$$

$$\bar{S}_a \;=\; \frac{\sum_i\big[S_a(\lambda_i)E_0(\lambda_i)\big]}{\sum_i E_0(\lambda_i)}, \tag{29}$$

$$\begin{aligned}\bar{A}_s \;=\; &\left[\frac{0.05}{1.1\cos^{1.4}\theta_0 \;+\; 0.15}\right]\frac{\bar{T}_d}{\bar{t}_d}\\ &+\; 0.08\left(1-\frac{\bar{T}_d}{\bar{t}_d}\right),\end{aligned} \tag{30}$$

$$\bar{T}_d \;=\; \frac{\sum_i T_d(\lambda_i)E_0(\lambda_i)}{\sum_i E_0(\lambda_i)}, \tag{31}$$

$$T_d(\lambda_i) \;=\; \exp\!\left\{\frac{-\big[\tau_m(\lambda_i) \;+\; \tau_a(\lambda_i)\big]}{\cos\theta_0}\right\}, \tag{32}$$

$$\bar{A} \;=F\bar{\rho}_s, \tag{33}$$

$$\bar{\rho}_s \;=\; \frac{\sum_i\rho_s(\lambda_i)}{\sum_i\big[\rho_s(\lambda_i)E_0(\lambda_i)\big]}, \tag{34}$$

where the horizontal line above the variable symbolizes the average value over the PAR range of 400–700 nm, and $\bar{E}_0$ is

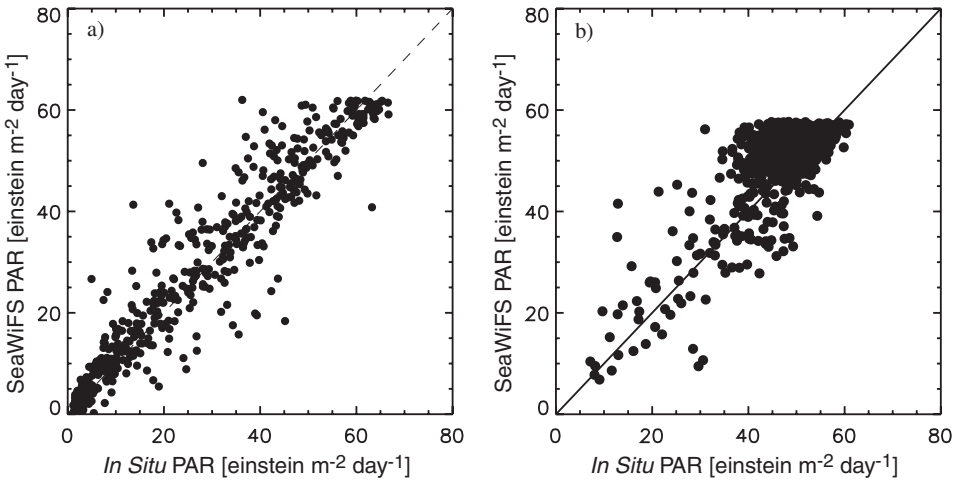

Fig. 30. Scatterplot of daily averaged SeaWiFS PAR against *in situ* PAR from moored buoys near **a)** British Columbia (Halibut Bank) and **b)** the equatorial Pacific (`ep1`).

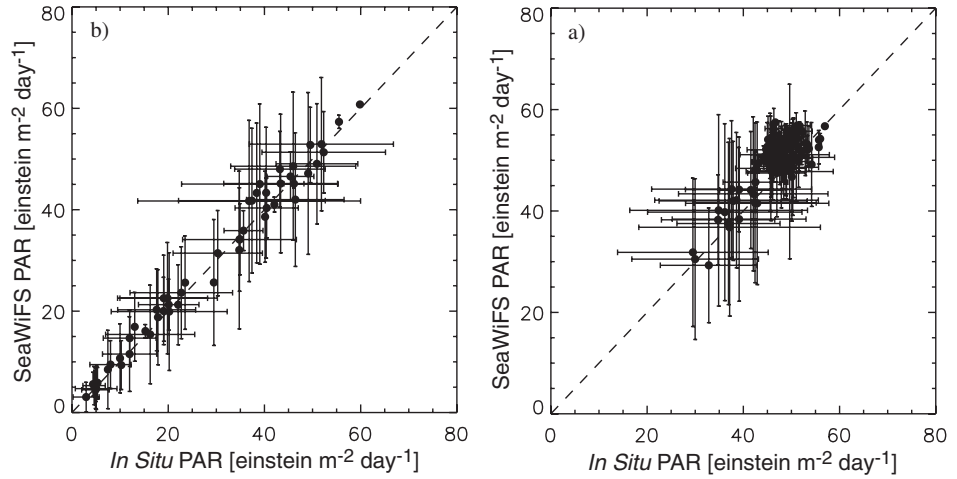

Fig. 31. Scatterplot of 8-day averaged SeaWiFS PAR against *in situ* PAR from moored buoys near **a)** British Columbia (Halibut Bank) and **b)** the equatorial Pacific (`ep1`).

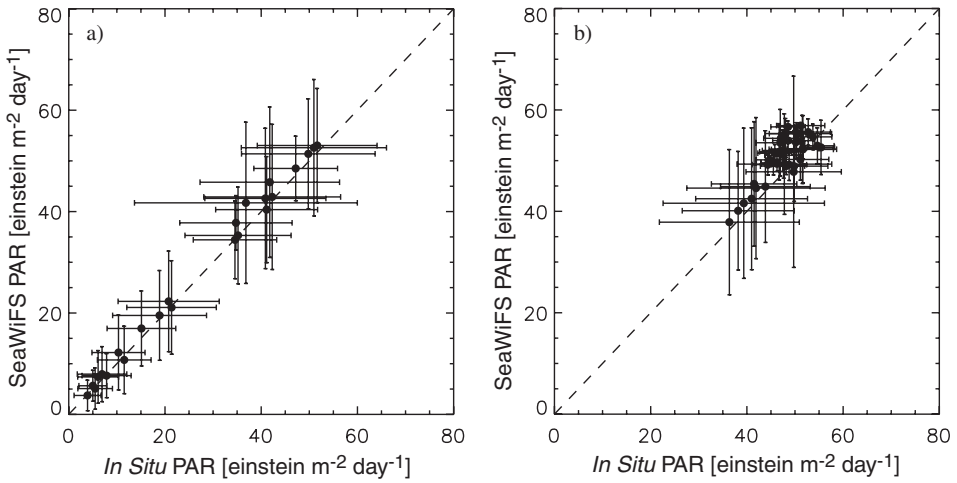

Fig. 32. Scatterplot of monthly averaged SeaWiFS PAR against *in situ* PAR from moored buoys near **a)** British Columbia (Halibut Bank) and **b)** the equatorial Pacific (`ep1`).

Table 8. Performance of the SeaWiFS PAR algorithm at the Halibut Bank and `ep1` mooring sites.

Averaging Period	*Daily*	*8-Day*	*Monthly*
	Halibut Bank		
Correlation coefficient, r^2	0.904	0.984	0.994
Bias†	0.932 (3.3%)	0.863 (3.1%)	1.10 (4.1%)
RMS difference†	6.2 (21.7%)	2.3 (8.2%)	1.8 (6.5%)
Mean†	28.4	28.2	27.2
Number of points	505	54	24
	`ep1`		
Correlation coefficient, r^2	0.613	0.68	0.673
Bias†	2.9 (6.0%)	2.8 (5.8%)	2.8 (5.8%)
RMS difference†	6.2 (12.8%)	4.3 (8.9%)	3.9 (8.0%)
Mean†	48.7	48.3	49
Number of points	882	103	38
	Halibut Bank and `ep1` Combined		
Correlation coefficient, r^2	0.883	0.957	0.978
Bias†	2.2 (5.3%)	2.1 (5.2%)	2.2 (5.4%)
RMS difference†	6.2 (15.0%)	3.7 (9.1%)	3.3 (8.0%)
Mean†	41.3	41.4	40.6
Number of points	1387	157	62

† In units of einstein $\mathrm{m}^{-2}\,\mathrm{day}^{-1}$.

the mean extraterrestrial solar irradiance within that spectral range. The direct transmittance through the atmosphere is denoted as T_d. The summation over wavelength indicated in (28), (29), (31), and (34) is performed over SeaWiFS bands 1–6.

The integration over time expressed in (26) is performed from sunrise to sunset of the day and location of the SeaWiFS observation. It should be noted that, with the exception of $\bar{E}_0$ and $\bar{S}_a$, all terms within the integral will vary with time of day in accordance with the change in solar zenith angle.

In the expression of $\bar{t}_g$ (27), the effect of both ozone and water ($\bar{t}_{\mathrm{oz}}$ and $\bar{t}_{\mathrm{wv}}$, respectively) is modeled according to Frouin et al. (1989).

Following Briegleb and Ramanathan (1982), surface albedo (30) is parameterized as a function of solar zenith angle and fractions of direct and diffuse incoming sunlight, with the diffuse component fixed at 0.08. The direct and diffuse components are weighted by the respective fractions of direct and diffuse transmittance. This parameterization, which takes into account Fresnel reflection and diffuse upwelling radiation, is sufficient because the influence of $\bar{A}_s$ on surface PAR is small. In some cases, however, the retrieved $\bar{A}$ might be less than $\bar{A}_s$. When this happens, $\bar{A}$ is fixed to $\bar{A}_s$.

The dependence of A on solar zenith angle (33) is taken into account via the angular factor, F. Rather than using angular models determined statistically (e.g., Young et al. 1998), F is computed from analytical formulas proposed by Zege et al. (1991) for nonabsorbing, optically thick scattering layers. The available angular models are fairly similar for partly cloudy, mostly cloudy, and overcast conditions, and they compare reasonably well with the Zege et al. (1991) formulas.

The cloud–surface system, however, is assumed to be stable during the day and to correspond to the SeaWiFS observation. This assumption is crude, and PAR accuracy will be degraded in regions where clouds exhibit strong diurnal variability. Still, useful daily PAR estimates would be obtained by averaging in space and time. Note that the algorithm yields a daily PAR estimate for each instantaneous SeaWiFS pixel.

Finally, the individual daily PAR estimates, obtained in units of $\mathrm{mW\,cm^{-2}\,\mu m^{-1}}$, are converted into units of einsteins per square meter per day (einstein $\mathrm{m}^{-2}\,\mathrm{day}^{-1}$) and averaged into 9 km resolution, daily, weekly, and monthly products. The factor required to convert units of $\mathrm{mW\,cm^{-2}\,\mu m^{-1}}$ to units of einstein $\mathrm{m}^{-2}\,\mathrm{day}^{-1}$ is equal to 1.193 to an inaccuracy of a few percent regardless of meteorological conditions (Kirk 1994). In middle and high latitudes, several daily estimates may be obtained over the same target during the same day, increasing product accuracy.

8.3 *IN SITU* MATCH-UP COMPARISON

An evaluation of the SeaWiFS PAR estimates was performed using several years of *in situ* PAR measurements from moored buoys off the west coast of Canada (Halibut Bank data set, 49.34°N–123.73°W) and in the central equatorial Pacific (`ep1` data set, 0.00°N–155.00°W). The total number of days used in the evaluation is 1387 (882 for

ep1 and 505 for Halibut Bank). Scatterplots of SeaWiFS versus *in situ* values are displayed in Figs. 30, 31, and 32 for daily, weekly, and monthly averages, respectively, and comparison statistics are summarized in Table 8. Agreement with *in situ* measurements is good, with RMS differences of 6.2(15.0%), 3.7(9.1%), and 3.3(8.1%) einstein m^{-2} day^{-1} on daily, weekly, and monthly time scales, respectively, when the ep1 and Halibut Bank data sets are combined.

The SeaWiFS estimates are higher by approximately 1 einstein m^{-2} day^{-1} at Halibut Bank and by approximately 3 einstein m^{-2} day^{-1} at the ep1 location. Overestimation at the ep1 location is due to less cloudiness at local noon (about the time of satellite overpass) than during the afternoon. A further verification was made using 16 days of data collected at the Bermuda Bio-optical Program (BBOP) site. Similar statistics were obtained for daily values, i.e., an RMS difference of 5.6(16%) einstein m^{-2} day^{-1} and a negligible bias.

The results presented above indicate good algorithm performance. One should be aware of the limitations of the algorithm, which ignores the diurnal variability of clouds. This variability will be introduced statistically, as a function of geographic location and month of year, in a future, improved version of the algorithm.

Acknowledgments

The authors wish to thank Francisco Chavez of the Monterey Bay Research Institute, Monterey, California, for providing the ep1 data set; James Gower of the Institute of Ocean Sciences, Sidney, B.C., Canada, for providing the Halibut Bank data set; and David Siegel of the University of California, Santa Barbara, California, for providing the BBOB data set.

Chapter 9

A Partially Coupled Ocean–Atmosphere Model for Retrieval of Water-Leaving Radiance from SeaWiFS in Coastal Waters

Richard P. Stumpf
NOAA Center for Coastal Monitoring and Assessment
Silver Spring, Maryland

Robert A. Arnone, Richard W. Gould, Jr., and Paul M. Martinolich
Naval Research Lab
Stennis, Mississippi

Varis Ransibrahmanakul
SPS Technologies
Silver Spring, Maryland

Abstract

The global atmospheric correction algorithm for SeaWiFS tends to over correct for the atmosphere in coastal waters because of water-leaving radiance (L_W) in the NIR part of the spectrum, λ_r. This $L_W(\lambda_r)$ phenomenon occurs particularly in water with high inorganic particulate levels. An iterative solution is used to solve this problem. A bio-optical model is used to determine the NIR backscatter from the backscatter at 670 nm, and specifically addresses inorganic particulates. This solution requires compensation for absorption by chlorophyll, detrital pigments, and gelbstoff (colored dissolved organic matter). The $L_W(\lambda_r)$ is found and removed from the total radiance so that the standard atmospheric models can be applied. Chlorophyll *a* concentrations, C_a, in coastal and Case-2 waters are reduced to appropriate levels. The algorithm cannot yet correct areas where negative L_W occurs at 670 nm.

9.1 INTRODUCTION

The use of satellites to monitor the color of the ocean requires effective removal of the atmospheric signal. The methods for treating the atmosphere have depended on the high absorption of red and NIR light by water. In open ocean water where only C_a and related pigments determine the optical properties, water can be considered to absorb all light, so that the signal observed by the satellite should result entirely from the atmospheric path radiance. While the scattering due to Rayleigh, and absorption due to ozone and other gases can be treated through computation with appropriate lookup tables to address seasonal and latitudinal effects (Gordon et al. 1983 and Gordon and Wang 1994), the aerosol optical depth must be computed for each pixel.

The aerosol correction has required determination of two major factors:

1) The amount of aerosol, characterized by the optical depth; and
2) The type of aerosol, which determines the size distribution and apparent color, and is characterized by either the Ångström exponent, or ϵ.

The atmospheric correction for the Coastal Zone Color Scanner (CZCS) used a band at 665 nm (CZCS band 4) to provide a correction for the aerosol optical depth (Gordon et al. 1983), with additional assumptions about the spectra for water with negligible C_a (Gordon and Clark 1981), and calculates the ϵ value for each scene (but not each pixel). The 665 nm band is positioned where the absorption of water becomes significant (Table 9), thus, the entire radiance in the CZCS correction is presumed to originate in the atmosphere.

It was recognized immediately that water with a detectable scattering component, in particular inorganic sediment, had detectable radiance at this wavelength. Smith and Wilson (1981) proposed an iterative solution based on assumptions of the spectral relationship between 443, 550, and 670 nm. Later, Mueller (1984) proposed another so-

lution using C_a to estimate the radiance at 670 nm. In both solutions, the estimated water-leaving radiance (L_W) at 670 nm is removed from the signal, then the normalized water-leaving radiances, L_{WN}, are recalculated and the L_W values are re-estimated. When the change in L_{WN} values becomes negligible, the iteration ends. Gould and Arnone (1994) altered the approach by using estimates of the diffuse attenuation to obtain the estimated L_W, and significantly improved the usefulness of CZCS data in clearer Case-2 waters. While these are the best approaches for CZCS, these iterations are based on in-water optical properties which are limited by their dependence on consistent spectral relationships between the bands. These spectral relationships will vary with changes in the optical constituents. In addition, use of the 670 nm band for atmospheric correction can produce unpredictable results as $L_W(670)$ can also become greater than the aerosol radiance [$L_a(670)$], making the result unreliable. The iteration further depends on consistent spectral relationships between the bands. These relationships can vary owing to changes in the optical constituents.

Table 9. Water absorption at the SeaWiFS bands (Curcio and Perry 1951, Palmer and Williams 1974, Smith and Baker 1981, and Pope and Fry 1997).

Band No.	*Wavelength* [nm]	*Bandwidth* [nm]	*Absorption* [m^{-1}]
1	412	20	0.00450
2	443	20	0.00700
3	490	20	0.01500
4	510	20	0.03250
5	555	20	0.06000
6	670	20	0.43000
7	765	40	2.50000
8	865	40	4.30000

With SeaWiFS, bands for atmospheric correction were introduced in the NIR at 765 and 865 nm (Table 9). The absorption of water at these bands is sixfold and tenfold, respectively, of the absorption at 665 nm, producing negligible water-leaving radiance in most Case-1 waters. In addition, the two bands offer a means of deriving an atmospheric model that adjusts for aerosol type by determining $\epsilon(\lambda_i, \lambda_j)$ at each pixel, where ϵ relates the aerosol radiance at band λ_i to a reference band λ_j (Gordon and Wang 1994). In coastal waters having high concentrations of scattering material, water-leaving radiance can still occur in the NIR, an effect noted previously by researchers using other sensors that had NIR bands [Moore (1980), Stumpf and Tyler (1988), and Stumpf and Pennock (1989)].

The presence of water-leaving radiance in the NIR introduces two sources of error into the removal of the aerosol. First, the total aerosol is overestimated as some of the total radiance (L_t) at 865 nm derives from the water. Second, as the absorption of water changes from 765–865 nm, the selection of the appropriate atmospheric model is affected, causing an error in the extrapolation of the aerosol radiance to the shorter wavelengths. As a result, the atmospheric radiances will be overestimated at all bands with increasing severity for shorter wavelengths, even leading to negative radiances in the blue bands in coastal water. This results in severe errors, if not complete failure, of various algorithms for C_a and optical properties.

To solve this problem, iterative solutions were proposed. Land and Haigh (1996) developed a solution for SeaWiFS that involved modeling the water reflectance and atmospheric aerosol at all wavelengths to convergence. They attempted to solve simultaneously for both the ocean and atmosphere at all wavelengths. While a promising solution, this attempt puts severe demands on the accuracy of the bio-optical model.

For the Medium Resolution Imaging Spectrometer (MERIS), Moore et al. (1999) developed an iteration based on three NIR bands to estimate the NIR water radiance based on the Gordon and Wang (1994) solution. This solution is promising, but does not apply to SeaWiFS or MODIS, both of which have fewer NIR bands.

Gould et al. (1998) proposed an iteration for SeaWiFS that determined NIR scattering from 670 nm scattering, which is the basis for the scattering component presented here. The solution addressed only the absorption by water.

Ruddick et al. (2000) developed a method that solves for the aerosol radiance and L_W simultaneously in the NIR to good results in highly scattering systems in the North Sea. This method uses a single aerosol type (constant ϵ value) determined manually, which poses problems for automated processing.

Hu et al. (2000b) developed a technique to transfer the ϵ value from the nearest clear water. While potentially effective, it depends on the aerosol type remaining spatially constant in the coastal zone, potentially over hundreds of kilometers.

Siegel et al. (2000) developed an iterative technique that presumed the backscatter to covary with C_a and used the Gordon and Wang model to solve for the NIR backscatter. This model has been implemented by NASA, but is most effective in Case-1 water or in water where sediment covaries with C_a.

The information presented in this chapter is a partially coupled solution for SeaWiFS (and ultimately MODIS), where the scattering problems of atmosphere and water scattering in the NIR are coupled. A variation on this model was implemented into the atmospheric correction program within the processing software for the fourth reprocessing of the SeaWiFS data set (Chapt. 4).

9.2 METHODS

The development of an algorithm that couples to the Gordon and Wang (1994) atmospheric correction involves several components. The first involves identifying the necessary change in the atmospheric correction. The second

involves the theory and bio-optical models used to determine the water-leaving radiance $L_W(\lambda_r)$, and third is the iterative process.

9.2.1 NIR Concept

Gordon and Wang (1994) (henceforth referred to as GW94) describe the solution for $L_t(\lambda)$:

$$L_t(\lambda) \;=\; L_r(\lambda) \;+\; [L_a(\lambda) \;+\; L_{\rm ra}(\lambda)] \;+\; t(\lambda)L_W(\lambda), \quad (35)$$

where $L_t(\lambda)$ is the radiance at the top of the atmosphere, $L_r(\lambda)$ is the Rayleigh scattering radiance, $L_a(\lambda)$ is the aerosol scattering radiance, $L_{\rm ra}(\lambda)$ is the interaction between molecular and aerosol scattering radiance, $t(\lambda)$ is the diffuse transmittance through the atmosphere, and $L_W(\lambda)$ is the water-leaving radiance. A basic assumption of the GW94 atmospheric correction approach is that $L_W(\lambda_r)$ is negligible. This assumption allows for the selection of an aerosol model using

$$L_a(\lambda_r) \;+\; L_{\rm ra}(\lambda_r) \;=\; L_t(\lambda_r) \;-\; L_r(\lambda_r). \quad (36)$$

If $L_W(765)$ and $L_W(865)$ are not negligible, the right side of (36) is increased, introducing two different errors in the determined aerosols. First, if $L_W(865)$ is not negligible, then $L_a(865) + L_{\rm ra}(865)$ is overestimated. This means that more aerosol is determined than is present, resulting in overcorrection for aerosols at all bands, producing $L_W(\lambda_r)$ to be lower than is the case. Second, with $L_W(765)$ not negligible, the aerosol type will be in error. The absorption by water at the SeaWiFS bands varies (Table 9), and at 765 nm it is 57% of that at 865 nm. As a result, $L_W(765) > L_W(865)$, and water-leaving radiance that is interpreted as aerosol will have a high ϵ value. For the extreme case of an atmosphere with no aerosol, water-leaving radiance at 765 and 865 nm would result in $\epsilon(765, 865) \approx 2.2$, almost double the highest value for a true aerosol reported in GW94, and much higher than $\epsilon(765, 865) \approx 1$ observed for marine aerosols. The resultant atmospheric model will lead to an overcorrection error where the overcorrection increases with shorter wavelength. Where the water already has low reflectance in the blue bands, such as in Case-2 water, the overcorrection would produce negative L_W in blue bands. Accordingly, a solution for $t(\lambda)L_W(\lambda_r)$ is needed.

9.2.2 Bio-Optical Models for NIR Iteration

Because of the strong absorption at the wavelengths of interest the relationship of remote sensing reflectance ($R_{\rm rs}$) to the inherent optical properties, backscatter (b_b) and total absorption ($a_{\rm tot}$) is reduced from the general form (adapted from (4) in Gordon et al. 1988):

$$R_{\rm rs}(\lambda) \;=\; y\frac{T_w}{Q(\lambda)}\;\frac{b_b(\lambda)}{b_b(\lambda) + a_{\rm tot}(\lambda)}, \quad (37)$$

to the linear form

$$R_{\rm rs}(\lambda) \;\simeq\; y\frac{T_w}{Q(\lambda)}\;\frac{b_b(\lambda)}{a_{\rm tot}(\lambda)}, \quad (38)$$

where in (37) and (38), T_w is the transmission and refraction loss at the air–water interface; and Q is the factor E_u/L_u, where E_u and L_u are the upwelling irradiance and radiance, respectively. The Q-factor is often assumed to be π, although the value is somewhat larger and variable. The variable y is the l_1 value from Gordon et al. (1988) times Q.

The linear form of (38) assures a stable iteration at high reflectance, although (37) shows that $R_{\rm rs}(\lambda)$ should approach $(y[T_w/Q(\lambda)])$ asymptotically without exceeding it. Ruddick et al. (2000) also showed that the linear solution is an accurate estimator of the Gordon et al. (1988) solution in the NIR.

The backscattering term (b_b), is the sum of b_b from pure water ($b_{\rm bw}$) and b_b from particles ($b_{\rm bp}$). The particle concentration and the scattering efficiency (size characteristics and the index of refraction) influence spectral b_b. Gould et al. (1999) determined that the spectral shape of b_b is linear in coastal waters. The backscatter is sufficient to produce measurable reflectance in the NIR part of the spectrum (Ruddick et al. 2000 and Siegel et al. 2000).

For the iterative solutions, $R_{\rm rs}$ is estimated at the critical NIR wavelengths, λ_r, from $R_{\rm rs}$ from a reference band, λ_j, using a solution of (38):

$$R_{\rm rs}(\lambda_r) \;=\; R_{\rm rs}(\lambda_0)\,\frac{a_{\rm tot}(\lambda_0)}{a_{\rm tot}(\lambda_r)}\,r_{\rm bb}(\lambda_r, \lambda_j), \quad (39)$$

where the backscatter relationship ($r_{\rm bb}$) is

$$r_{\rm bb}(\lambda_r, \lambda_j) \;=\; \left[\frac{b_b(\lambda_r)}{b_b(\lambda_j}\right]^{\eta}, \quad (40)$$

and η is a constant. As $b_{\rm bp} >> b_{\rm bw}$, it is only necessary to determine $r_{\rm bb}$ rather than the actual backscatter. For the two NIR bands, λ_r becomes λ_i, and λ_j is 670 nm.

Gould et al. (1999) concluded that the Petzold volume scattering function, b, varied linearly with wavelength, and $b_b \approx 0.02b$. Their result gives a spectral relationship for backscatter in coastal waters:

$$b_b(\lambda) \;=\; -0.00113\lambda \;+\; 1.62517, \quad (41)$$

with $\eta = 1$ in (40). If no spectral dependence existed, then either $\eta = 0$ or $B_0 = 0$.

The total absorption is

$$a_{\rm tot}(\lambda) \;=\; a_w(\lambda) \;+\; a_{\rm ph}(\lambda) \;+\; a_{\rm dg}(\lambda), \quad (42)$$

where a_w, $a_{\rm ph}$, and $a_{\rm dg}$ are the coefficients of absorption due to water, phytoplankton, and dissolved or detritus matter, respectively. For the 670 nm band, all three terms

are determined; for the 765 and 865 nm bands, $a_{\rm ph}$ and $a_{\rm dg}$ are presumed to be negligible.

The a_w term is determined from tabulated values from Palmer and Williams (1974) and Pope and Fry (1997), with additional data from Curcio and Petty (1951) and Smith and Baker (1981). The $a_{\rm ph}$ term is found using data from Morel and Gentili (1991) with tuning of $a_{\rm ph}(440)$ to the SeaBAM data set (O'Reilly et al. 1998, and Maritorena and O'Reilly 2000):

$$a_{\rm ph}(440) \;=\; 0.08(C_a)^{0.65}. \qquad (43)$$

Using Bricaud et al. (1998), and Lee et al. (1998) $a_{\rm ph}$ is obtained:

$$a_{\rm ph}(\lambda) \;=\; a_{\rm ph}(440)\,[A_0(\lambda) + A_1(\lambda)\,\ln a_{\rm ph}(440)]. \qquad (44)$$

While $a_{\rm ph}$ is determined everywhere; for $C_a < 1 \mu{\rm g\,L^{-1}}$, it becomes negligible as $a_{\rm ph}/a_w < 0.05$.

In coastal waters such as river plumes, detrital and gelbstoff absorption can be significant. Absorption at 400 nm of 1–20 $\rm m^{-1}$, corresponds to an absorption at 670 nm of 0.04–0.7 $\rm m^{-1}$, which is greater than $a_{\rm dg}(400)$ in some Case-1 waters. An analysis of field data has shown that the $a_{\rm dg}$ value may be approximated by using the 555 and 670 nm bands. For coastal waters, which includes waters having extremely high $a_{\rm dg}$ values, the extreme absorption in the blue eliminates the information content of the 412 and 443 nm bands for determining $a_{\rm dg}(412)$ (Carder et al. 1999). As a result, a semi-analytical solution is employed using the 555 and 670 nm bands, using the ratio of $R_{\rm rs}(555)$ and $R_{\rm rs}(670)$, where

$$a_{\rm dg}(670) \;=\; 0.147 \;-\; 0.18X, \qquad (45)$$

when

$$X \;=\; \frac{R_{\rm rs}(555) \;-\; R_{\rm rs}(670)}{R_{\rm rs}(555)}. \qquad (46)$$

The coefficients in (44) were determined by fitting X to derived $a_{\rm dg}$ (Fig. 33). The effectiveness of this method is shown from field data where it is dominated by $a_{\rm dg}$ (Fig. 34). For areas offshore, $a_{\rm dg}(670)$ is negligible. An additional analysis compared estimated $R_{\rm rs}(412)$ [using (41)–(46) in (38)] to observed $R_{\rm rs}(412)$, including water with extremely high dissolved absorption. The solution uses $a_{\rm dg}(412) = a_{\rm dg}(670)\exp[0.013(670-412)]$. The comparison shows the ability to estimate $a_{\rm dg}(670)$ is meaningful even when using it to extrapolate to 412 nm (Fig. 35).

9.2.2.1 NIR Iteration Application

In the SeaWiFS processing, (39) was implemented using an iterative computation of $L_W(765)$ and $L_W(865)$. The procedure is based on the original SeaWiFS processing code using the GW94 atmospheric model. The goal is to remove the $L_W(\lambda_r)$ component from $L_t(\lambda_r)$, so that only the atmospheric component of $L_t(\lambda_r)$ is input into GW94. The iteration first uses $L_t(\lambda_r)$ as input to GW94 in order to solve for $L_W(670)$, as would be done in any noniterative method. Then, $L_W(670)$ is used through the model described in (39) to determine $L_W(\lambda_r)$ [i.e., $L_W(765)$ and $L_W(865)$]. These are propagated to the top of the atmosphere (correcting L_W for the direct transmittance $T(\lambda)$ determined from the GW94 atmospheric model). This TOA $L_W(\lambda_r)$ is removed from $L_t(\lambda_r)$ which is then input into the GW94 computation.

0-iteration:
$L_t(\lambda_r)$ is input into GW94, whose output goes into $R_{\rm rs}(\lambda_v)$, where (λ_v) are the visible wavelengths; $R_{\rm rs}(670)$ is input into (39), whose output $R_{\rm rs}(\lambda_r)$ is

$$L_t(\lambda_r)_1 \;=\; L_t(\lambda_r) \;-\; T(\lambda_r)\,R_{\rm rs}(\lambda_r)_0\,F_0(\lambda_r). \qquad (47)$$

1-iteration:
$L_t(\lambda_r)_1$ is input into GW94, the output of which goes into $R_{\rm rs}(\lambda_v)_1$; $R_{\rm rs}(670)_1$ is input into (39), whose output $R_{\rm rs}(\lambda_r)_1$ is

$$L_t(\lambda_r)_2 \;=\; L_t(\lambda_r)_1 \;-\; T(\lambda_r)\,R_{\rm rs}(\lambda_r)_1\,F_0(\lambda_r). \qquad (48)$$

If $\Delta R_{\rm rs}(765) = R_{\rm rs}(\lambda_{\rm ir})_1 - R_{\rm rs}(\lambda_{\rm ir})_0 > 10^{-5}\,{\rm sr^{-1}}$ then continue the iteration; else stop the iteration.

The iteration is not performed if the initial $R_{\rm rs}(765) < 5\times10^{-5}{\rm sr^{-1}}$ or if $L_W(670) < 0$, and the iteration stops when $\Delta R_{\rm rs}(765)$ (the change between iterations) is less than $10^{-5}\,{\rm sr^{-1}}$.

The minimum threshold to initiate iteration constrains the solution to water having a significant scattering signal. Even in oligotrophic Case-1 water, such as the Loop Current in the Gulf of Mexico, SeaWiFS has sufficient sensitivity that two iterations could be performed if some constraint were not applied. The process is run for up to eight iterations; although convergence is generally achieved in two iterations, and rarely takes more than four.

The atmospheric error tends to cause a greater error at shorter wavelengths, which has a potential impact on the iterative solution. The underestimate results in the C_a and $a_{\rm ph}$ being overestimated. To prevent overestimation of $a_{\rm tot}(670)$ and the resultant overcorrection, the C_a concentrations in the computation are limited on the first two iterations. The C_a value is not allowed to be greater than $10\,\mu{\rm g\,L^{-1}}$ as an input to the computation of the first iteration, and not greater than $20\,\mu{\rm g\,L^{-1}}$ in the computation of the second iteration. (The C_a product is not limited in any way.) If $L_W(555) < 0$ during any iteration, then only $a_w(670)$ is used in the computation of $a_{\rm tot}(670)$, as neither $a_{\rm ph}(670)$ nor $a_{\rm dg}(670)$ is determined. In most areas, C_a and detrital–gelbstoff absorption are not as critical as water absorption in determining $a_{\rm tot}(670)$. In some estuaries and river plumes, detrital and dissolved absorption produce a significant effect.

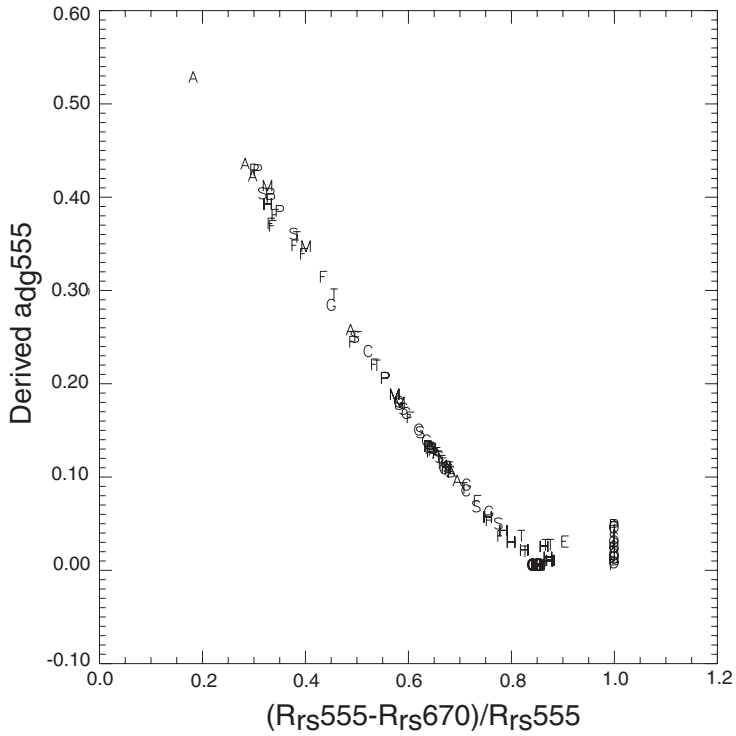

Fig. 33. Comparison of $X = [R_{\rm rs}(555) - R_{\rm rs}(670)]/R_{\rm rs}(555)$ to $a_{\rm dg}(555)$ derived from spectral model. The labels indicate locations of field data: `P`=Pamlico, `T`=Tampa Bay, `A`=Alabama shelf, `F`=Florida Bay, `S`=South Atlantic Bight, `G`= Gulf of Mexico, `H`=North Carolina shelf; the best fit to this solution is (45). The derived $a_{\rm dg}$ came from the total absorption, (38), less the phytoplankton absorption, (44).

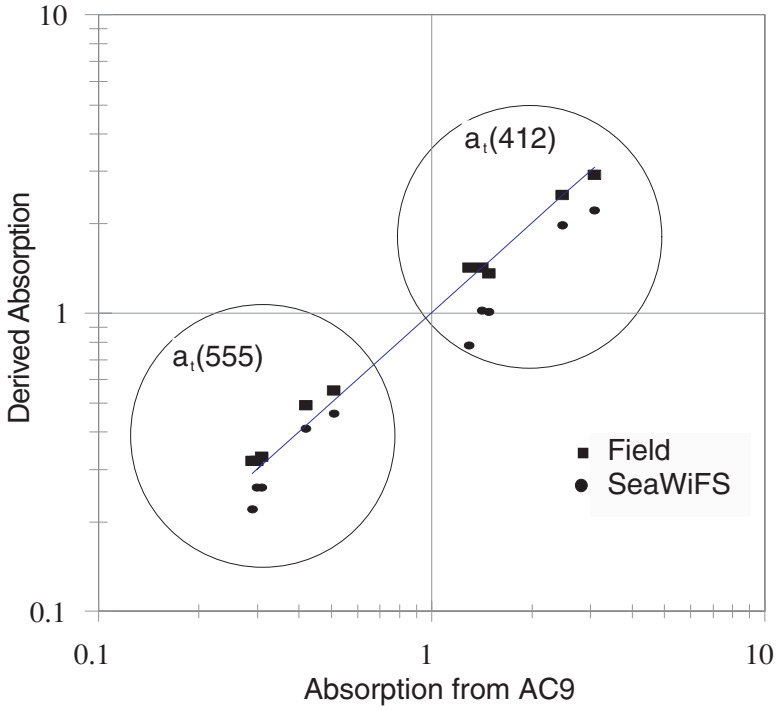

Fig. 34. The derived total absorption ($a_{\rm tot}$) at 412 and 555 nm compared with AC-9. The coastal $a_{\rm dg}$ computation applies at these sites and $a_{\rm dg}$ produces over 90% of the total absorption at these bands. The derived total absorption ($a_{\rm tot}$) used $R_{\rm rs}$ with (44) and (45).

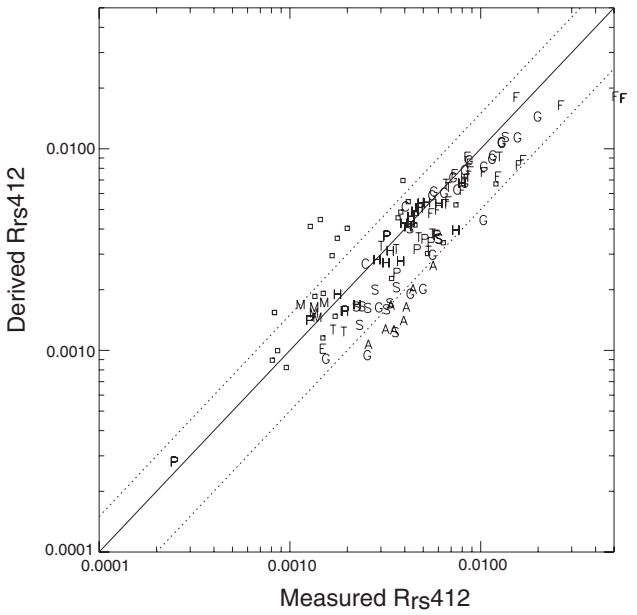

Fig. 35. Estimated $R_{\rm rs}(412)$ versus observed $R_{\rm rs}(412)$ using the Gulf of Mexico–South Atlantic Bight data set developed as part of this study. The SeaBAM tuning was applied here. The boxes are samples that did not have a 670 nm value, so the coastal $a_{\rm dg}$ could not be used. The letters denoting locations are the same as in Fig. 33. The estimate accounts for 83% of the variance in the measured $R_{\rm rs}(412)$.

The iterative solutions were implemented in the SeaWiFS Data Analysis System (SeaDAS) version 4 and were applied to pixels containing the station taken within one day of the sample. The standard calibration was applied. The C_a value was found using version 2 of the Ocean Chlorophyll (OC2) algorithm (Maritorena and O'Reilly 2000).

9.3 RESULTS

SeaWiFS imagery was processed using the iterative technique for the northern Gulf of Mexico, South Atlantic Bight, and the East Coast. In the coastal zone of the Gulf of Mexico, scattering due to suspended particulate matter is significant, as well as absorption from dissolved and detrital materials.

The NIR iteration produces a substantial decrease in the correlation of $L_a(865)$ with $L_W(670)$ (Figs. 36 and 37). Without the NIR iteration, a strong correlation exists between aerosol radiance and water-leaving radiance [the smallest values of $L_a(865)$ for each $L_a(670)$]. For pixels with the lowest aerosol, $L_a(865)$ increased at about $0.07L_W(670)$ with a noniterative process. After the iteration, most of the correlation has been removed, with $L_a(865)$ showing a negligible change for $L_W(670) < 1.5\,\mathrm{mW\ cm^{-2}\,\mu m^{-1}\,sr^{-1}}$ (or $R_{\rm rs}(670) < 0.0096\,\mathrm{sr^{-1}}$). The $L_a(865)$ value shows a weak correlation for greater $L_W(670)$, with $L_a(865)$ changing at approximately $0.015\times$ Ł$_W(670)$. These areas are among the highest scattering found, including the core Mississippi River plume and Florida Bay during major resuspension events (of calcium carbonate sediments). The linearization of the relationship of $R_{\rm rs}$ to the optical properties (b_b and a) in (39) produces a negligible effect for low $R_{\rm rs}(670)$. Ruddick et al. (2000) noted that for the ratio of NIR reflectances, the linearized form produced only small errors.

A comparison of the iterative and noniterative method shows that the iterative techniques increase reflectance at shorter wavelengths (Fig. 38). The noniterative and Siegel process produces a strong spectrally dependent bias against field measurements (Fig. 39), while the NIR iteration reduces both the bias and the RMS error against the measured data (Figs. 39 and 40). With the reduction in the spectral component of the bias, the calculated C_a value from SeaWiFS becomes more consistent with that calculated from field radiometry (Fig. 41).

In order to prevent iteration from occurring unnecessarily in extremely clear waters, iteration does not take place if $R_{\rm rs}(765) > 5\times10^{-5}$. This suggests that some NIR water-leaving radiance may be present in most Case-1 water (Siegel et al. 2000). The iteration is based on the spectral characteristic of backscatter by inorganic sediments. In Case-1 water (which does not have inorganic scattering), the spectral backscatter relationship, $r_{\rm bb}(\lambda_r, 670)$, will be influenced by phytoplankton and may differ from that used here. Phytoplankton tends to produce much less backscatter than inorganic particles, so the errors in using a sediment-based $r_{\rm bb}(\lambda_r, 670)$ may be small, even though phytoplankton does produce some NIR scattering (Siegel et al. 2000). The potential for error, however, in high chlorophyll Case-1 waters should be examined.

The NIR iteration does not remove all negative radiances, indicating that other factors, probably absorbing aerosols, are also involved in this error (Figs. 39 and

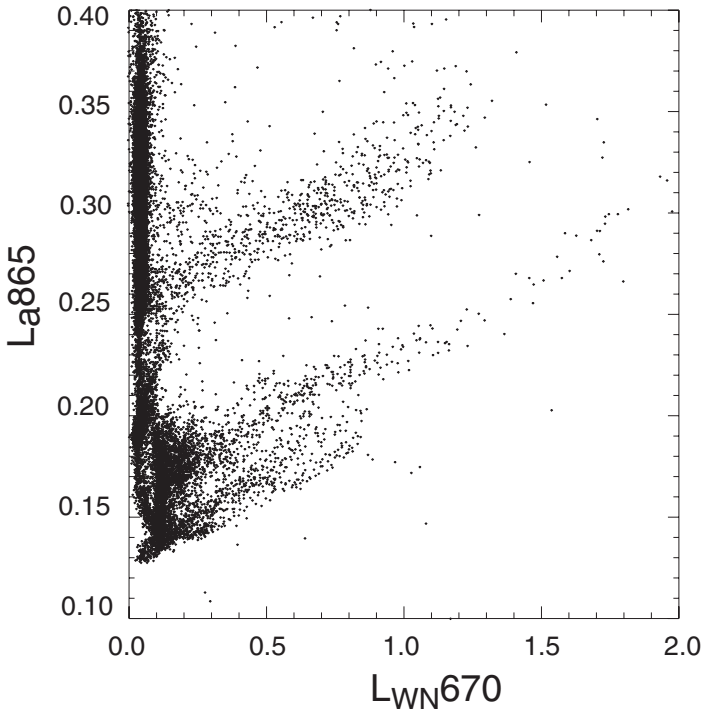

Fig. 36. Comparison of $L_a(865)$ with a $L_{WN}(670)$ with a standard noniterative process indicating correlation of presumed aerosol with water-leaving radiance (in units of $\mathrm{mW\,cm^{-2}\,\mu m^{-1}\,sr^{-1}}$).

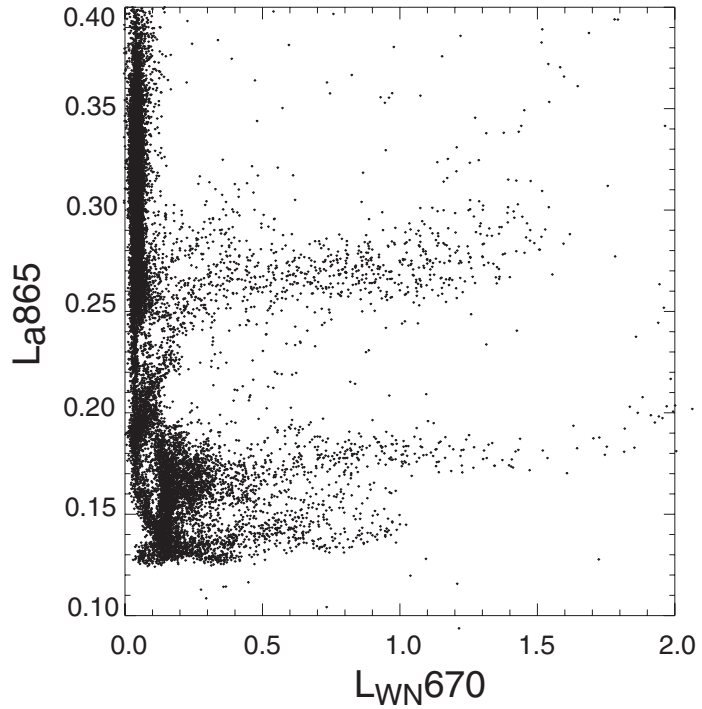

Fig. 37. Comparison of $L_a(865)$ with the NIR iteration, compare with Fig. 38 to show the decrease in correlation between the presumed aerosol and water-leaving radiance (in units of $\mathrm{mW\,cm^{-2}\,\mu m^{-1}\,sr^{-1}}$).

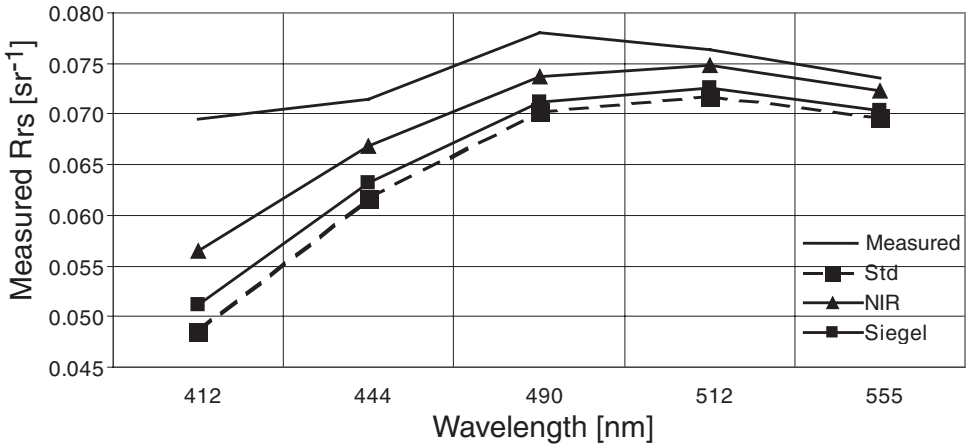

Fig. 38. Mean spectra of noniterative (standard), Siegel iteration, and NIR-iteration methods of processing SeaWiFS data are shown in the station data from the Gulf of Mexico and South Atlantic Bight. The 64 stations were taken over a two-year period.

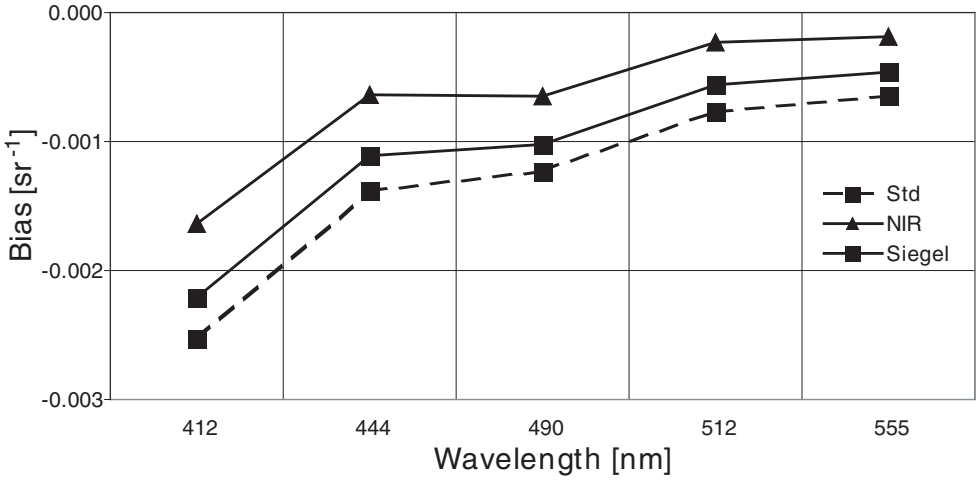

Fig. 39. Bias of SeaWiFS-derived reflectances against measured reflectances taken within one day of overpasses for the noniterative (standard), Siegel iteration, and NIR-iteration methods.

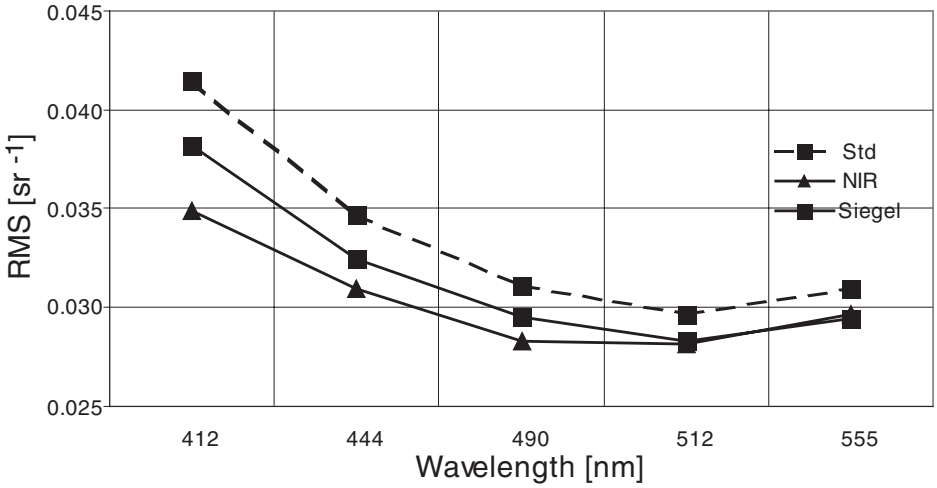

Fig. 40. RMS error between SeaWiFS and field reflectances taken within one day of overpasses for the noniterative (standard), Siegel iteration, and NIR-iteration methods.

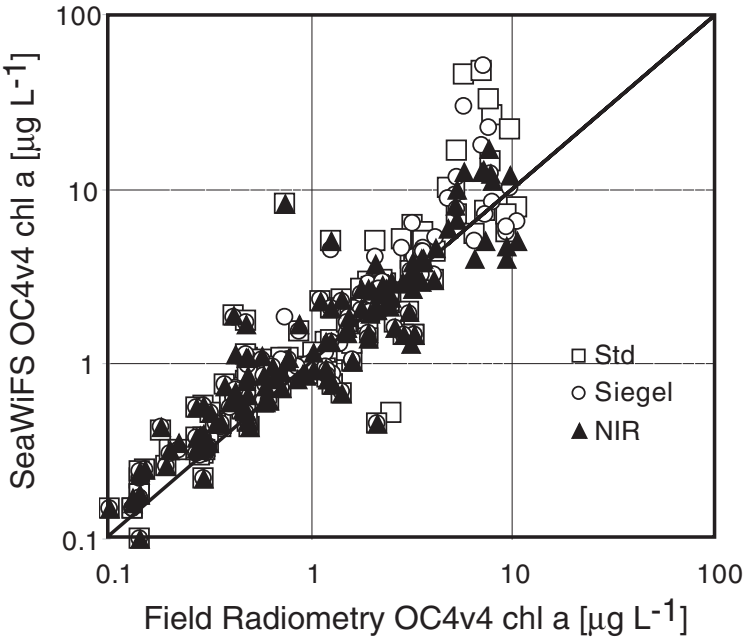

Fig. 41. Comparison of chlorophyll estimated by the Ocean Chlorophyll 4 version 4 algorithm (OC4v4) from satellite- and field matchups for the noniterative (standard), Siegel iteration, and NIR-iteration methods.

40). By improving the aerosol model selection, however, the algorithm results in less error, particularly at shorter wavelengths. As expected, once the scattering effect was removed, the calculated C_a from the OC2 algorithm decreased. The NIR iteration produces a substantial decrease in C_a value in coastal waters. The C_a algorithm is based on the ratio, $R_{\rm rs}(490)/R_{\rm rs}(555)$, and the errors reduce $R_{\rm rs}(490)$ relative to $R_{\rm rs}(555)$. Removing the scattering effect removes this error, bringing the C_a value to reasonable levels.

9.4 CONCLUSIONS

This chapter has described an atmospheric correction procedure that will extend SeaWiFS products into the coastal regions. This procedure provides an improved method of estimating the water-leaving radiance and remote sensing reflectance in turbid coastal waters. This procedure is partially coupled with the Gordon and Wang solution for scattering and molecular absorption and is based on semi-analytic solutions to the spectral behavior of the remote sensing reflectance of the water. This interation presumed a fixed spectral shape of the backscatter, $r_{\rm bb}(\lambda_r, 670)$. In water that is dominated by chlorophyll, this shape may change somewhat.

The full correction described here improves the accuracy of retrieval of remote sensing reflectance, which inherently reduces the number of pixels with unacceptably low reflectances. It will further permit extension of image products into bays and estuaries, however, it will not eliminate all negative radiance. Areas of highly turbid coastal water that produce negative radiances at 555 nm will require additional algorithms to achieve a valid atmospheric correction.

Chapter 10

A Comparison of SeaWiFS LAC Products from the Third and Fourth Reprocessing: Northeast US Ecosystem

John E. O'Reilly
NOAA National Marine Fisheries Service
Narragansett, Rhode Island

James A. Yoder
University of Rhode Island
Narragansett, Rhode Island

Abstract

A comprehensive set of 2,524 LAC scenes of the northeast US continental shelf and adjacent waters scanned by SeaWiFS from 4 September 1997 to 11 November 2002 was processed using NASA standard algorithms and methods employed in the fourth reprocessing. Estimates of chlorophyll *a* concentration (C_a) and normalized water-leaving radiance (L_{WN}) from the fourth reprocessing are statistically compared with results obtained previously from the third reprocessing. Chlorophyll *a* concentration from the fourth reprocessing is lower than those from the third reprocessing in Gulf Stream and Sargasso Sea waters, along the outer continental shelf and slope water, and over the deep basins in the Gulf of Maine. In nearshore shelf waters approximately less than 50 m, C_a from the third and fourth reprocessings are comparable, except over the shoal water on Georges Bank, Nantucket Shoals, and the northern nearshore Gulf of Maine, where C_a from the fourth reprocessing is approximately 1.1–1.2 times greater than C_a from the third reprocessing. The median $L_{WN}(412)$ and median $L_{WN}(443)$ from the fourth reprocessing are substantially greater than values from the third reprocessing, and the frequency of negative water-leaving radiances for the 412 nm and 443 nm bands is significantly lower with the fourth reprocessing. Statistical match-up comparisons between SeaWiFS C_a and *in situ* C_a indicate that the fourth reprocessing improved the accuracy of C_a estimates for this region.

10.1 INTRODUCTION

Previous chapters in this volume describe a number of improvements to the SeaWiFS algorithms and processing methods that were incorporated into the fourth reprocessing, with a focus on results from the global ocean. This chapter focuses on high resolution SeaWiFS LAC scenes of the northeast US coastal ecosystem, comparing results from the third and fourth reprocessing.

The northeast US coastal ecosystem (NEC) is a good representative area for studying changes in SeaWiFS LAC products resulting from changes in algorithms and data processing methods. This study area (Fig. 42) encompasses several large eutrophic estuaries, highly productive continental shelf water (O'Reilly and Zetlin 1998), and oligotrophic blue waters of the Gulf Stream and Sargasso Sea. SeaWiFS estimates of surface chlorophyll concentration (C_a) in this area span over three orders of magnitude, with most (99.8%) from 0.02–30 mg m^{-3} (Table 10). This region encompasses a wide range of bio-optical conditions (Case-1 and -2 waters), capturing all but the clearest, most oligotrophic waters (0.001–0.02 mg m^{-3} C_a) scanned by SeaWiFS. Moreover, this and other regions adjacent to densely populated and industrialized areas present formidable challenges to the atmospheric correction of ocean color data and the derivation of accurate water-leaving radiances that are required for reliable C_a estimates.

10.2 METHODS

These analyses are based on 2,524 SeaWiFS LAC scenes covering the NEC region and the period from 4 September 1997 through 11 November 2002. Level-1 SeaWiFS data were obtained from the NASA DAAC and processed to level-2 using SeaDAS (Fu et al. 1998). Level-2 processing employed the NASA standard algorithms and standard (default) SeaDAS processing parameters used in the third and fourth reprocessings (McClain 2000, and Chapt. 1 of

Table 10. Statistical characteristics of SeaWiFS products from the third and fourth reprocessing. Values in the "0.1%" and "99.9%" columns represent the 0.1 and 99.9 percentiles. The percent of data below zero is indicated by P_{neg}. The statistics are based on clear pixels (third reprocessing: 3.07×10^8; fourth reprocessing: 3.52×10^8) present in 2,524 SeaWiFS NEC scenes.

	Third Reprocessing					*Fourth Reprocessing*				
Product	0.1%	99.9%	Median	Mode	P_{neg}	0.1%	99.9%	Median	Mode	P_{neg}
Chlorophyll *a*	0.034	35.75	0.593	0.114	N/A	0.019	29.70	0.441	0.097	N/A
$L_{WN}(412)$	−1.451	2.774	0.351	0.093	25.04	−1.425	3.167	0.549	0.207	14.19
$L_{WN}(443)$	−0.837	2.667	0.603	0.341	6.972	−0.867	2.898	0.689	0.378	5.057
$L_{WN}(490)$	−0.199	2.136	0.722	0.567	0.846	−0.308	2.539	0.774	0.565	0.551
$L_{WN}(510)$	0.022	2.185	0.619	0.608	0.604	−0.045	2.679	0.599	0.588	0.175
$L_{WN}(555)$	0.146	2.644	0.380	0.331	0.522	0.152	3.136	0.364	0.310	0.018
$L_{WN}(670)$	−0.104	1.225	0.047	0.038	7.618	−0.134	1.585	0.041	0.032	10.63
$\tau_a(510)$	0.007	0.571	0.105	0.056	0.529	0.005	0.599	0.111	0.061	0.150
$\tau_a(865)$	0.006	0.337	0.078	0.049	0.522	0.004	0.342	0.077	0.043	0.149
$\alpha(510)$	−0.096	1.483	0.475	0.500	N/A	−0.084	1.483	0.657	0.641	N/A
PAR						0.578	62.53	30.38	61.34	N/A

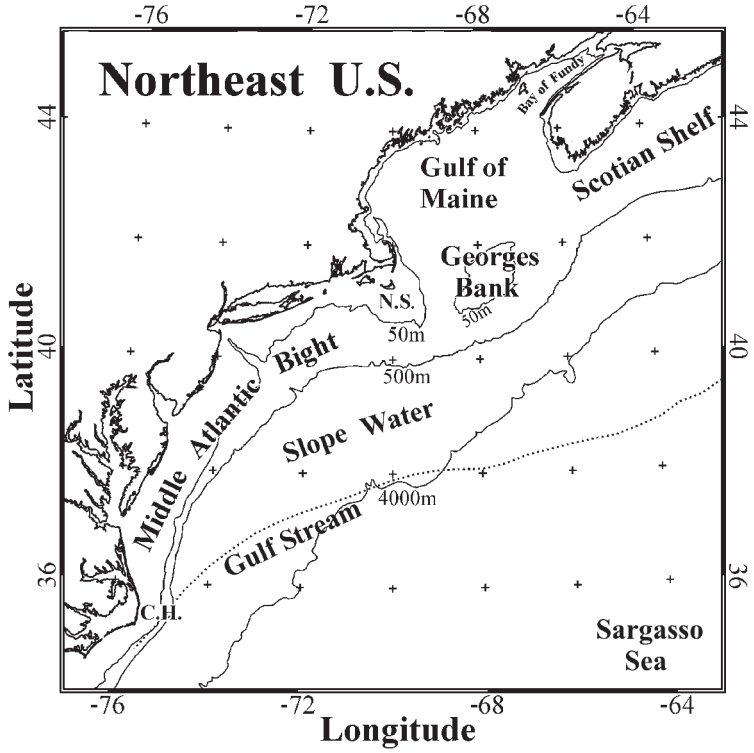

Fig. 42. The study area and its major oceanographic regions: Middle Atlantic Bight, Georges Bank, Gulf of Maine, Scotian Shelf, Bay of Fundy, Slope Water, Gulf Stream, and the Sargasso Sea. In addition, Cape Hatteras (C.H.), Nantucket Shoals (N.S.), and the locations of the 50 m, 500 m, and 4,000 m isobaths are shown. The mean position of the north wall of the Gulf Stream is illustrated as a dashed line intersecting the 4,000 m isobath.

this volume, respectively). Scenes collected before 15:30 GMT and after 18:40 GMT were discarded, leaving from 2–3 scenes each day with some coverage of the NEC region. HRPT stations represented in the final data set included 2,496 from the NASA Goddard Space Flight Center, 22 from the Bedford Institute of Oceanography, and 6 from the Bermuda Biological Station. SeaDAS (version 4.3) was also used to map level-2 data to the standard Lambert conic projection (1024×1024 pixels with a resolution of 1.25 km per pixel).

A number of SeaWiFS products were generated with SeaDAS:

a) OC4v4 chlorophyll *a* concentration;

b) Normalized water-leaving radiance for six bands, i.e., $L_{WN}(412)$, $L_{WN}(443)$, $L_{WN}(490)$, $L_{WN}(510)$, $L_{WN}(555)$, and $L_{WN}(670)$;

c) Aerosol optical depth at 510 nm, i.e., $\tau_a(510)$, and 865 nm, i.e., $\tau_a(865)$;

d) Aerosol Ångström coefficient at 510 nm, $\alpha(510)$;

e) PAR; and

f) Level-2 processing flags, `L2` flags.

The `L2` flags used to mask (i.e., eliminate) data from statistical analyses of all products except PAR were `land`, `sunglint`, `highlt`, `straylight`, `cldice`, `solzen`, and `lowlw`.

SeaWiFS C_a estimates were compared (i.e., matchups) with *in situ* C_a measured in surface water collected during surveys of the continental shelf region conducted by the National Oceanic and Atmospheric Administration (NOAA) National Marine Fisheries Service (NMFS). In these matchups, SeaWiFS C_a was represented as the median of retrievals from a 7×7 pixel box centered over the *in situ* sampling coordinates, with at least 11 clear pixels, and within ±12 hr of the *in situ* observation. The *in situ* C_a measurements were made at sea on 90% acetone extracts of pigments from surface (2 m) water samples using the Welschmeyer (1994) fluorometric method and a Turner Designs model 10 AU digital fluorometer fitted with nonacidification optical filters and a lamp kit. The fluorometer was calibrated with Turner Designs certified fluorometric chlorophyll standard (19.6 $\mu g\,L^{-1}\,C_a$). Measurements of fluorescence of a secondary standard—Turner Designs' red solid secondary standard for chlorophyll *a*—were also made with each sample reading to correct for minor variations in fluorometer sensitivity during surveys. Matchups were statistically evaluated by using a Type II linear regression (Press and Teukolsky 1992) of $\log_{10}$-transformed data.

10.3 RESULTS

The relative and cumulative frequency distributions for C_a and L_{WN} values from the third and fourth reprocessings are illustrated in Fig. 43. Table 10 summarizes the statistical characteristics of these frequency distributions. The fourth reprocessing yielded more clear pixels (3.52×10^8) than the third reprocessing (3.07×10^8), with the same number of scenes and `L2` flags applied to eliminate suspect data. This increase is related to the changes of the flags and masks that increased the number of valid pixels with the fourth reprocessing (Chapt. 6).

10.3.1 C_a

When considering the entire region, the median C_a from the fourth reprocessing (0.441 mg m^{-3}) is lower than that from the third reprocessing (0.593 mg m^{-3}). A similar decrease in the mode and the 0.1 and 99.9 percentiles is also evident (Table 10). The relative frequency distribution for C_a from the fourth reprocessing (Fig. 43b) is smoother and has a more log-normal shape than the distribution from the third reprocessing (Fig. 43a).

The spatial distribution of the ratio of C_a (from the fourth to the third reprocessings) is portrayed in Fig. 44. In continental shelf waters shallower than 50 m, estimates of C_a from the third and fourth reprocessings are comparable, except along the Maine coast, Nantucket Shoals, and the tidally mixed shoal water on Georges Bank, where C_a from the fourth reprocessing is approximately 1.1–1.2 times greater than C_a from the third reprocessing.

In areas of usually low C_a, such as the slope water, Gulf Stream, and Sargasso Sea (Fig. 45), the mean C_a from the fourth reprocessing is lower (0.8) than the mean C_a from the third reprocessing. In the turbid, chlorophyll-rich areas within the Middle Atlantic Bight estuaries and the Bay of Fundy, C_a from the fourth reprocessing tends to be lower than C_a from the third reprocessing.

10.3.2 Normalized Water-Leaving Radiances

The median $L_{WN}(412)$ from the fourth reprocessing was substantially greater than that from the third reprocessing (Table 10; Fig. 43). The median values for both $L_{WN}(443)$ and $L_{WN}(490)$ also increased, while medians for $L_{WN}(510)$, $L_{WN}(555)$, and $L_{WN}(670)$ decreased. The percent frequency of pixels with negative water-leaving radiances ($P_{\rm neg}$) for the 412 nm band was substantially lower in data from the fourth reprocessing (14%) than from the third reprocessing (25%). In a similar manner, $P_{\rm neg}(443)$, $P_{\rm neg}(490)$, $P_{\rm neg}(510)$, and $P_{\rm neg}(555)$ decreased from the third to the fourth reprocessing whereas $P_{\rm neg}(670)$ increased from 7.6–10.7% (Table 10).

The spatial distributions of $P_{\rm neg}(412)$ and $P_{\rm neg}(443)$ are shown in Fig. 46. The general pattern of $P_{\rm neg}$ is correlated with the pattern for the mean C_a, with the highest $P_{\rm neg}$ in the nearshore and estuarine areas and the lowest $P_{\rm neg}$ in offshore waters (compare Fig. 45 with Fig. 46). The $P_{\rm neg}(412)$ above 50% from the fourth reprocessing is restricted to a narrow band adjacent to the coast, whereas $P_{\rm neg}(412)$ from the third reprocessing exceeded 50% over most of the inner half of the continental shelf area.

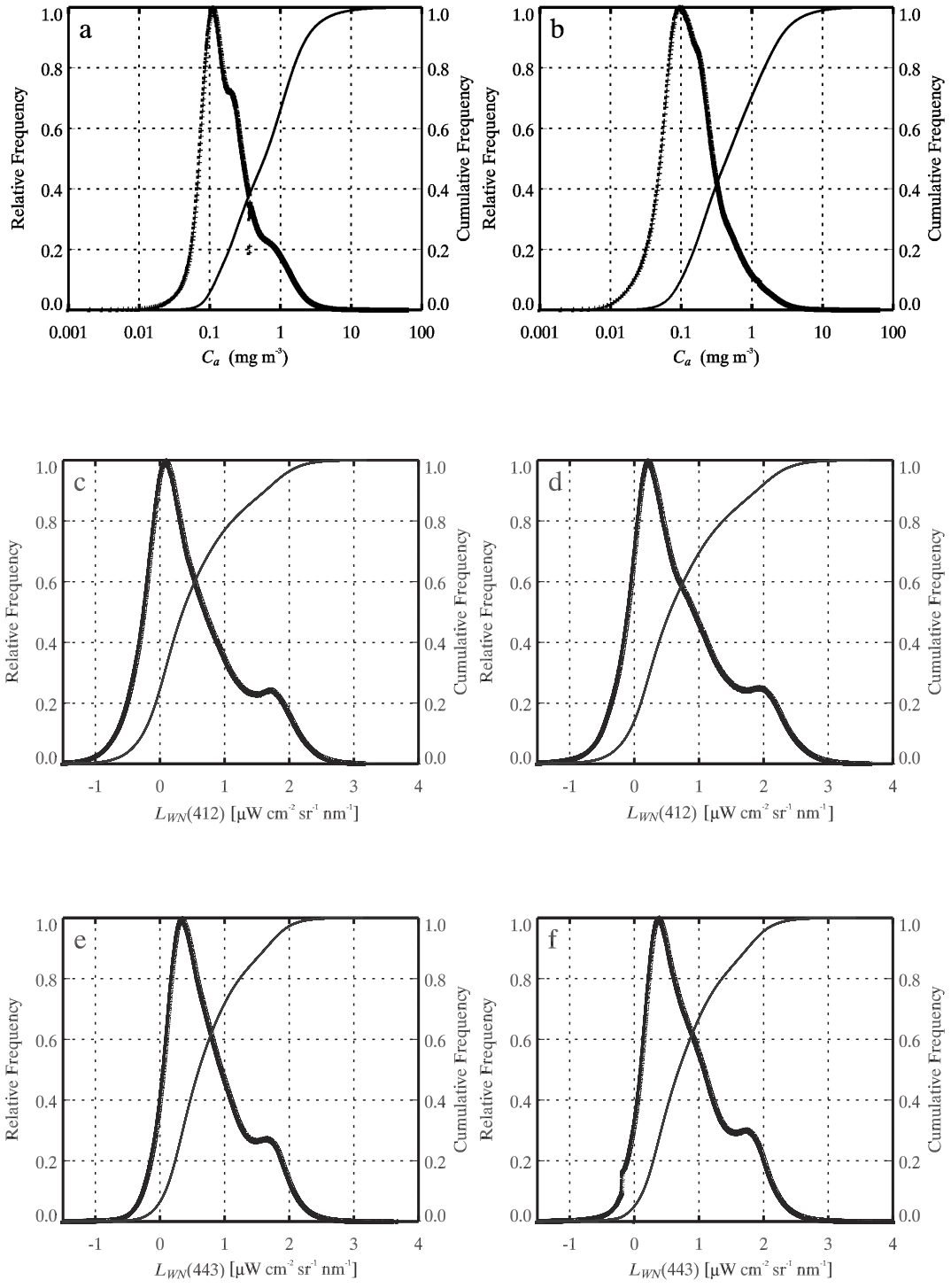

Fig. 43. The frequency distributions for SeaWiFS data from the third and fourth reprocessing. The relative frequency distribution (thick curve) and cumulative frequency distribution (thin curve) are shown in each panel: **a)** C_a, third reprocessing; **b)** C_a, fourth reprocessing; **c)** $L_{WN}(412)$, third reprocessing; **d)** $L_{WN}(412)$, fourth reprocessing; **e)** $L_{WN}(443)$, third reprocessing; and **f)** $L_{WN}(443)$, fourth reprocessing.

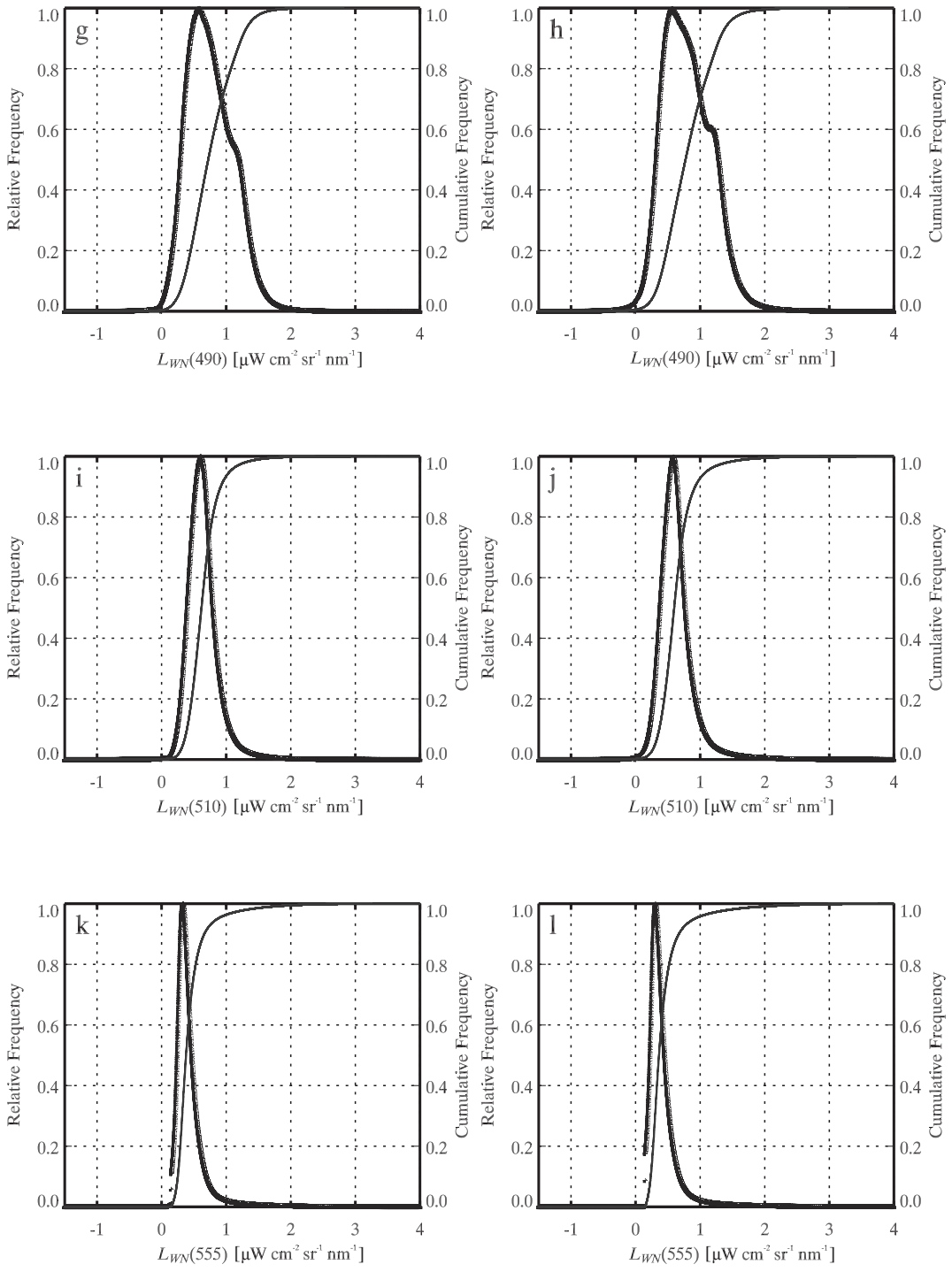

Fig. 43. (cont.) The frequency distributions for SeaWiFS data from the third and fourth reprocessing. The relative frequency distribution (thick curve) and cumulative frequency distribution (thin curve) are shown in each panel: **g)** $L_{WN}(490)$, third reprocessing; **h)** $L_{WN}(490)$, fourth reprocessing; **i)** $L_{WN}(510)$, third reprocessing; **j)** $L_{WN}(510)$, fourth reprocessing; **k)** $L_{WN}(555)$, third reprocessing; and **l)** $L_{WN}(555)$, fourth reprocessing.

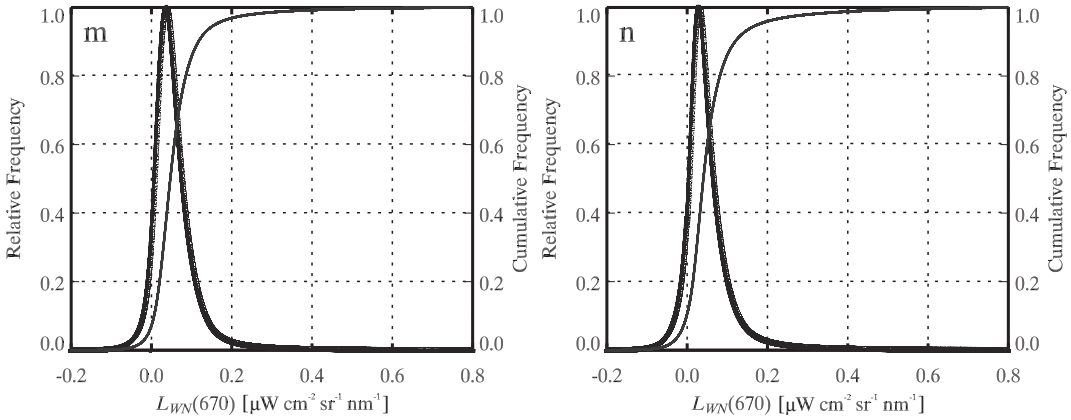

Fig. 43. (cont.) The frequency distributions for SeaWiFS data from the third and fourth reprocessing. The relative frequency distribution (thick curve) and cumulative frequency distribution (thin curve) are shown in each panel: **m)** $L_{WN}(670)$, third reprocessing; and **n)** $L_{WN}(670)$, fourth reprocessing.

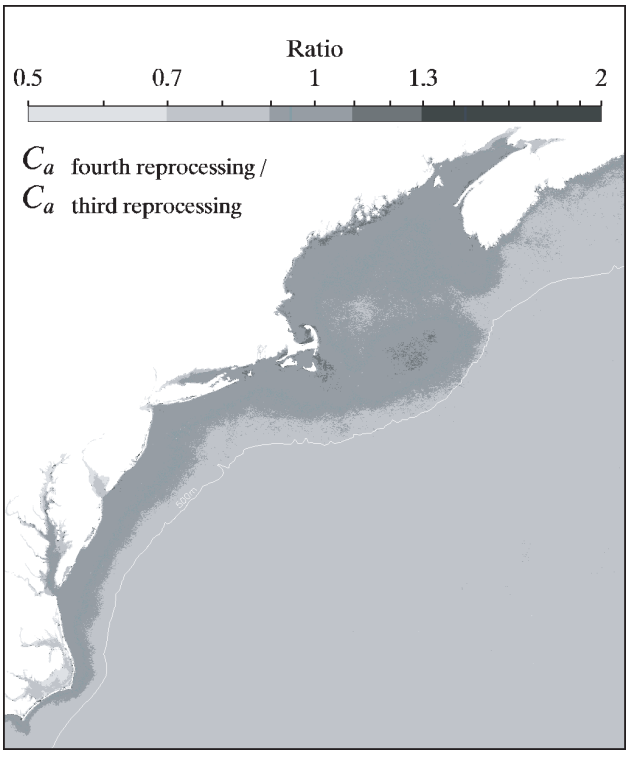

Fig. 44. The spatial distribution of the ratio of mean C_a from the fourth reprocessing to mean C_a from the third reprocessing. The 500 m isobath is represented as a white line.

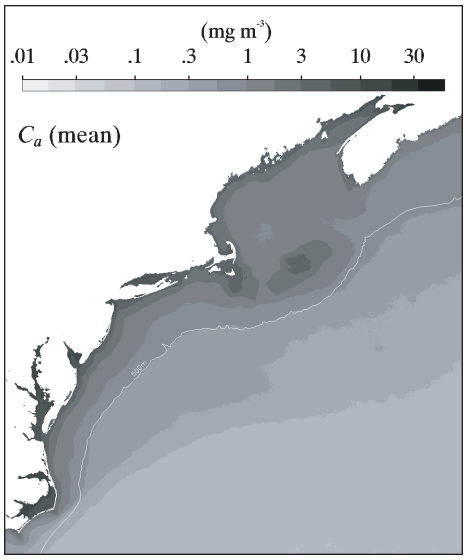

Fig. 45. The spatial distribution of the mean SeaWiFS C_a from the fourth reprocessing. The mean C_a is a geometric mean based on 2,524 SeaWiFS LAC scenes from 4 September 1997 to 11 November 2002. The 500 m isobath is represented as a white line.

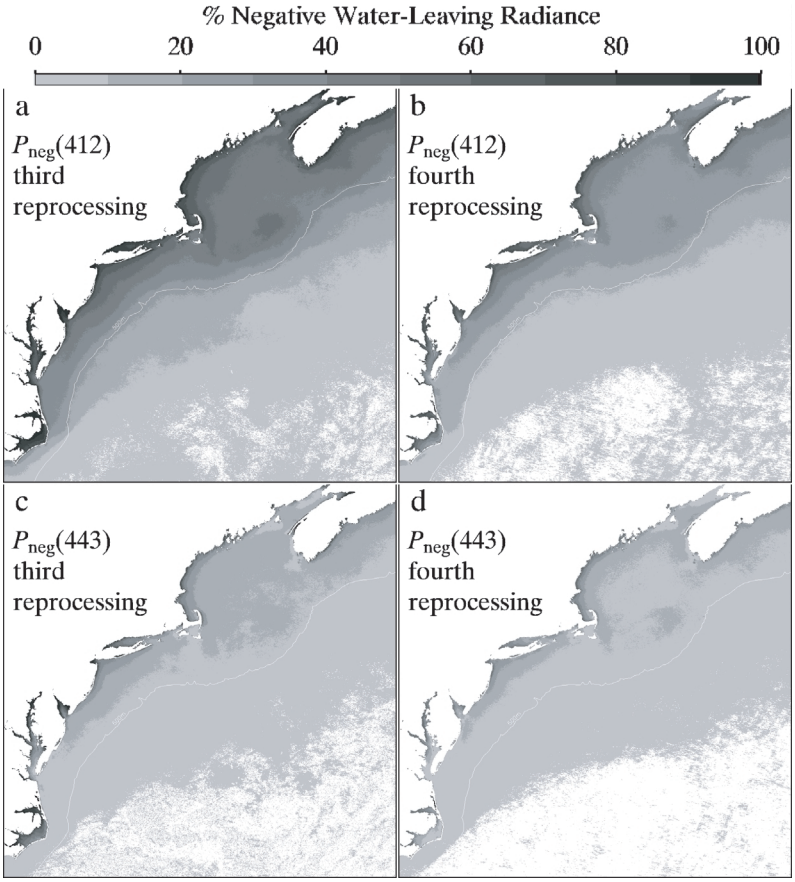

Fig. 46. The spatial distribution of the frequency of negative water-leaving radiance retrievals (P_{neg}): **a)** $P_{\text{neg}}(412)$, third reprocessing; **b)** $P_{\text{neg}}(412)$, fourth reprocessing; **c)** $P_{\text{neg}}(443)$, third reprocessing; and **d)** $P_{\text{neg}}(443)$, fourth reprocessing. Ocean areas where no negative water-leaving radiances were detected are designated as white (e.g., portions of the Gulf Stream and Sargasso Sea regions). The P_{neg} value is based on the clear pixel retrievals in 2,524 SeaWiFS LAC scenes. The 500 m isobath is represented as a white line.

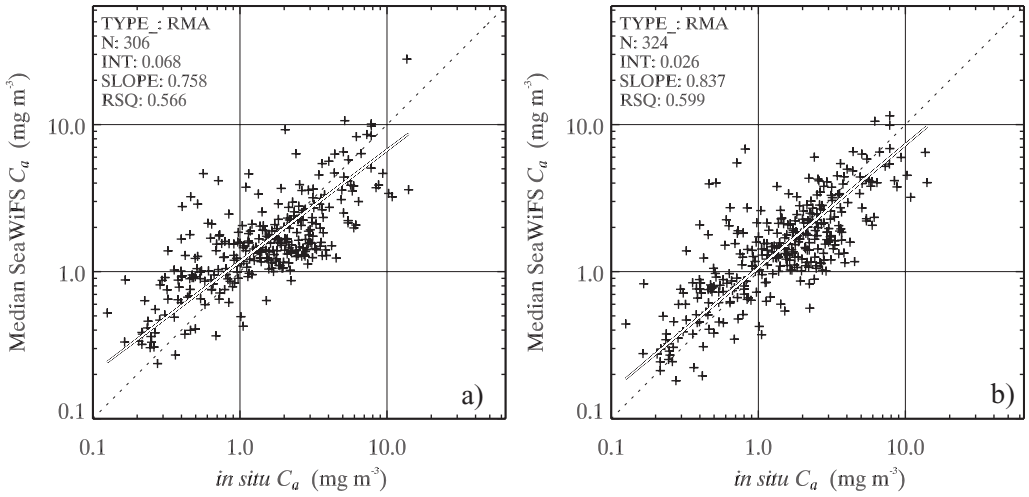

Fig. 47. Reduced Major Axis (RMA) regression of SeaWiFS C_a with *in situ* C_a: **a)** matchup results from the third reprocessing; and **b)** matchup results for data from the fourth reprocessing. The number of matchups (N), regression intercept (INT), regression slope (SLOPE), R^2 coefficient of determination (RSQ), and the regression line are shown in each plot. The dashed line represents a 1:1 relationship.

10.3.3 Matchups

The statistical results for the space–time matchups between SeaWiFS and *in situ* C_a (Fig. 47) indicate that the accuracy of SeaWiFS C_a from the fourth reprocessing is superior to that from the third reprocessing (the regression slope is closer to 1.0, and the intercept is closer to 0.0). The coefficient of determination (R^2) also improved from 0.566 to 0.599 (Fig. 47). Note that the fourth reprocessing yielded more matchups than the third, using identical match-up criteria and SeaDAS masking flags, because more clear pixels were retrieved (Table 10).

10.4 CONCLUSIONS

The suite of improvements to algorithms and processing methods incorporated into the fourth reprocessing have markedly improved the accuracy of SeaWiFS LAC estimates of C_a and water-leaving radiances for this region, relative to results from the third reprocessing. The use of stray light corrected MOBY data in the vicarious calibration (Chapt. 3) and other modifications, have resulted in substantial decreases in the frequency of negative water-leaving radiances for the 412 nm and 443 nm bands. Despite these improvements, the fourth reprocessing still produced relatively high $P_{\rm neg}(412)$ (>20%) and $P_{\rm neg}(443)$ (>10%) throughout a large portion of the continental shelf area. The occurrence of negative L_{WN} values is an obvious symptom of inadequate atmospheric correction. Further improvements in atmospheric correction schemes are required, particularly in the nearshore areas, and such improvements will likely further improve the accuracy of SeaWiFS estimates of C_a for this region.

Acknowledgments

The authors wish to thank T. Ducas, S. Schollaert, and M. Kennelly for their assistance in processing SeaWiFS data, J. Prezioso, J. Dennecour, and J. Jossi for their assistance with *in situ* chlorophyll measurements, and J. Acker and the Goddard DAAC for providing SeaWiFS data and assistance.

Glossary

ACS Attitude Control System
AOT Aerosol Optical Thickness

BBOP Bermuda BioOptics Project

CVT Calibration and Validation Team
CZCS Coastal Zone Color Scanner

DAAC Distributed Active Archive Center

ETOPO2 Earth Topography 2 min grid
ETOPO5 Earth Topography 5 min grid

GAC Global Area Coverage (SeaWiFS 1 km resolution, subsampled to 4 km)
GPS Global Positioning System
GSFC Goddard Space Flight Center

HRPT High Resolution Picture Transmission

LAC Local Area Coverage (SeaWiFS 1 km resolution)

MERIS Medium Resolution Imaging Spectrometer
MOBY Marine Optical Buoy
MODIS Moderate Resolution Imaging Spectroradiometer

NASA National Aeronautics and Space Administration
NDVI Normalized Difference Vegetation Index
NEC Northeast US Coastal Ecosystem
NIR Near-Infrared
NIST National Institute of Standards and Technology

OCTS Ocean Color and Temperature Scanner
OrbView-2 Not an acronym, but the current name for the SeaStar satellite.

PAR Photosynthetically Available Radiation

QC Quality Control

RMA Reduced Major Axis
RMS Root Mean Squared
ROLO Robotic Lunar Observatory
RSR Relative Spectral Response

SBRS Santa Barbara Research Systems
SeaDAS SeaWiFS Data Analysis System
SeaWiFS Sea-viewing Wide Field-of-view Sensor
SIMBIOS Sensor Intercomparison and Merger for Biological and Interdisciplinary Oceanic Studies
SIRCUS Spectral Irradiance and Radiance Responsitivity Calibrations Using Uniform Standards

TOA Top of the Atmosphere

USGS United States Geological Survey
UTC Coordinated Universal Time

Symbols

a_0 Coefficient of the lunar calibration function of time.
a_1 Coefficient of the lunar calibration function of time.
a_2 Coefficient of the lunar calibration function of time.
a_{dg} Absorption coefficient for detritus and gelbstoff.
a_{oz} Ozone absorption coefficient.
a_p Absorption coefficient for particles.
a_{ph} Absorption coefficient for phytoplankton.
a_{tot} Total absorption coefficient, the sum of a_{dg}, a_p, and a_w.
a_w Absorption coefficient for water.
A Cloud–surface system albedo.
A_s Albedo of the ocean surface.

b Scattering function.
b_b Backscatter coefficient.
b_{bp} Particulate backscatter coefficient.
b_{wv} Pure water backscatter coefficient.

C_a Chlorophyll a concentration.
C_{oz} Ozone concentration.

d_a Distance of aerosol model.

E_0 Solar flux at the top of the atmosphere.
E_c Solar flux that would reach the surface if the cloud–surface system were nonreflecting and nonabsorbing.
E_s Solar flux reaching the ocean surface.
$\bar{E}_s$ Estimate of daily PAR.
E_u Upwelling radiance.
$\bar{E}_\theta$ Mean extraterrestrial solar irradiance.

f Lunar calibration function of time.
f_T Detector temperature correction.
f/Q Bidirectional reflectance at the water's surface.
F Dependence of the cloud–surface system albedo on solar zenith angle.
F_0 Solar irradiance.

G_i Gain for a given band.

i An index variable for either a given pixel, band, or number of iterations.
i_c Centered pixel i.

j An index variable for a given band.

k SeaWiFS aerosol model indicator.
K_2 Detector temperature correction factor.
$K_d(490)$ Diffuse attenuation coefficient at 490 nm.

l_1 SeaWiFS aerosol model indicator.
$L(\lambda_M)$ The L_{WN} values for MOBY.
$L(\lambda_S)$ The L_{WN} values for SeaWiFS.
$L(\lambda_{S/M})$ $L(\lambda_S)$ averaged over the 5×5 pixel subscene and this average value is divided by $L(\lambda_M)$.
$L_a(\lambda, i)$ Aerosol path radiance, including Rayleigh-aerosol interaction for wavelength λ at location i.
$L'_a(\lambda, i)$ The computed aerosol path radiance, including Rayleigh-aerosol interaction for wavelength λ at location i.
$L_r(\lambda, i)$ Rayleigh path radiance for wavelength λ at location i.
L_{ra} Interaction between molecular and aerosal scattering radiance.
L_t Radiance at the top of the atmosphere.
$L_t(\lambda, i)$ Observed TOA radiance for wavelength λ at location i.
L_u Upwelling radiance.
L_W Water-leaving radiance.
$L_{WN}(\lambda)$ Normalized water-leaving radiance at wavelength λ.
$L_{WN}(\lambda_r)$ Normalized water-leaving radiance in the NIR part of the spectrum.
L'_{WN} Corrected normalized water-leaving radiance.
$L_{WN}(0^-)$ Normalized water-leaving radiance, just below the sea surface.
$L_{WN}(0^+)$ Normalized water-leaving radiance, just above the sea surface.

n_w Refractive index of the water.
N Number of matchups.

P_a Aerosol phase function.
P_m Molecular phase function.
$P_{\rm neg}(\lambda)$ Percent frequency of pixels with negative water-leaving radiances.

Q The factor E_u/L_u.

$r_{\rm bb}$ Backscatter relationship.
R^2 Coefficient of determination.
$R_{\rm rs}(\lambda)$ Remote-sensing reflectance at wavelength λ.

S_a Spherical albedo.

t Time.
$t(\lambda)$ Diffuse transmittance.
t_d Clear sky total (diffuse + direct) transmittance.
$t_f(\theta)$ Fresnel transmittance of the air–sea interface.
t_g Gaseous transmittance.
$tL_f(\lambda, i)$ White-cap radiance, transmitted to the TOA for wavelength λ at location i.
$t_{\rm ox}(\lambda, i)$ Oxygen transmittance for wavelength λ at location i.
$t_{\rm oz}$ Gaseous transmittance due to ozone.
$t_{\rm oz}(\lambda, i)$ Ozone transmittance for wavelength λ at location i.
$t_{\rm wv}$ Gaseous transmittance due to water vapor.
t_0 Reference time for lunar calibration time series.
T Detector temperature.
$T(\lambda)$ Direct transmittance.
T_d Clear sky direct transmittance.
$T_{\rm ref}$ Detector reference temperature.
T_w Transmission and refraction loss at the air–water interface.

X See (46).

y The l_1 value from Gordon et al. (1988) times Q.

α Ångström coefficient.

ϵ Single-scattering aerosol reflectance ratio.
$\epsilon_{\rm ms}$ Multiscattering equivalent of ϵ.

η Constant.

θ Sensor zenith angle.
θ_0 Solar zenith angle.
θ_v Viewing zenith angle.

λ Wavelength.
λ_i Nominal wavelength for band i.
$\lambda_{i/j}$ Radiance ratio of band i to band j.
λ_j Reference band wavelength.
λ_M The L_{WN} values for MOBY.
λ_r The NIR part of the spectrum.
λ_S The L_{WN} values for SeaWiFS.
$\lambda_{S/M}$ Mean of the SeaWiFS and MOBY L_{WN} values.
λ_v Wavelength in the visible part of the spectrum.

ρ_a Aerosol path reflectance at wavelength λ.
$\rho_{\rm atm}$ Reflectance due to scattering by molecules and aerosols in the atmosphere.
ρ_s Reflectance of the cloud–surface layer.
ρ_t Reflectance at the top of the atmosphere.
ρ_t' Corrected ρ_t for gaseous absorption due to ozone.

τ_a Aerosol optical thickness.
τ_m Optical thickness of molecules.

ω_a Single scattering albedo of aerosols.

References

Ainsworth, E.J., and F.S. Patt, 2000: "Modifications to the TOMS ozone ancillary data interpolation." In: McClain, C.R., E.J. Ainsworth, R.A. Barnes, R.E. Eplee, Jr., F.S. Patt, W.D. Robinson, M. Wang, and S.W. Bailey, SeaWiFS Postlaunch Calibration and Validation Analyses, Part 1. *NASA Tech. Memo. 2000–206892, Vol. 9,* S.B. Hooker and E.R. Firestone, Eds., NASA Goddard Space Flight Center, Greenbelt, Maryland, 69–73.

Bailey, S.W., C.R. McClain, P.J. Werdell, and B.D. Schieber, 2000: "Normalized water-leaving radiance and chlorophyll *a* match-up analyses." In: McClain, C.R., R.A. Barnes, R.E. Eplee, Jr., B.A. Franz, N.C. Hsu, F.S. Patt, C.M. Pietras, W.D. Robinson, B.D. Schieber, G.M. Schmidt, M. Wang, S.W. Bailey, and P.J. Werdell, SeaWiFS Postlaunch Calibration and Validation Analyses, Part 2. *NASA Tech. Memo. 2000–206892, Vol. 10,* S.B. Hooker and E.R. Firestone, Eds., NASA Goddard Space Flight Center, Greenbelt, Maryland, 45–52.

Barnes, R.A., A.W. Holmes, W.L. Barnes, W.E. Esaias, C.R. McClain, and T. Svitek, 1994: SeaWiFS Prelaunch Radiometric Calibration and Spectral Characterization. *NASA Tech. Memo. 104566, Vol. 23,* S.B. Hooker, E.R. Firestone, and J.G. Acker, Eds., NASA Goddard Space Flight Center, Greenbelt, Maryland, 55 pp.

——, ——, and W.E. Esaias, 1995: Stray Light in the SeaWiFS Radiometer. *NASA Tech. Memo. 104566, Vol. 31,* S.B. Hooker, E.R. Firestone, and J.G. Acker, Eds., NASA Goddard Space Flight Center, Greenbelt, Maryland, 76 pp.

——, R.E. Eplee, Jr., G.M. Schmidt, F.S. Patt, and C.R. McClain, 2001: Calibration of SeaWiFS. I. Direct techniques. *Appl. Opt.,* **40,** 6,682–6,700.

Bricaud, A., A. Morel, M. Babin, K. Allali, and H. Claustre, 1998: Variations of light absorption by suspended particles with chlorophyll *a* concentration in oceanic (Case-1) waters: Analysis and implications for bio-optical models. *J. Geophys. Res.,* **103,** 31,033–31,044.

Briegleb, B.P., and V. Ramanathan, 1982: Spectral and diurnal variations in clear sky planetary albedo. *J. Climate Appl. Meteor.,* **21,** 1,168–1,171.

Carder, K.L., F.R. Chen, Z.P. Lee, and S.K. Hawes, 1999: Semi-analytic Moderate-Resolution Imaging Spectrometer algorithms for chlorophyll *a* and absorption with bio-optical domains based on nitrate-depletion temperatures. *J. Geophys. Res.,* **104,** 5,403–5,421.

Clark, D.K., M.E. Feinholz, M.A. Yarbrough, B.C. Johnson, S.W. Brown, Y.S. Kim, and R.A. Barnes, 2001: "Overview of the radiometric calibration of MOBY." In: Earth Observing Systems VI, *SPIE,* **4483,** 64–76.

Curcio, J.A., and C.C. Petty, 1951: The near infrared absorption spectrum of liquid water. *J. Opt. Soc. Amer.,* **41,** 302–305.

Dedieu, G., P.-Y. Deschamps, and Y.H. Kerr, 1987: Satellite estimation of solar irradiance at the surface of the earth and of surface albedo using a physical model applied to Meteosat data. *J. Climate Appl. Meteor.,* **26,** 79–87.

Eplee, R.E., Jr., and R.A. Barnes, 2000: "Lunar data analysis for SeaWiFS calibration." In: McClain, C.R., E.J. Ainsworth, R.A. Barnes, R.E. Eplee, Jr., F.S. Patt, W.D. Robinson, M. Wang, and S.W. Bailey, SeaWiFS Postlaunch Calibration and Validation Analyses, Part 1. *NASA Tech. Memo. 2000–206892, Vol. 9,* S.B. Hooker and E.R. Firestone, Eds., NASA Goddard Space Flight Center, Greenbelt, Maryland, 17–27.

——, and C.R. McClain, 2000: "MOBY data analysis for the vicarious calibration of SeaWiFS bands 1–6." In: McClain, C.R., E.J. Ainsworth, R.A. Barnes, R.E. Eplee, Jr., F.S. Patt, W.D. Robinson, M. Wang, and S.W. Bailey, 2000: SeaWiFS Postlaunch Calibration and Validation Analyses, Part 1. *NASA Tech. Memo. 2000–206892, Vol. 9,* S.B. Hooker and E.R. Firestone, Eds., NASA Goddard Space Flight Center, Greenbelt, Maryland, 43–50.

——, W.D. Robinson, S.W. Bailey, D.K. Clark, P.J. Werdell, M. Wang, R.A. Barnes, and C.R. McClain, 2001: Calibration of SeaWiFS. II. Vicarious techniques. *Appl. Opt.,* **40,** 6,701–6,718.

Frouin, R., D.W. Lingner, K. Baker, C. Gautier, and R. Smith, 1989: A simple analytical formula to compute clear sky total and photosynthetically available solar irradiance at the ocean surface. *J. Geophys. Res.,* **94,** 9,731–9,742.

——, and B. Chertock, 1992: A technique for global monitoring of net solar irradiance at the ocean surface. Part I: Model. *J. Appl. Meteor.,* **31,** 1,056–1,066.

Fu, G., K.S. Baith, and C.R. McClain, 1998: SeaDAS: The SeaWiFS Data Analysis System. *Proc. 4th Pacific Ocean Remote Sensing Conf.,* Qingdao, China, 28–31 July 1998, 73–79.

Gordon, H.R., 1995: Remote sensing of ocean color: a methodology for dealing with broad spectral bands and significant out-of-band response. *Appl. Opt.,* **34,** 8,363–8,374.

——, and D.K. Clark, 1981: Clear water radiances for atmospheric correction of coastal zone color scanner imagery. *Appl. Opt.,* **20,** 4,175–4,180.

——, ——, J.W. Brown, O.B. Brown, R.H. Evans, and W.W. Broenkow, 1983: Phytoplankton pigment concentrations in the Middle Atlantic bight: comparison between ship determinations and Coastal Zone Color Scanner estimates. *Appl. Opt.,* **22,** 20–26.

——, O.B. Brown, R.H. Evans, J.W. Brown, R.C. Smith, K.S. Baker, and D.K. Clark, 1988: A semianalytic radiance model of ocean color. *J. Geophys. Res.,* **93,** 10,909–10,924.

——, and M. Wang, 1994: Retrieval of water-leaving radiance and aerosol optical thickness over the oceans with SeaWiFS: a preliminary algorithm. *Appl. Opt.,* **33,** 443–452.

Gould, R.W., and R.A. Arnone, 1994: Extending Coastal Zone Color Scanner estimates of the diffuse attenuation coefficient into case II waters. *SPIE, Ocean Optics XII,* **2258,** 342–356.

——, ——, and M. Sydor, 1998: Testing a new remote sensing reflectance algorithm to estimate absorption and scattering in Case-2 Waters. [Available on CD-ROM], *SPIE Ocean Optics XII,* Hawaii.

——, ——, and P.M. Martinolich, 1999: Spectral dependence of the scattering coefficient in Case-1 and Case-2 waters. *Appl. Opt.,* **38,** 2,377–2,383.

Hale, G.M., and M.R. Query, 1973: Optical constants of water in the 200-nm to 200μm wavelength region. *Appl. Opt.,* **12,** 555–563.

Hu, C., K.L. Carder, and F.E. Müeller-Karger, 2000a: How precise are SeaWiFS ocean color estimates? Implications of digital noise errors. *Remote Sens. Environ.,* **76,** 239–249.

——, ——, and ——, 2000b: Atmospheric correction of SeaWiFS imagery over turbid coastal waters; a practical method. *Remote Sens. Environ.,* **74,** 195–206.

Kieffer, H.H., T.C. Stone, R.A. Barnes, S. Bender, R.E. Eplee, Jr., J. Mendenhall, and L. Ong, 2002: "On-orbit radiometric calibration over time and between spacecraft using the Moon." In: Sensors, Systems, and Next Generation Satellites VIII, *SPIE,* **4881**, 301–313.

Kirk, J.T.O., 1994: *Light and Photosynthesis in Aquatic Ecosystems,* 2nd edition, Cambridge University Press, 509 pp.

Kou, L., D. Labrie, and P. Chylek, 1993: Refractive indices of water and ice in the 0.65-2.5 μm spectral range. *Appl. Opt.,* **32,** 3,531–3,540.

Land, P.E., and J.D. Haigh, 1996: Atmospheric correction over case 2 waters with an iterative fitting algorithm, *Appl. Opt.,* **35,** 5,443–5,451.

Lee, Z.P., K.L. Carder, R.G. Steward, T.G. Peacock, C.O. Davis, and J.S. Patch, 1998: An empirical ocean color algorithm for light absorption coefficients of optically deep waters. *J. Geophys. Res.,* **103,** 27,967–27,978.

Loisel, H., and A. Morel, 1998: Light scattering and chlorophyll concentration in Case-1 water: a reexamination. *Limnol. Oceanogr.,* **43,** 847–858.

Maritorena, S., and J.E. O'Reilly, 2000: "OC2v2: Update on the initial operational SeaWiFS chlorophyll *a* algorithm." In: O'Reilly, J.E., and 24 Coauthors, SeaWiFS Postlaunch Calibration and Validation Analyses, Part 3. *NASA Tech. Memo. 2000–206892, Vol. 11,* S.B. Hooker and E.R. Firestone, Eds., NASA Goddard Space Flight Center, Greenbelt, Maryland, 3–8.

McClain, C.R., 2000: "SeaWiFS postlaunch calibration and validation overview." In: McClain, C.R., E.J. Ainsworth, R.A. Barnes, R.E. Eplee, Jr., F.S. Patt, W.D. Robinson, M. Wang, and S.W. Bailey, SeaWiFS Postlaunch Calibration and Validation Analyses, Part 1. *NASA Tech. Memo. 2000–206892, Vol. 9,* S.B. Hooker and E.R. Firestone, Eds., NASA Goddard Space Flight Center, Greenbelt, Maryland, 4–12.

——, E.J. Ainsworth, R.A. Barnes, R.E. Eplee, Jr., F.S. Patt, W.D. Robinson, M. Wang, and S.W. Bailey, 2000a: SeaWiFS Postlaunch Calibration and Validation Analyses, Part 1. *NASA Tech. Memo. 2000–206892, Vol. 9,* S.B. Hooker and E.R. Firestone, Eds., NASA Goddard Space Flight Center, Greenbelt, Maryland, 82 pp.

——, R.A. Barnes, R.E. Eplee, Jr., B.A. Franz, N.C. Hsu, F.S. Patt, C.M. Pietras, W.D. Robinson, B.D. Schieber, G.M. Schmidt, M. Wang, S.W. Bailey, and P.J. Werdell, 2000b: SeaWiFS Postlaunch Calibration and Validation Analyses, Part 2. *NASA Tech. Memo. 2000–206892, Vol. 10,* S.B. Hooker and E.R. Firestone, Eds., NASA Goddard Space Flight Center, Greenbelt, Maryland, 57 pp.

——, R. Evans, J. Brown, and M. Darzi, 1995: "SeaWiFS Quality Control Masks and Flags: Initial Algorithms and Implementation Strategy," In: McClain, C.R., W.E. Esaias, M. Darzi, F.S. Patt, R.H. Evans, J.W. Brown, K.R. Arrigo, C.W. Brown, R.A. Barnes, and L. Kumar: SeaWiFS Algorithms, Part 1. *NASA Tech. Memo. 104566, Vol. 28,* S.B. Hooker, E.R. Firestone, and J.G. Acker, Eds., NASA Goddard Space Flight Center, 3–7.

Moore, G.K., 1980: Satellite remote sensing of water turbidity. *Bull. Hydrolog. Sci.,* **25,** 407–421.

——, J. Aiken, and S.J. Lavender, 1999: The atmospheric correction of water colour and the quantitative retrieval of suspended particulate matter in Case II waters application to MERIS, *Int. J. Remote Sens.,* **20,** 1,713–1,734.

Morel, A., 1988: Optical modeling of the upper ocean in relation to its biogenous matter content (Case-1 waters). *J. Geophys. Res.,* **93,** 10,749–10,768.

——, and B. Gentili, 1991: Diffuse reflectance of oceanic waters: its dependence on sun angle as influenced by the molecular scattering contribution. *Appl. Opt.* **30,** 4,427–4,438.

——, and S. Maritorena, 2001: Bio-optical properties of oceanic waters: A reappraisal. *J. Geophys. Res.,* **106,** 7,163–7,180.

——, and J.L. Mueller, 2002: "Normalized water-leaving radiance and remote sensing reflectance: Bidirectional reflectance and other factors." In: J.L. Mueller and G.S. Fargion, Eds., Ocean Optics Protocols for Satellite Ocean Color Sensor Validation, Revision 3, Vol. 2. *NASA Tech. Memo. 2002–210004,* NASA Goddard Space Flight Center, Greenbelt, Maryland, 183–210.

Mueller, J.L., 1984: Effects of water reflectance at 670 nm on Coastal Zone Color Scanner (CZCS) aerosol radiance estimates off the coast of central California. *Ocean Optics VII, Proc. SPIE,* **489,** Bellingham, Washington, 179–186.

Neckel, H., and D. Labs, 1984: The solar radiation between 3,300 and 12,500Å. *Solar Physics,* **90,** 205–258.

O'Reilly, J., S. Maritorena, B. Mitchell, D. Siegel, K. Carder, S. Garver, M. Kahru, and C. McClain, 1998: Ocean color chlorophyll algorithms for SeaWiFS. *J. Geophys. Res.,* **103,** 24,937–24,953.

——, and C. Zetlin, 1998: Seasonal, Horizontal, and Vertical Distribution of Phytoplankton Chlorophyll *a* in the Northeast U.S. Continental Shelf Ecosystem. *NOAA Tech. Report NMFS,* **39,** Fishery Bulletin, 120 pp.

——, S. Maritorena, D.A. Siegel, M.C. O'Brien, D. Toole, B.G. Mitchell, M. Kahru, F.P. Chavez, P. Strutton, G.F. Cota, S.B. Hooker, C.R. McClain, K.L. Carder, F. Müller-Karger, L. Harding, A. Magnuson, D. Phinney, G.F. Moore, J. Aiken, K.R. Arrigo, R. Letelier, and M. Culver, 2000: "Ocean color chlorophyll *a* algorithms for SeaWiFS, OC2, and OC4: Version 4." In: J.E. O'Reilly and 24 Coauthors, SeaWiFS Postlaunch Calibration and Validation Analyses, Part 3. *NASA Tech. Memo. 2000–206892, Vol. 11,* S.B. Hooker and E.R. Firestone, Eds., NASA Goddard Space Flight Center, Greenbelt, Maryland, 9–23.

Palmer, K.F., and D. Williams, 1974: Optical properties of water in the near infrared. *J. Opt. Soc. Amer.,* **66,** 1,107–1,110.

Patt, F.S., 1999: "Assessment of geolocation for SeaWiFS and OCTS using island targets." *Proc. CNES Seminar, In-orbit characterization of optical imaging systems,* Bordeaux, France, November 1999.

——, 2002: Navigation Algorithms for the SeaWiFS Mission. *NASA Tech. Memo. 2002–206892, Vol. 16,* S.B. Hooker and E.R. Firestone, Eds., NASA Goddard Space Flight Center, Greenbelt, Maryland, 17 pp.

——, R.H. Woodward, and W.W. Gregg, 1997: An automated method for navigation assessment for Earth survey sensors using island targets. *Inter. J. Remote Sens.,* **18,** 3,311–3,336.

——, and S. Bilanow, 2001: "Horizon scanner triggering height analysis for OrbView-2." Proc. 2001 Flight Mechanics Symp., *NASA Contractor Rept. 2001–209986,* NASA Goddard Space Flight Center, Greenbelt, Maryland, 559–573.

Podesta, G., 1995: "SeaWiFS Global Fields: What's In a Day?" In: Mueller, J.L., R.S. Fraser, S.F. Biggar, K.J. Thome, P.N. Slater, A.W. Holmes, R.A. Barnes, C.T. Weir, D.A. Siegel, D.W. Menzies, A.F. Michaels, and G. Podesta: Case Studies for SeaWiFS Calibration and Validation, Part 3. *NASA Tech. Memo. 104566, Vol. 27,* S.B. Hooker and E.R. Firestone, Eds., NASA Goddard Space Flight Center, Greenbelt, Maryland, 34–42.

Pope, R.M., and E.S. Fry, 1997: Absorption spectrum (380–700 nm) of pure water. II. Integrating cavity measurements. *Appl. Opt.,* **36,** 8,710–8,723.

Press, W.H., and S.A. Teukolsky, 1992: Fitting straight line data with errors in both coordinates, *Computers in Physics,* **6,** 274–276.

Robinson, W.D., and M. Wang, 2000: "Vicarious calibration of SeaWiFS band 7." In: McClain, C.R., E.J. Ainsworth, R.A. Barnes, R.E. Eplee, Jr., F.S. Patt, W.D. Robinson, M. Wang, and S.W. Bailey, 2000: SeaWiFS Postlaunch Calibration and Validation Analyses, Part 1. *NASA Tech. Memo. 2000–206892, Vol. 9,* S.B. Hooker and E.R. Firestone, Eds., NASA Goddard Space Flight Center, Greenbelt, Maryland, 38–42.

Ruddick, K.G., F. Ovidio, and M. Rijkeboer, 2000: Atmospheric correction of SeaWiFS imagery for turbid coastal and inland waters. *Appl. Opt.,* **39,** 897–912.

Siegel, D.A., M. Wang, S. Maritorena, and W. Robinson, 2000: Atmospheric correction of satellite ocean color imagery: the black pixel assumption. *Appl. Opt.,* **39,** 3,582–3,591.

Sloss, P.W., 1988: Digital Relief of the Surface of the Earth. *Data Announcement 88-MGG-02,* NOAA, National Geophysical Data Center, Boulder, Colorado, 2 pp.

——, 2001: ETOPO2 Database on CD-ROM, NOAA, National Geophysical Data Center, Boulder, Colorado, USA.

Smith, R.C., and W.H. Wilson, 1981: Ship and satellite bio-optical research in the California Bight. *Oceanography from Space,* J.F.R. Gower, Ed., Plenum Press, 281–294.

——, and K.S. Baker, 1981: Optical properties of the clearest natural waters. *Appl. Opt.,* **20,** 177–184.

Siegel, D.A., M. Wang, S. Maritorena, and W. Robinson, 2000: Atmospheric correction of satellite ocean color imagery: the black pixel assumption. *Appl. Opt.,* **39,** 3,582–3,591.

Stumpf, R.P., and M.A. Tyler, 1988: Satellite detection of bloom and pigment distributions in estuaries. *Remote Sens. Environ.,* **24,** 385–404.

——, and J.R. Pennock, 1989: Calibration of a general optical equation for remote sensing of suspended sediment in a moderately turbid estuary. *J. Geophys. Res.,* **94,** 14,363–14,371.

Sydor, M., and R.A. Arnone, 1997: Effect of suspended particulate and dissolved organic matter on remote sensing of coastal and riverine waters. *Appl. Opt.,* **36,** 6,905–6,912.

Tanré, D., M. Herman, P.-Y. Deschamps, and A. De Leffe, 1979: Atmospheric modeling for space measurements of ground reflectances, including bidirectional properties. *Appl. Opt.,* **18,** 3,587–3,594.

Thuillier, G., M. Hersé, P.C. Simon, D. Labs, H. Mandel, D. Gillotay, and T. Foujols, 1998: The visible solar spectral irradiance from 350 to 850 nm as measured by the SOLSPEC spectrometer during the Atlas I mission. *Solar Physics,* **177,** 41–61.

——, ——, ——, ——, ——, ——, and ——, 2003: The solar spectral irradiance from 200 to 2400 nm as measured by the SOLSPEC spectrometer from the Atlas 1-2-3 and EURECA missions. *Solar Physics,* (submitted).

Wang, M., 2003: Correction of artifacts in the SeaWiFS atmospheric correction: Removing the discontinuity in the derived products. *Remote Sens. Environ.,* **84,** 603–611.

——, and S.W. Bailey, 2001: Correction of sun glint contamination on the SeaWiFS ocean and atmospheric products. *Appl. Opt.,* **40,** 4,790–4,798.

——, B.A. Franz, R.A. Barnes, and C.R. McClain, 2001: Effect of spectral bandpass on SeaWiFS-retrieved near-surface optical properties of the ocean. *Appl. Opt.,* **40,** 343–348.

Welschmeyer, N.A., 1994: Fluorometric analysis of chlorophyll *a* in the presence of chlorophyll *b* and phaeopigments. *Limnol. Oceanogr.,* **39,** 1,985–1,992.

Yeh, E-n, M. Darzi, and L. Kumar, 1997: "SeaWiFS Stray Light Correction Algorithm," In: Yeh, E-n, R.A. Barnes, M. Darzi, L. Kumar, E.A. Early, B.C. Johnson, and J.L. Mueller: Case Studies for SeaWiFS Calibration and Validation, Part 4. *NASA Tech. Memo. 104566, Vol. 41,* S.B. Hooker and E.R. Firestone Eds., NASA Goddard Space Flight Center, Greenbelt, Maryland, 24–30.

Young, D.F., P. Minnis, D.R. Doelling, G.G. Gibson, and T. Wong, 1998: Temporal interpolation methods for the clouds and Earth's Radiant Energy System (CERES) experiment. *J. Appl. Meteor.,* **37,** 572–590.

Zege, E.P., A.P. Ivanov, and I.L. Katsev, 1991: *Image Transfer Through a Scattering Medium.* Springer-Verlag, New York, 349 pp.

The SeaWiFS Postlaunch Technical Report Series

Vol. 1

Johnson, B.C., J.B. Fowler, and C.L. Cromer, 1998: The SeaWiFS Transfer Radiometer (SXR). *NASA Tech. Memo. 1998–206892, Vol. 1,* S.B. Hooker and E.R. Firestone, Eds., NASA Goddard Space Flight Center, Greenbelt, Maryland, 58 pp.

Vol. 2

Aiken, J., D.G. Cummings, S.W. Gibb, N.W. Rees, R. Woodd-Walker, E.M.S. Woodward, J. Woolfenden, S.B. Hooker, J-F. Berthon, C.D. Dempsey, D.J. Suggett, P. Wood, C. Donlon, N. González-Benítez, I. Huskin, M. Quevedo, R. Barciela-Fernandez, C. de Vargas, and C. McKee, 1998: AMT-5 Cruise Report. *NASA Tech. Memo. 1998–206892, Vol. 2,* S.B. Hooker and E.R. Firestone, Eds., NASA Goddard Space Flight Center, Greenbelt, Maryland, 113 pp.

Vol. 3

Hooker, S.B., G. Zibordi, G. Lazin, and S. McLean, 1999: The SeaBOARR-98 Field Campaign. *NASA Tech. Memo. 1999–206892, Vol. 3,* S.B. Hooker and E.R. Firestone, Eds., NASA Goddard Space Flight Center, Greenbelt, Maryland, 40 pp.

Vol. 4

Johnson, B.C., E.A. Early, R.E. Eplee, Jr., R.A. Barnes, and R.T. Caffrey, 1999: The 1997 Prelaunch Radiometric Calibration of SeaWiFS. *NASA Tech. Memo. 1999–206892, Vol. 4,* S.B. Hooker and E.R. Firestone, Eds., NASA Goddard Space Flight Center, Greenbelt, Maryland, 51 pp.

Vol. 5

Barnes, R.A., R.E. Eplee, Jr., S.F. Biggar, K.J. Thome, E.F. Zalewski, P.N. Slater, and A.W. Holmes 1999: The SeaWiFS Solar Radiation-Based Calibration and the Transfer-to-Orbit Experiment. *NASA Tech. Memo. 1999–206892, Vol. 5,* S.B. Hooker and E.R. Firestone, Eds., NASA Goddard Space Flight Center, 28 pp.

Vol. 6

Firestone, E.R., and S.B. Hooker, 2000: SeaWiFS Postlaunch Technical Report Series Cumulative Index: Volumes 1–5. *NASA Tech. Memo. 2000–206892, Vol. 6,* S.B. Hooker and E.R. Firestone, Eds., NASA Goddard Space Flight Center, Greenbelt, Maryland, 14 pp.

Vol. 7

Johnson, B.C., H.W. Yoon, S.S. Bruce, P-S. Shaw, A. Thompson, S.B. Hooker, R.E. Eplee, Jr., R.A. Barnes, S. Maritorena, and J.L. Mueller, 1999: The Fifth SeaWiFS Intercalibration Round-Robin Experiment (SIRREX-5), July 1996. *NASA Tech. Memo. 1999–206892, Vol. 7,* S.B. Hooker and E.R. Firestone, Eds., NASA Goddard Space Flight Center, 75 pp.

Vol. 8

Hooker, S.B., and G. Lazin, 2000: The SeaBOARR-99 Field Campaign. *NASA Tech. Memo. 2000–206892, Vol. 8,* S.B. Hooker and E.R. Firestone, Eds., NASA Goddard Space Flight Center, 46 pp.

Vol. 9

McClain, C.R., E.J. Ainsworth, R.A. Barnes, R.E. Eplee, Jr., F.S. Patt, W.D. Robinson, M. Wang, and S.W. Bailey, 2000: SeaWiFS Postlaunch Calibration and Validation Analyses, Part 1. *NASA Tech. Memo. 2000–206892, Vol. 9,* S.B. Hooker and E.R. Firestone, Eds., NASA Goddard Space Flight Center, 82 pp.

Vol. 10

McClain, C.R., R.A. Barnes, R.E. Eplee, Jr., B.A. Franz, N.C. Hsu, F.S. Patt, C.M. Pietras, W.D. Robinson, B.D. Schieber, G.M. Schmidt, M. Wang, S.W. Bailey, and P.J. Werdell, 2000: SeaWiFS Postlaunch Calibration and Validation Analyses, Part 2. *NASA Tech. Memo. 2000–206892, Vol. 10,* S.B. Hooker and E.R. Firestone, Eds., NASA Goddard Space Flight Center, 57 pp.

Vol. 11

O'Reilly, J.E., S. Maritorena, M.C. O'Brien, D.A. Siegel, D. Toole, D. Menzies, R.C. Smith, J.L. Mueller, B.G. Mitchell, M. Kahru, F.P. Chavez, P. Strutton, G.F. Cota, S.B. Hooker, C.R. McClain, K.L. Carder, F. Müller-Karger, L. Harding, A. Magnuson, D. Phinney, G.F. Moore, J. Aiken, K.R. Arrigo, R. Letelier, and M. Culver 2000: SeaWiFS Postlaunch Calibration and Validation Analyses, Part 3. *NASA Tech. Memo. 2000–206892, Vol. 11,* S.B. Hooker and E.R. Firestone, Eds., NASA Goddard Space Flight Center, 49 pp.

Vol. 12

Firestone, E.R., and S.B. Hooker, 2000: SeaWiFS Postlaunch Technical Report Series Cumulative Index: Volumes 1–11. *NASA Tech. Memo. 2000–206892, Vol. 12,* S.B. Hooker and E.R. Firestone, Eds., NASA Goddard Space Flight Center, Greenbelt, Maryland, 24 pp.

Vol. 13

Hooker, S.B., G. Zibordi, J-F. Berthon, S.W. Bailey, and C.M. Pietras, 2000: The SeaWiFS Photometer Revision for Incident Surface Measurement (SeaPRISM) Field Commissioning. *NASA Tech. Memo. 2000–206892, Vol. 13,* S.B. Hooker and E.R. Firestone, Eds., NASA Goddard Space Flight Center, Greenbelt, Maryland, 24 pp.

Vol. 14

Hooker, S.B., H. Claustre, J. Ras, L. Van Heukelem, J-F. Berthon, C. Targa, D. van der Linde, R. Barlow, and H. Sessions, 2000: The First SeaWiFS HPLC Analysis Round-Robin Experiment (SeaHARRE-1). *NASA Tech. Memo. 2000–206892, Vol. 14,* S.B. Hooker and E.R. Firestone, Eds., NASA Goddard Space Flight Center, Greenbelt, Maryland, 42 pp.

Vol. 15

Hooker, S.B., G. Zibordi, J-F. Berthon, D. D'Alimonte, S. Maritorena, S. McLean, and J. Sildam, 2001: Results of the Second SeaWiFS Data Analysis Round Robin, March 2000 (DARR-00). *NASA Tech. Memo. 2001–206892, Vol. 15,* S.B. Hooker and E.R. Firestone, Eds., NASA Goddard Space Flight Center, Greenbelt, Maryland, 71 pp.

Vol. 16

Patt, F.S., 2002: Navigation Algorithms for the SeaWiFS Mission. *NASA Tech. Memo. 2002–206892, Vol. 16,* S.B. er and E.R. Firestone, Eds., NASA Goddard Space Flight Center, Greenbelt, Maryland, 17 pp.

Vol. 17

Hooker, S.B., S. McLean, J. Sherman, M. Small, G. Lazin, G. Zibordi, and J.W. Brown, 2002: The Seventh SeaWiFS Intercalibration Round-Robin Experiment (SIRREX-7), March 1999. *NASA Tech. Memo. 2002–206892, Vol. 17,* S.B. Hooker and E.R. Firestone, Eds., NASA Goddard Space Flight Center, Greenbelt, Maryland, 69 pp.

Vol. 18

Firestone, E.R., and S.B. Hooker, 2003: SeaWiFS Postlaunch Technical Report Series Cumulative Index: Volumes 1–17. *NASA Tech. Memo. 2003–206892, Vol. 18,* S.B. Hooker and E.R. Firestone, Eds., NASA Goddard Space Flight Center, Greenbelt, Maryland, 28 pp.

Vol. 19

Zibordi, G., J-F. Berthon, J.P. Doyle, S. Grossi, D. van der Linde, C. Targa, and L. Alberotanza 2002: Coastal Atmosphere and Sea Time Series (CoASTS), Part 1: A Tower-Based Long-Term Measurement Program. *NASA Tech. Memo. 2002–206892, Vol. 19,* S.B. Hooker and E.R. Firestone, Eds., NASA Goddard Space Flight Center, Greenbelt, Maryland, 29 pp.

Vol. 20

Berthon, J-F., G. Zibordi, J.P. Doyle, S. Grossi, D. van der Linde, and C. Targa, 2002: Coastal Atmosphere and Sea Time Series (CoASTS), Part 2: Data Analysis. *NASA Tech. Memo. 2002–206892, Vol. 20,* S.B. Hooker and E.R. Firestone, Eds., NASA Goddard Space Flight Center, Greenbelt, Maryland, 25 pp.

Vol. 21

Zibordi, G., D. D'Alimonte, D. van der Linde, J-F. Berthon, S.B. Hooker, J.L. Mueller, G. Lazin, and S. McLean, 2002: The Eighth SeaWiFS Intercalibration Round-Robin Experiment (SIRREX-8), September–December 2001. *NASA Tech. Memo. 2002–206892, Vol. 21,* S.B. Hooker and E.R. Firestone, Eds., NASA Goddard Space Flight Center, Greenbelt, Maryland, 39 pp.

Vol. 22

Patt, F.S., R.A. Barnes, R.E. Eplee, Jr., B.A. Franz, W.D. Robinson, G.C. Feldman, S.W. Bailey, J. Gales, P.J. Werdell, M. Wang, R. Frouin, R.P. Stumpf, R.A. Arnone, R.W. Gould, Jr., P.M. Martinolich, V. Ransibrahmanakul, J.E. O'Reilly, and J.A. Yoder, 2003: Algorithm Updates for the Fourth SeaWiFS Data Reprocessing, *NASA Tech. Memo. 2003–206892, Vol. 22,* S.B. Hooker and E.R. Firestone, Eds., NASA Goddard Space Flight Center, Greenbelt, Maryland, 74 pp.